APPLICATION OF AN ELASTO-PLASTIC CONTINUUM MODEL TO PROBLEMS IN GEOPHYSICS

A thesis submitted to the University of Manchester
for the degree of Doctor of Philosophy
in the Faculty of Engineering and Physical Sciences

2014

By
Matthew Crooks
School of Mathematics

Contents

Word Count: 20,109

List of Tables

List of Figures

The University of Manchester

Matthew Crooks
Doctor of Philosophy
Application of an elasto-plastic continuum model to problems in geophysics
21st July 2014

A model for stress and strain accumulation in strike slip earthquake faults is presented in which a finite width cuboidal fault region is embedded between two cuboidal tectonic plates. Elasto-plastic continuum constitutive equations model the gouge in the fault and the tectonic plates are linear elastic solids obeying the generalised Hooke's law.

The model predicts a velocity field which is comparable to surface deformations. The plastic behaviour of the fault material allows the velocities in the tectonic plate to increase to values which are independent of the distance from the fault.

Both of the non-trivial stress and strain components accumulate most significantly in the vicinity of the fault. The release of these strains during a dynamic earthquake event would produce the most severe deformations at the fault which is consistent with observations and the notion of an epicenter. The accumulations in the model, however, are at depths larger than would be expected. Plastic strains build up most significantly at the base of the fault which is in yield for the longest length of time but additionally is subject to larger temperatures which makes the material more ductile.

The speed of propagation of the elasto-plastic boundary is calculated and its acceleration towards the surface of the fault may be indicative of a dynamic earthquake type event.

Declaration

No portion of the work referred to in this thesis has been submitted in support of an application for another degree or qualification of this or any other university or other institute of learning.

Copyright

i. The author of this thesis (including any appendices and/or schedules to this thesis) owns certain copyright or related rights in it (the "Copyright") and s/he has given The University of Manchester certain rights to use such Copyright, including for administrative purposes.

ii. Copies of this thesis, either in full or in extracts and whether in hard or electronic copy, may be made **only** in accordance with the Copyright, Designs and Patents Act 1988 (as amended) and regulations issued under it or, where appropriate, in accordance with licensing agreements which the University has from time to time. This page must form part of any such copies made.

iii. The ownership of certain Copyright, patents, designs, trade marks and other intellectual property (the "Intellectual Property") and any reproductions of copyright works in the thesis, for example graphs and tables ("Reproductions"), which may be described in this thesis, may not be owned by the author and may be owned by third parties. Such Intellectual Property and Reproductions cannot and must not be made available for use without the prior written permission of the owner(s) of the relevant Intellectual Property and/or Reproductions.

iv. Further information on the conditions under which disclosure, publication and commercialisation of this thesis, the Copyright and any Intellectual Property and/or Reproductions described in it may take place is available in the University IP Policy (see `http://documents.manchester.ac.uk/DocuInfo.aspx?DocID=487`), in any relevant Thesis restriction declarations deposited in the University Library, The University Library's regulations (see `http://www.manchester.ac.uk/library/aboutus/regulations`) and

in The University's policy on presentation of Theses

Acknowledgements

I would like to thank my supervisor Dr David Harris for his invaluable input into this thesis and the support over the years for which I am incredibly grateful.

I would like to thank the waves group at the University of Manchester for welcoming me into their group and the support and friendship they offered. In particular I thank Professor David Abrahams and Dr William Parnell as well as Dr Phil Cotterill, Tom, Ruth, Vic, Maria, Duncan and of course Riccardo.

My immense gratitude goes to my girlfriend Vic for making me laugh so much over the last 4 years and keeping me sane while I wrestled with Matlab. I thank her for unwavering interest and patience and for allowing me to be a kept man while I finish writing up. I hope to be able to reciprocate the support over the next few months.

I finally thank my family and friends; Patrick for always being in the office, most afternoons, to recant stories from the showbiz world, as well as Phil, Andrew, Hannah, James and Ben for their friendship over the last 4 years.

Dedicated to my Grandma,
Ann Crooks
24th April 1925 - 1st June 2014

Chapter 1

Introduction

In this thesis we are interested in the strain which accumulates in the tectonic plates and fault material between earthquake events. We develop a two-dimensional anti-plane deformation model which incorporates the theories that are standard in both geophysics and continuum plasticity and modifies the work by Rowshandel and Nemat-Nasser [1986] to include a finite width fault.

The Earth's interior is divided into several layers each distinguished by its heterogeneous chemical composition and rheology. The crust is the solid outermost strata of the Earth and varies between $0 - 35km$ thick. Below the crust lies the mantle which extends about $2900km$ towards the Earth's centre. The lithosphere consists of the crust and the outermost layer of the mantle and it is within this $50 - 100km$ thick region that the tectonic plates lie. Up to a further $75 - 225km$ depth below the lithosphere lies the asthenosphere, a region with a considerably lower viscosity.

The pressure within the Earth increases with increasing depth and this has the effect of increasing the melting point of the rock; defined as the minimum temperature at which all of the rock's constituent compounds are at or above their individual melting points. Additionally, the temperature increases towards the Earth's core. The rheology of the rock in this region is, therefore, determined by a balance between temperature and melting point.

The temperature gradient near the Earth's surface is about $20 - 30 K km^{-1}$ but this decreases rapidly through a region about $75 - 225km$ deep to a more modest

positive value. This temperature profile is demonstrated by the black line in Figure 1.1. The pressure increases linearly with depth and it is assumed that this leads to a linear increase in melting temperature; neglecting any change in the constituents of the rock and a change in gravity with depth. This is demonstrated in Figure 1.1 by the red line. Due to the heterogenous nature of rock, some compounds within it may be molten at temperatures below the bulk melting temperature. Within the region $75 - 225km$ deep the ratio of temperature to melting point reaches a minimum value and it is within this region that the maximum fraction of the rock's minerals are molten. The effect is a significant reduction in the viscosity of the rock within this region, demonstrated by Figure 1.2. This region is called the asthenosphere and due to its rheology undergoes convection in the form of viscous creep. It is the convective currents that Elsasser [1969] hypothesised is the driving mechanism for tectonic plate movement.

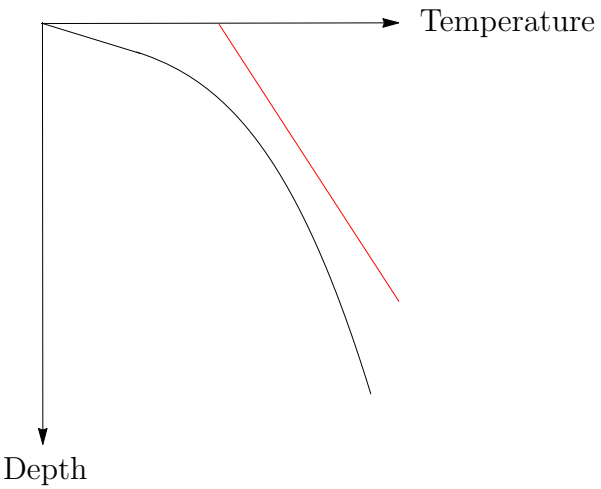

Figure 1.1: The temperature profile of the Earth's interior with depth is shown in black and the change in melting temperature with depth is shown in red.

Some of the earliest studies of stress and strain accumulation models of earthquake faulting were based on dislocations within linearly elastic bodies (Housner [1953] and Savage and Prescott [1978]). The early models of a finite-depth, two-dimensional crack within an elastic half-plane have been extended to include a distribution of dislocations, Savage [2006], but has failed to be widely adopted. Although these show some agreement with surface displacements (Lisowski et al.

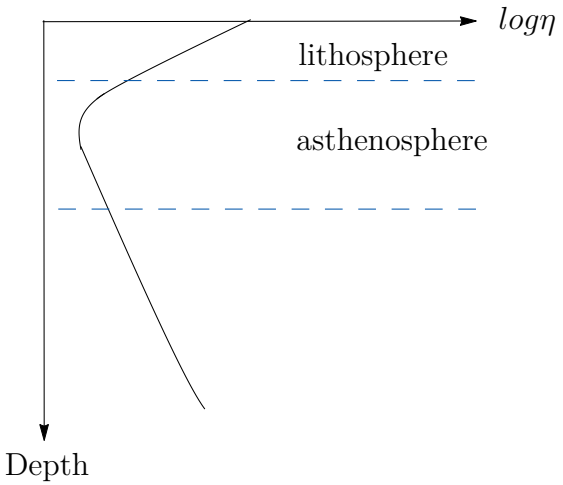

Figure 1.2: The depth variation of the *log* of the viscosity, η, in the Earth's interior with depth with approximate positions of the regions called the lithosphere and asthenosphere.

[1991]) they do not take into account the mechanical properties of the fault gauge. Furthermore, they do not lend themselves to the recurring pattern of earthquake cycles (Prescott and Nur [1981], Turcotte and Spence [1974]) nor do they encompass any driving mechanism for the plate tectonics.

The first mathematical modelling of a visco-elastic asthenosphere was by Nur and Mavko [1974] however they did not attribute the driving mechanism of earthquake faulting to advection within the asthenosphere and kept the dislocation idea of previous models. Coupling the Earth's elastic lithosphere to a visco-elastic layer complicated the mathematics significantly and much work was carried out to assess whether such difficulties were necessary. Savage and Prescott [1978] and Thatcher [1983] have compared elastic half-plane models with the asthenosphere model of Nur and Mavko. Reid's elastic rebound hypothesis (Reid [1910]) states that without asthenosphere coupling there should be no residual strains following an earthquake. However, Savage and Prescott [1978], Thatcher [1983], found that if the relaxation time of the asthenosphere is longer than the recurrence time of an earthquake then there will be long-term strain accumulation over a series of earthquakes. This strain accumulation becomes less significant when the depth of the dislocation is small in comparison to the thickness of the lithosphere.

Turcotte and Spence [1974] have suggested a model in which the viscous traction forces from the asthenosphere may be negligible in comparison to the forces present at the fault. Applying a free surface condition to the lower surface allows them to find an analytic solution based on Koiter [1959] for a fault which comprises a crack starting from a finite depth and extending down to the lower surface of the lithosphere. However once the crack has propagated through to the surface of the lithosphere, as they suggest happens during an earthquake, then the model cannot be applied again and so it does not admit a pattern of recurring earthquakes.

A further model (Lehner et al. [1981], Li and Rice [1987]) suggests that an earthquake may be a propagating fracture within the lithosphere of the Nur and Mavko model. Some progress is made analytically by depth averaging through the lithosphere. Such an approach loses the concept of a hypocentre.

Much work has been published on the frictional sliding of rocks (Rice and Simons [1976], Rice and Tse [1986], Scholtz [1990], Scholtz [1998]) and the proposal that an earthquake occurs when the static friction force is overcome and dynamic friction begins. There is evidence on the surface of the earth that a fault is not simply the meeting of two intact rock masses but in fact over millions of years fragments of rock have broken away to form a region of a granular material called gouge (Rice [2007], Scholtz [1990]). Such a material must be modelled with some form of granular constitutive equation.

The most realistic model of earthquake faulting found in the literature is given by Rowshandel and Nemat-Nasser [1986]. This encompasses the convection in the visco-elastic asthenosphere driving the earthquake, a plasticity constitutive law (Nemat-Nasser and Shokooh [1980], Nemat-Nasser and Shokooh [1980]) down the fault and a locked top section of the fault whose eventual release represents the earthquake. Some seemingly unpublished asymptotics that assume a linear velocity profile across the fault reduced the width of the fault to zero and led Nemat-Nasser and Rowshandel to declare the fault to be simply a two-dimensional plane where the two tectonic plates meet. This inevitably simplifies the problem but is somewhat unrealistic. Their paper as a whole though does offer a good model for the coupling of a plastic constitutive equation to the lithosphere and this thesis is focused on solving a similar problem but with a fault of finite width filled with a granular material.

A granular material is a collection of individual solid particles called grains. They can exhibit similar properties to both liquids and solids; they can flow and conform to the shape of the container they are placed in but they can also support shear stresses when stationary. The space between the grains can be filled with a liquid or a gas. The presence of an inviscid gas may be neglected but a liquid filled void can interact with the grains and must be accounted for.

Fault material is a granular material that has been created by the grinding of fragments of rock which break off the faces of the tectonic plates at the fault during earthquakes. The rock type is classified depending on its grain size. Larger fragments of rock are referred to as clasts and are typically the size of gravel. Conglomerates are composed prodominantly of clasts embedded within finer grains. The larger particles in conglomerates are smooth and materials with angular clasts are referred to as brecca. As the grains are ground down further they form fault gouge; a granular material with very small grain size.

Due to the intricacies of such materials their behaviour is highly dependent on the situtation and this, coupled with their intractable response during experiments, has led to a lack of consensus on a constitutive model. It is arguable that one equation could not accurately capture the vast array of behaviours of granular materials from loose gaseous type flow though to compacted solid states. Instead of deriving one unified theory, models are often derived for specific problems such as avalanches (Gray et al. [1999]) and sand dunes (Kennedy [1963]) with measureable success.

The discrete nature of granular materials means that they do not satisfy the continuum hypothesis as a vanishingly small volume element may have very different properties either side of a grain boundary. One commonly applied approach is the discrete element method which models each individual grain using classic Newtonian mechanics to model the collisions. This can be successful, especially for loose orderings and packing problems, but it is limited to relatively small numbers of grains by the computer power currently available. Futhermore, due to the need for information on collisions its application currently only extends to a mix of, at most, a few convex shaped grains.

A continuum approach is more amenable to large scale geophysical problems. In such problems there is often a sufficiently large number of grains that the

microscopic length scales are much smaller than the macroscopic ones. Continuum models homogenize out the individual grains and properties of the material at a given point by taking the average value over a representative volume element. The granular nature of the material is then captured through various means such as the dilatation and angle of internal friction.

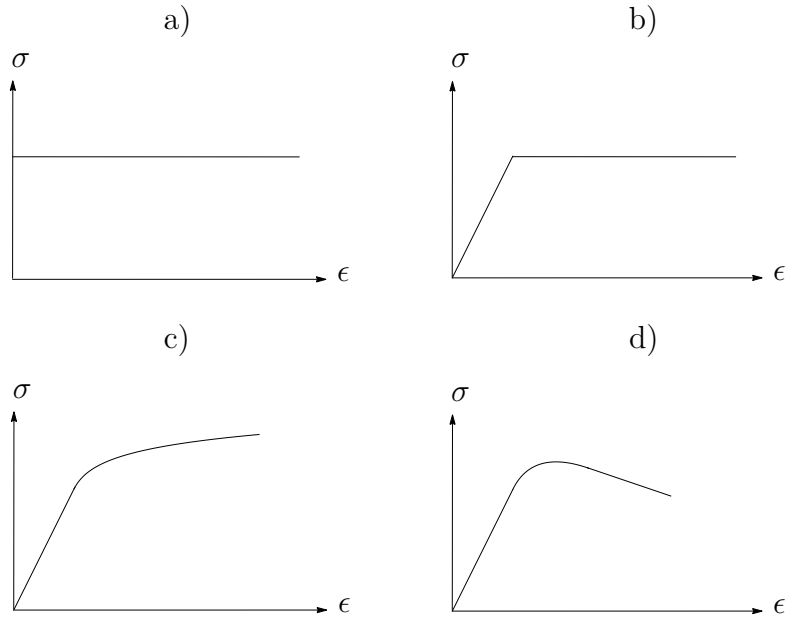

Figure 1.3: Stress-strain curves for a variety of plasticity models where ϵ is the strain and σ is the stress; a) rigid plastic, b) elastic-perfectly plastic, c) work hardening elasto-plasticity d) work softening elasto-plasticity.

Modelling of granular materials using continuum plasticity models is the focus of this thesis. The term *Plasticity* describes the permanent deformations that a material undergoes when subjected to an applied force. Initiation of the plastic deformation occurs when the material reaches *yield*. Representative stress-strain curves for a range of plasticity models are shown in Figure 1.3. A material with a stress-strain curve similar to Figure 1.3a is referred to as *rigid perfectly plastic*. These behave as a rigid body unless the applied stress is equal to the yield stress, σ_c, at which point the material begins to flow. The stress cannot exceed the yield stress. Figure 1.3b shows the response of an *elastic-perfectly plastic* material. The initial straight sloped section represents the linear elastic regime of the deformation. Within this phase the applied stress can be removed and the

material will return to its original configuration. If the load is increased up to the value σ_c the material begins to flow and undergoes permanent deformation. A material that undergoes *work/strain-hardening* will have a stress-strain curve similar to that given in Figure 1.3c. The characteristic of this material is the gradual change in gradient; as the material deforms, an increasingly larger strain increment results from the same additional stress increment. During work/strain hardening the grains in the material reorder themselves to interlock more substantially. Further discussion of work/strain hardening is given in Section 2.5.2. The final stress-strain curve represents *work/strain softening* and is described as a reduction in the resistance of a material to shear stresses as shear strain increases. This phenomenon is shown on Figure 1.3d by the negative gradient.

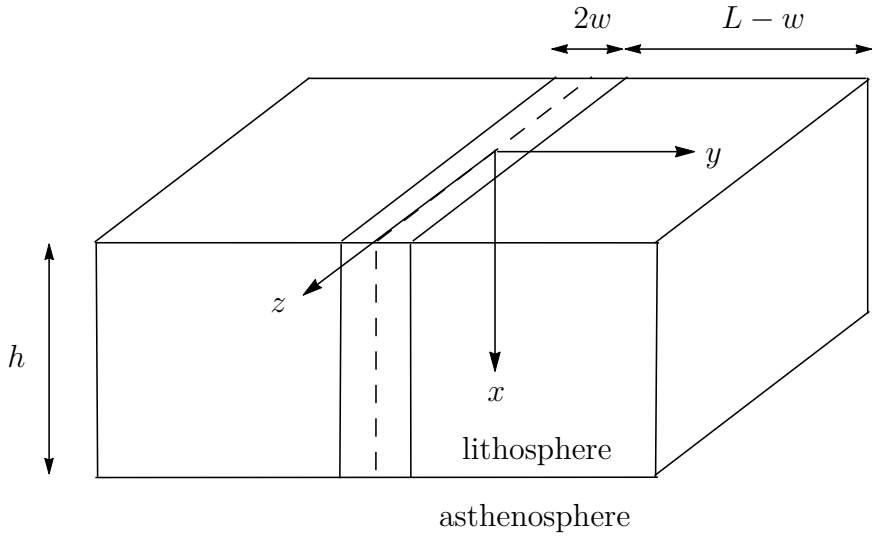

Figure 1.4: The 3D geometry of the problem. A cuboid fault region of width $2w$ is embedded between two other cuboidal regions representing the tectonic plates. The depth in the x direction of the tectonic plate and fault material is h and the two tectonic plates extended a distance L from the centre of the fault in the y direction.

The three dimensional geometry of the problem is shown in Figure 1.4. We introduce a Cartesian coordinate system with x vertically downwards, y horizontal and normal to the fault and z directed along the length of the fault. The tectonic plates and fault extend to the base of the lithosphere which is at a depth $h \sim 50km$ below the Earth's surface. The fault is assumed to be of infinite length in the z

direction and of width $2w \sim 1 - 10m$ in the y direction. The tectonic plates meet the fault along vertical planes defined by $y = \pm w$ and are modelled up to a distance $L \sim 25km$ from the fault at which a far field boundary condition is applied. At the base of the lithosphere there is a forcing due to convection within the asthenosphere. This is modelled as an applied traction-rate. A representative cross section through the plane $z = const$ is shown in Figure 1.5. The portion of the plane contained within the fault is the rectangular region shown in red. An elasto-plastic material will, in general, have two sub-regions within it as shown in Figure 1.5. Region $ABCD$ consists of the pre-yield elastically behaving material and the region $CDEF$ contains the material which has reached yield and therefore has a plastic constituent to its deformation. The boundary between the two regions, CD, is termed the *elasto-plastic boundary*. Therefore, once part of the fault material reaches yield it is necessary to solve the problem with two discrete regions within the fault.

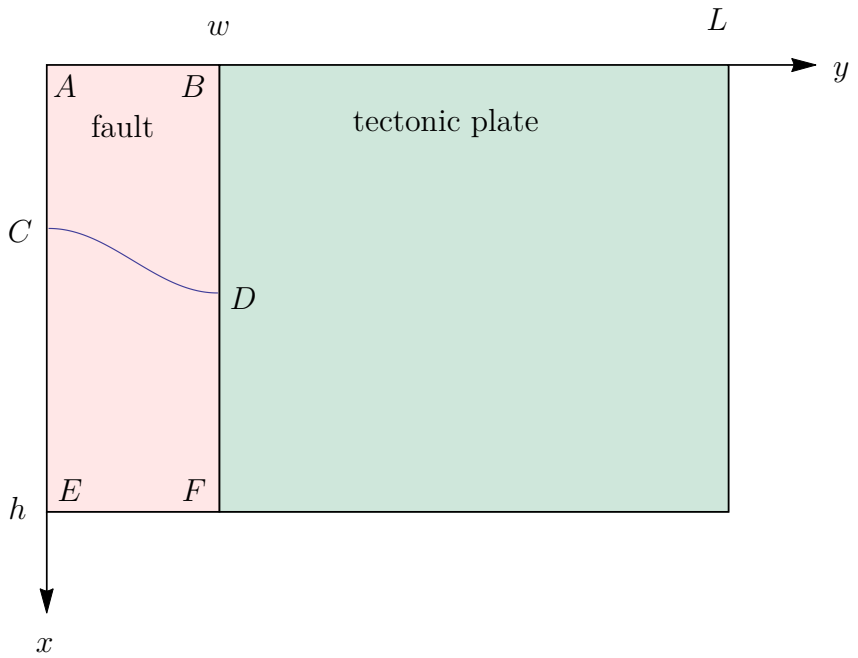

Figure 1.5: The 2D geometry of the problem. The green region represents the cross section of the tectonic plate and the red region is the fault. The elasto-plastic boundary that separates the fault material that is in yield from that which has not reached yield is shown by the blue curve across the fault.

An overview of the thesis layout is as follows. Chapters 2-4 introduce the background required for the later work beginning with continuum mechanics and granular materials in Chapter 2. Chapters 3 and 4 present some of the relevant theory on finite differences and classifying PDEs.

The original material begins in Chapter 5 with an explanation of the model used to represent earthquake faulting. This is an extension of the model used by Rowshandel and Nemat-Nasser [1986]. Values from the literature are assigned to the various material parameters within this chapter.

Chapter 6 presents an analytic solution to the velocity field in the early stages of the deformation. This is important as it is used to verify the convergence of the numerical scheme given in Chapters 7 and 8.

Chapter 7 applies standard finite difference methods to the particular problem outlined in Chapter 5. It focuses on the grid points in the domain which have a regular mesh avoiding the curved elasto-plastic boundary and the two corners at which singularities in the stress-rate occur.

A novel method of applying the finite difference method to curved boundaries is presented in Chapter 8. The method uses quadratic interpolation to approximate points outside the domain which appear in standard finite difference expressions. This is applied to grid points in the vicinity of the elasto-plastic boundary and convergence plots are given comparing the numerical scheme to the analytic solution from Chapter 6.

Chapter 9 derives asymptotic approximations to the stress-rate singularities near the corners positioned at (h, w) and where the elasto plastic boundary meets the boundary between the fault and the tectonic plate. A novel method of implementing such a solution into a numerical scheme is described.

An explanation of the Matlab code used to implement the numerical scheme is given in Chapter 8 with some additional information on some of the difficulties encountered such as the accumulation of the stress. The long narrow geometry of the fault produces several boundary layers which are resolved through addaptive mesh refinements, this is explained in Section 10.3.

Chapter 11 presents and discusses the results from the numerical model. The velocity field within the tectonic plate is shown at various timesteps throughout the earthquake cycle as well the accumulated stress and strain.

Chapter 2

Background: Theory of Continuum Mechanics

In this chapter we give an overview of continuum mechanics. We begin by introducing the concepts of stress and strain before discussing the constitutive behaviour of linear elastic and granular materials which are used later in the thesis to model the deformation of the tectonic plates and fault material.

2.1 Forces

The forces acting on a body can be divided into two quantities; *body forces* and *surface forces*. Body forces act on the internal volume of the body whereas surface forces act on the external and internal surfaces of a body. An introduction to each of these concepts is presented here with the aim of establishing notation. There is a plethora of books which provide more in-depth discussions, see for example Spencer [1968], Muskhelishvili [1953] and Graff [1991].

2.1.1 Body Forces

Body forces act on the volume or mass of a body. Denote by V the volume bounded by a surface and consider a small volume element δV. Suppose the body is subjected to a body force per unit mass, $\mathbf{b}$. The force per unit volume is then $\mathbf{F_b} = \rho\mathbf{b}$ and the force exerted on δV is $\rho\mathbf{b}\delta V$. Note that $\rho\delta V$ is the mass, δm, of

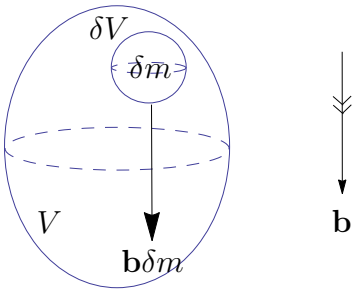

Figure 2.1: A body with volume V under the action of a body force $\mathbf{b}$. The infinitesimal volume element δV of mass δm feels a force of $\mathbf{b}\delta m$.

the volume δV and so the force exerted on δV can be expressed as $\mathbf{b}\delta m$ as shown in Figure 2.1. The total body force acting on a body can therefore be written as the integral of the body forces over the body's volume

$$\mathcal{F}_b = \int_V \rho \mathbf{b} dV. \tag{2.1}$$

2.1.2 Stress

Denote the surface of a body by S and consider a point P on S as shown in Figure 2.2. The outwards unit normal to S at P relative to a Cartesian coordinate system (x, y, z) is denoted $\mathbf{n}$ and points outwards from the body.

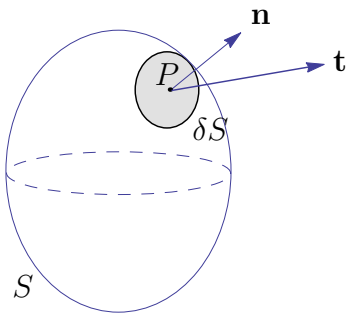

Figure 2.2: A body with surface S. The small area of the surface δS surrounds the point P and the normal to S at P is $\mathbf{n}$. The traction acting on S at P is denoted $\mathbf{t}$.

Suppose a force $\delta\mathbf{F}$ is applied to a small region δS of S. The traction $\mathbf{t}$ at P is

the force per unit area and can be expressed by the limit

$$\mathbf{t}(x, y, z) = \lim_{\delta S \to 0} \frac{\delta \mathbf{F}}{\delta S}, \tag{2.2}$$

as δS reduces to the point P. The total surface force exerted on the body can be obtained by integrating the traction over S, namely

$$\mathbf{F} = \int_S \mathbf{t} dS. \tag{2.3}$$

The region enclosed by S can be divided into two regions by defining an internal surface $\hat{S}$, as shown in Figure 2.3. The two constituent parts exert a force on one another across the surface $\hat{S}$, which is denoted $\pm\hat{F}$. The traction on this internal surface having unit normal $\hat{\mathbf{n}}$ is then given in an analogous way to that on an external surface, (2.2), thus

$$\mathbf{t}(x, y, z) = \lim_{\delta \hat{S} \to 0} \frac{\delta \hat{\mathbf{F}}}{\delta \hat{S}}.$$

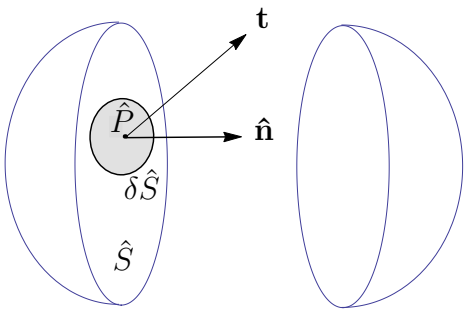

Figure 2.3: A body with internal surface $\hat{S}$. The small area of the surface $\delta\hat{S}$ surrounds the point $\hat{P}$ and the normal to $\hat{S}$ at $\hat{P}$ is $\hat{\mathbf{n}}$. The traction acting on $\hat{S}$ at $\hat{P}$ is denoted $\mathbf{t}$.

2.1.3 The Stress Tensor

There are infinitely many potential orientations of $\hat{S}$ and so it is impossible to represent the forces within a body by the traction alone. Thus, we introduce the

concept of the (Cauchy) *stress tensor*, denoted σ, given by

$$\sigma = \begin{pmatrix} \sigma_{11} & \sigma_{12} & \sigma_{13} \\ \sigma_{21} & \sigma_{22} & \sigma_{23} \\ \sigma_{31} & \sigma_{32} & \sigma_{33} \end{pmatrix},$$

relative to a cartesian coordinate system $Oxyz$. To allow for the use of the summation convention we use numerical subscripts to correspond to the coordinate directions and identify $x = x_1$, $y = x_2$ and $z = x_3$. Each stress component σ_{ij} is, in general, a function of x, y, z and t and is the i^{th} component of the traction on a surface with unit normal in the j^{th} coordinate direction. The diagonal components of the stress tensor are called *normal stresses* and the off-diagonal elements are the *shear stresses*. By considering the stresses on an infinitesimal tetrahedron it can be shown, see for example Gould [1994], that the traction on a surface with unit normal $\mathbf{n}$ can be expressed as the matrix product of the stress tensor with $\mathbf{n}$, thus

$$\mathbf{t} = \sigma \cdot \mathbf{n}, \tag{2.4}$$

where $\mathbf{n}$ is a column vector. Furthermore, the stress tensor can be shown to be symmetric by considering a moment balance on an infinitesimal cubic volume and so can be written

$$\sigma = \begin{pmatrix} \sigma_{11} & \sigma_{12} & \sigma_{13} \\ \sigma_{12} & \sigma_{22} & \sigma_{23} \\ \sigma_{13} & \sigma_{23} & \sigma_{33} \end{pmatrix}.$$

The eigenvalues of the stress tensor are called the *principal stresses* and are denoted σ_1, σ_2, and σ_3. Since the stress tensor is symmetric, its eigenvectors, called *principal axes of stress*, corresponding to the principal stresses are orthogonal and provide an alternative coordinate system in which the stress tensor takes the

diagonal form

$$\sigma = \begin{pmatrix} \sigma_1 & 0 & 0 \\ 0 & \sigma_2 & 0 \\ 0 & 0 & \sigma_3 \end{pmatrix}.$$

The principal stresses are invariant under a rotation of the coordinate system relative to which the stress tensor is defined. The eigenvalues of the stress tensor, λ, are given, in the usual way, by roots of the equation

$$\det(\sigma - \lambda \mathbf{I}) = 0. \tag{2.5}$$

This leads to the characteristic equation

$$\lambda^3 + I_1\lambda^2 - I_2\lambda + I_3 = 0,$$

where

$$\begin{aligned} I_1 &= \sigma_{11} + \sigma_{22} + \sigma_{33}, \\ I_2 &= \sigma_{11}\sigma_{22} + \sigma_{22}\sigma_{33} + \sigma_{11}\sigma_{33} - \sigma_{12}^2 - \sigma_{23}^2 - \sigma_{13}^2, \\ I_3 &= \sigma_{11}\sigma_{22}\sigma_{33} + 2\sigma_{12}\sigma_{23}\sigma_{13} - \sigma_{12}^2\sigma_{33} - \sigma_{23}^2\sigma_{11} - \sigma_{13}^2\sigma_{22}. \end{aligned} \tag{2.6}$$

The I_j given by (2.6) are invariant under a rotation of the coordinates and as such are referred to as the *invariants of the stress tensor*. They can be expressed using the summation notation as

$$\begin{aligned} I_1 &= \sigma_{kk}, \\ I_2 &= \frac{1}{2}\left(\sigma_{ii}\sigma_{jj} - \sigma_{ij}\sigma_{ji}\right), \\ I_3 &= \det(\sigma_{ij}). \end{aligned}$$

The *deviatoric stress tensor* is defined as

$$s_{ij} = \sigma_{ij} - \frac{1}{3}I_1\delta_{ij}. \tag{2.7}$$

The invariants of the deviatoric stress tensor can be expressed in various forms in terms of the components of the deviatoric stress tensor, the stress tensor, the principal stresses or the invariants of the stress tensor but the relevant definitions for the current work are stated below.

$$\begin{aligned} J_1 &= s_{kk} = 0, \\ J_2 &= \frac{1}{2} s_{ij} s_{ji} \\ &= \frac{1}{6}\left[(\sigma_{11}-\sigma_{22})^2 + (\sigma_{22}-\sigma_{33})^2 + (\sigma_{11}-\sigma_{33})^2\right] + \sigma_{12}^2 + \sigma_{23}^2 + \sigma_{13}^2, \\ J_3 &= \det(s_{ij}). \end{aligned} \tag{2.8}$$

2.2 Strain

The *strain* within a body is a measure of the deformation of the material. It is defined in terms of the relative change in positions of points in the body and as such neglects rigid body motions. Infinitesimal strain theory, in which the displacements of material points are much smaller than the macroscropic length scales over which they vary, is an assumption which greatly simplifies the continuum model. In the current problem the macroscopic lengths associated with tectonic plates are of the order of tens of kilometers whereas the total displacements are only several meters; infinitesimal strain theory is therefore justified. For a detailed discussion of the infinitesimal theory see, for example Gould [1994], and for an explanation of finite strains see Hashiguchi and Yamakawa [2012].

We follow the method of Gould [1994] to define the strain but note that it is expressed here in the more conventional notation using capital letters to denote the reference configuration and lower case letters to denote the current configuration. Follow a point R on a body as it deforms from its undeformed configuration to its deformed state and label its new position r. We denote its position in a cartesian coordinate system associated with the deformed configuration by $\mathbf{X} = (X_1, X_2, X_3)$ and its position in the undeformed body is given by $\mathbf{x} = (x_1, x_2, x_3)$. For simplicity the two coordinate systems have the same origin in this thesis. The position vector of r relative to R is given by $\mathbf{x} = \mathbf{X} + \mathbf{u}(\mathbf{X})$. To characterise the strain we define

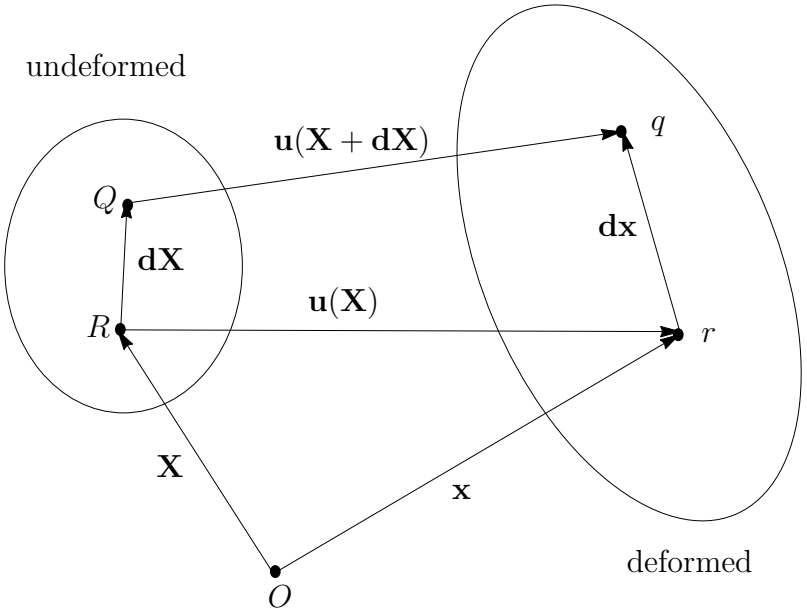

Figure 2.4: A figure showing the displacement, $\mathbf{u}(\mathbf{R})$, of a point P to $\mathcal{P}$ and the displacement, $\mathbf{u}(\mathbf{R}+\mathbf{dR})$, of a point Q to q as the body deforms from the undeformed configuration to the deformed.

a second point Q with position $\mathbf{X}+\mathbf{dX}$ in the undeformed body and

$$\mathbf{x}+\mathbf{dx} = \mathbf{X}+\mathbf{dX}+\mathbf{u}(\mathbf{X}+\mathbf{dX}),$$

is the position vector of q in the deformed body as shown in Figure 2.4. If the points R and Q are taken to be sufficiently close together that $|\mathbf{dX}|$ is small then term $\mathbf{u}(\mathbf{X}+\mathbf{dX})$ and can be approximated by its Taylor series expansion to give

$$\mathbf{x}+\mathbf{dx} = \mathbf{X}+\mathbf{dX}+\mathbf{u}(\mathbf{X})+dX_j\frac{\partial \mathbf{u}}{\partial X_j}+O(|\mathbf{dX}|^2),$$

where $\mathbf{dX} = (dX_1, dX_2, dX_3)$. Since $\mathbf{x} = \mathbf{X}+\mathbf{u}(\mathbf{X})$, the position vector of q relative to r can be expressed in terms of the position vector of Q relative R as

$$\mathbf{dx} \approx \mathbf{dX}+dX_j\frac{\partial \mathbf{u}}{\partial X_j}. \tag{2.9}$$

If the latter term is zero then the relative positions of R and Q remain unchanged

and hence the former term represents rigid body translation. The second term describes the rigid body rotation and the deformation. The i^{th} component of (2.9) can be used to define the *displacement gradient tensor*

$$\frac{\partial u_i}{\partial X_j} = \frac{dx_i - dX_i}{dX_j}. \tag{2.10}$$

The displacement gradient tensor can be decomposed into its symmetric and antisymmetric parts as

$$\frac{\partial u_i}{\partial X_j} = \frac{1}{2}\left(\frac{\partial u_i}{\partial X_j} + \frac{\partial u_j}{\partial X_i}\right) + \frac{1}{2}\left(\frac{\partial u_i}{\partial X_j} - \frac{\partial u_j}{\partial X_i}\right).$$

The symmetric part is known as the *infinitesimal strain tensor* and the antisymmetric part is the *infinitesimal rotation tensor*. They are commonly denoted ϵ_{ij} and ω_{ij} respectively and are defined explicitly below

$$\begin{aligned} \epsilon_{ij} &= \frac{1}{2}\left(\frac{\partial u_i}{\partial X_j} + \frac{\partial u_j}{\partial X_i}\right), \\ \omega_{ij} &= \frac{1}{2}\left(\frac{\partial u_i}{\partial X_j} - \frac{\partial u_j}{\partial X_i}\right). \end{aligned} \tag{2.11}$$

The former is a measure of the deformation within the body and the latter measures infinitesimal rigid body rotations.

Write the position vectors of Q relative to R and q relative to r as vectors of magnitudes dS and ds and directions $\mathbf{N}$ and $\mathbf{n}$ respectively,

$$\begin{aligned} \mathbf{dR} &= dS\mathbf{N}, \\ \mathbf{dr} &= ds\mathbf{n}. \end{aligned}$$

The magnitude of ds can be related to dS by combining these definitions with the

expression (2.9)

$$\begin{aligned} ds^2 &= \mathbf{dx}\cdot\mathbf{dx} \approx \left(\mathbf{dX} + dX_i\frac{\partial \mathbf{u}}{\partial X_i}\right)\cdot\left(\mathbf{dX} + dX_j\frac{\partial \mathbf{u}}{\partial X_j}\right) \\ &= dS^2 + dX_j dX_k\frac{\partial u_k}{\partial X_j} + dX_i dX_k\frac{\partial u_k}{\partial X_i} + dX_i dX_j\frac{\partial u_k}{\partial X_i}\frac{\partial u_k}{\partial X_j} \\ &= dS^2 + dX_i dX_j\left(\delta_{ik}\frac{\partial u_k}{\partial X_j} + \delta_{jk}\frac{\partial u_k}{\partial X_i} + \frac{\partial u_k}{\partial X_i}\frac{\partial u_k}{\partial X_j}\right) \\ &= dS^2 + dX_i dX_j\left(\frac{\partial u_i}{\partial X_j} + \frac{\partial u_j}{\partial X_i} + \frac{\partial u_k}{\partial X_i}\frac{\partial u_k}{\partial X_i}\right). \end{aligned} \tag{2.12}$$

The *Lagrangian strain tensor* is defined as

$$\epsilon^L_{ij} = \frac{1}{2}\left(\frac{\partial u_i}{\partial X_j} + \frac{\partial u_j}{\partial X_i} + \frac{\partial u_k}{\partial X_i}\frac{\partial u_k}{\partial X_i}\right). \tag{2.13}$$

Relative to an Eulerian frame of reference the position vector of R is $\mathbf{X} = \mathbf{x} - \mathbf{u}(\mathbf{x})$. The position vector of Q relative to R can be expressed in terms of the position vector of q relative r as

$$\mathbf{dX} \approx \mathbf{dx} - dx_j\frac{\partial \mathbf{u}}{\partial x_j}. \tag{2.14}$$

The analogous expression to (2.12) is then

$$ds^2 \approx dS^2 + ds_i ds_j\left(\frac{\partial u_i}{\partial x_j} + \frac{\partial u_j}{\partial x_i} - \frac{\partial u_k}{\partial x_i}\frac{\partial u_k}{\partial x_i}\right), \tag{2.15}$$

and the *Eulerian strain* is defined as

$$\epsilon^E_{ij} = \frac{1}{2}\left(\frac{\partial u_i}{\partial x_j} + \frac{\partial u_j}{\partial x_i} - \frac{\partial u_k}{\partial x_i}\frac{\partial u_k}{\partial x_i}\right). \tag{2.16}$$

For infinitesimal strains the components of the displacement gradient are small, namely $|u_{i,j} \ll 1|$, and the products of these terms may be neglected. Furthermore, to leading order the derivatives relative to the initial and final configurations are

identical. Hence

$$\frac{\partial u_i}{\partial X_j} = \frac{\partial u_i}{\partial x_j},$$

and the definitions of the Lagrangian and Eulerian strains, (2.13) and (2.16) coincide with each other and with the definition of infinitesimal strain given by (2.11). For the remainder of the thesis the term "strain" shall be used to describe the infinitesimal strain.

2.3 The Cauchy Momentum Equations and the Equilibrium Equations

Derivation of the Cauchy momentum equations appears in many texts including Muskhelishvili [1953] and Spencer [1980]; an overview is presented here for completeness. The vector valued resultant force $\mathcal{R}(V)$ on any arbitrary volume V which is bounded by the surface S can be expressed as the sum of the body forces, (2.1), and the surface forces, (2.3). The i^{th} component is then

$$\mathcal{R}_i(V) = \int_S t_i dS + \int_V \rho b_i dV.$$

Using equation (2.4) together with the divergence theorem we can write

$$\mathcal{R}_i(V) = \int_V \sigma_{ij,j} dV + \int_V \rho b_i dV,$$

where the comma denotes differentiation with respect to the following j^{th} coordinate. The left hand side can be related to the acceleration using Newton's second law to obtain

$$\int_V \rho \frac{Dv_i}{Dt} dV = \int_V \sigma_{ij,j} dV + \int_V \rho b_i dV,$$

where v is the velocity and $\frac{D}{Dt}$ is the material derivative. This equation must hold for any arbitrary volume V in the domain and so the integrands on either side can

be equated to give Cauchy momentum equations

$$\rho \frac{Dv_i}{Dt} = \sigma_{ij,j} + \rho b_i. \tag{2.17}$$

If the material is in equilibrium then the resultant force, and therefore the acceleration, is zero. The equations of equilibrium are consequently

$$\sigma_{ij,j} + \rho b_i = 0. \tag{2.18}$$

2.4 Linear Elasticity

2.4.1 Generalised Hooke's Law

Hooke's Law states that the force F required to extend a spring by an amount x is proportional to x. Namely that $F = kx$. The constant of proportionality k is the spring stiffness. The three-dimensional analogy is the generalised Hooke's law given by

$$\sigma_{ij} = E_{ijkl}\epsilon_{kl}, \tag{2.19}$$

where E_{ijkl} is a fourth order tensor containing information about the material properties. The 81 components of E_{ijkl} must satify certain constraints imposed by the symmetry of the stress and strain tensors. For example, symmetry of the stress tensor implies $E_{ijkl} = E_{jikl}$. Application of all the symmetries of the stress and strain tensors leaves 21 independent components. A homogeneous and isotropic material has the same material properties everywhere and in all directions. For such a material

$$E_{ijkl} = \lambda \delta_{ij}\delta_{kl} + 2\mu\delta_{ik}\delta_{jl}, \tag{2.20}$$

where δ_{ij} is the kronecker delta, see for example Muskhelishvili [1953]. The two parameters λ and μ are the first and second *Lamé coefficients* respectively. The second, μ, is also called the *shear modulus*. They are determined experimentally and characterise the material. Substitution of (2.20) into (2.19) produces the

generalised Hooke's law for a homogeneous and isotropic material

$$\sigma_{ij} = \lambda\delta_{ij}\epsilon_{kk} + 2\mu\epsilon_{ij}. \tag{2.21}$$

The application of a traction to a surface of a linear elastic solid causes instantaneous deformation. If, however, the applied traction is time-dependent then the material can undergo continuous time-dependent deformation. In such a situation, the partial time derivative of the generalised Hooke's law, (2.21), relates the stress-rate tensor, $\dot{\sigma}_{ij}$, to the deformation-rate tensor, d_{ij}, through the equation

$$\dot{\sigma}_{ij} = \lambda\delta_{ij}d_{kk} + 2\mu d_{ij}. \tag{2.22}$$

Here the superposed dot refers to the partial time derivative and d_{ij} is the partial time derivative of the strain tensor, namely, $d_{ij} = \dot{\epsilon}_{ij}$.

Both the temperature and pressure profiles vary continuously and in reality there is not a sharp interface between the rheology in the lithosphere and the asthenosphere. Furthermore, the material properties in the tectonic plates vary with depth. Studies of the effects of inhomogeneities have been carried out by Wang et al. [2003], Hearn and Bürgmann [2005] and Pichon et al. [2005] but are often much more complicated and without knowledge of the precise nature of the variation of the material properties are not necessarily more accurate. Consequently this thesis only relates to homogeneous and isotropic linear elasticity and consequently references to generalised Hooke's law refer to equation (2.21).

2.4.2 Strain Compatibility

The six independent components of the strain tensor are determined uniquely by the derivatives of the three components of the displacement field. The converse, however, is not true; it is not possible to specify six components of the strain tensor independently so that they correspond to a displacement field. The additional restrictions come in the form of the *compatibility equations* derived by Saint-Venant and take the form

$$\epsilon_{ij,kl} + \epsilon_{kl,ij} - \epsilon_{kl,il} - \epsilon_{il,kj} = 0.$$

If a three-dimensional body is subdivided into infinitesimal cubes then the strain tensor provides information about the deformed configuration of these cubes. The strain compatibility equations provide constraints that ensure the deformed cubes still fit together. The values of i, j, k, l that lead to non-trivial strain compatibility equations are given by the columns in the table below.

Table 2.1: The 6 Non-trivial Strain Compatibility Equations

i	1	1	1	1	1	2
j	1	1	2	1	2	2
k	2	2	2	3	3	3
l	2	3	3	3	3	3

2.5 Granular Materials

2.5.1 Yield Criterion

A *yield criterion* is a statement about the state of stress which marks the onset of plastic deformation. Often defined in the form $f(\sigma_{ij}; k) \leq 0$, for a suitably chosen *yield function* f, strict inequality occurs during pre-yield (elastic) deformation and equality holds when the material is in yield. The yield function, f, not only depends on the components of the stress tensor but can also depend on many other parameters such as the angle of internal friction and cohesion as well as those characterising the work hardening and anisotropy. These additional parameters are denoted by k. The choice of yield criterion depends on the material being considered and there have been many possibilities proposed in the literature, see for example, Nemat-Nasser and Shokooh [1980] and Lade [1977]. The three most worthy of mention for their historical importance are those by Coulomb, von Mises and Tresca. The former is a popular choice for granular materials but the latter two are more commonly applied to metal plasticity. Detailed explanations of these three are given below.

The Mohr-Coulomb yield criterion is an experimentally derived criterion that is especially relevant to soils and rock. It states that the maximum shear

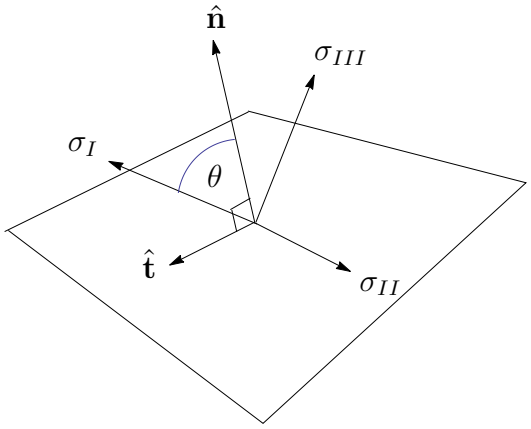

Figure 2.5: A surface in principal stress space with normal $\mathbf{n}$. The coordinate axis σ_{II} lies in the plane and the σ_I axis is orientated at an angle θ to the normal.

stress, τ_n, on any surface is limited by the normal stress, σ_n, through the equation

$$|\tau_n| \leq -\sigma_n \tan\phi + c, \tag{2.23}$$

where compressive stresses are taken to be negative. Here the material parameters ϕ and c are the angle of internal friction and the cohesion respectively. The Mohr-Coulomb yield criterion for cohesionless materials is equivalent to Coulomb friction between solid bodies with the coefficient of friction equal to $\tan\phi$.

Denote the principal stresses by σ_I, σ_{II} and σ_{III} such that $\sigma_I > \sigma_{II} > \sigma_{III}$. Consider a plane containing the σ_{II} axis and with unit normal subtending an angle θ relative to the σ_I axis as shown in Figure 2.5. The unit normal is then $\hat{\mathbf{n}} = (\cos\theta, 0, \sin\theta)$ and the tangent vector to the surface in the $\sigma_I - \sigma_{III}$ plane is written $\hat{\mathbf{t}} = (\sin\theta, 0, -\cos\theta)$. The normal and tangent components of the traction are subsequently

$$\begin{aligned} \sigma_n &= \hat{\mathbf{n}}\sigma\hat{\mathbf{n}}^T = \sigma_I \cos^2\theta + \sigma_{III}\sin^2\theta, \\ \tau_n &= \hat{\mathbf{t}}\sigma\hat{\mathbf{n}}^T = \sigma_I \cos\theta\sin\theta - \sigma_{III}\cos\theta\sin\theta, \end{aligned}$$

respectively. Using the double angle formulae for $\cos\theta$ and $\sin\theta$ these can be

expressed as

$$\begin{aligned} \sigma_n &= \frac{\sigma_I + \sigma_{III}}{2} + \frac{\sigma_I - \sigma_{III}}{2} \cos 2\theta, \\ \tau_n &= \frac{\sigma_I - \sigma_{III}}{2} \sin 2\theta, \end{aligned}$$

and the yield criterion (2.23) becomes

$$\frac{\sigma_I - \sigma_{III}}{2} |\sin 2\theta| + \frac{\sigma_I + \sigma_{III}}{2} \tan\phi + \frac{\sigma_I - \sigma_{III}}{2} \cos 2\theta \tan\phi - c \leq 0,$$

or, equivalently, since $\cos\phi > 0$

$$\frac{\sigma_I - \sigma_{III}}{2} (|\sin 2\theta| \cos\phi + \cos 2\theta \sin\phi) + \frac{\sigma_I + \sigma_{III}}{2} \sin\phi - c\cos\phi \leq 0.$$

Use of the double angle formula shows that the first term takes its maximum value of 1 when

$$\theta = \pm \left(\frac{\pi}{4} - \frac{\phi}{2} \right),$$

in which case the Mohr-Coulomb yield criterion is

$$\frac{\sigma_I - \sigma_{III}}{2} + \frac{\sigma_I + \sigma_{III}}{2} \sin\phi - c\cos\phi \leq 0. \tag{2.24}$$

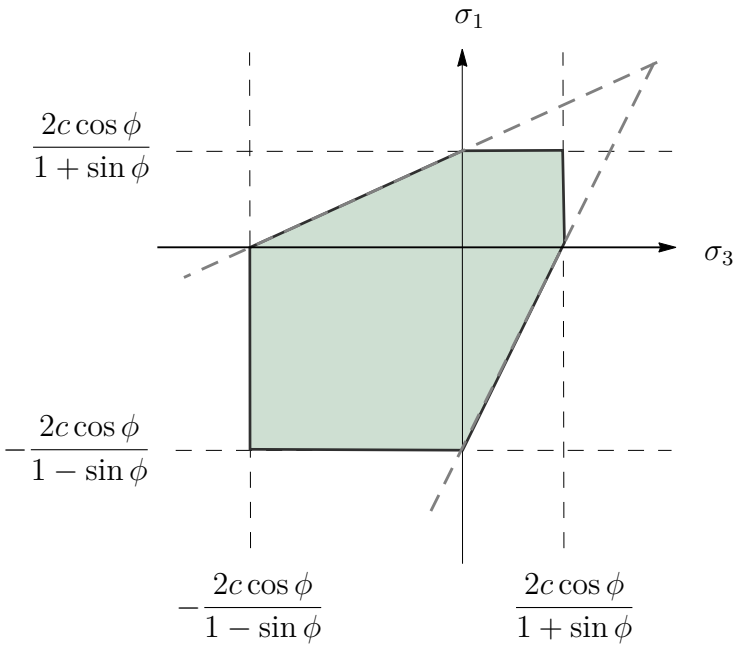

Figure 2.6: The Mohr-Coulomb yield surface in the plane defined by $\sigma_2 = 0$. The shaded irregular hexagonal region represents the admissible pre-yield stress states and the black edge lines denote the in-yield plastic states of stress.

The values of the principal stresses, σ_1, σ_2 and σ_3, will determine which one corresponds to the labels σ_I, σ_{II} and σ_{III}. There are six possibilities and consequently (2.24) represents 6 inequalities; one for each of the permutations of σ_1, σ_2 and σ_3. These can be written explicitly as

$$\begin{cases} \pm\dfrac{\sigma_1-\sigma_2}{2} - \dfrac{\sigma_1+\sigma_2}{2}\sin\phi - c\cos\phi \;\leq\; 0, \\ \pm\dfrac{\sigma_1-\sigma_3}{2} - \dfrac{\sigma_1+\sigma_3}{2}\sin\phi - c\cos\phi \;\leq\; 0, \\ \pm\dfrac{\sigma_2-\sigma_3}{2} - \dfrac{\sigma_2+\sigma_3}{2}\sin\phi - c\cos\phi \;\leq\; 0. \end{cases} \tag{2.25}$$

Taking strict equality in the middle inequality gives the equations of two intersecting straight lines in the $\sigma_1 - \sigma_3$ plane, distinguished by the plus or minus, the

equations of which are

$$\begin{aligned}\sigma_1 &= \sigma_3\left(\frac{1-\sin\phi}{1+\sin\phi}\right) - \frac{2c\cos\phi}{1+\sin\phi},\\ \sigma_1 &= \sigma_3\left(\frac{1+\sin\phi}{1-\sin\phi}\right) + \frac{2c\cos\phi}{1-\sin\phi}.\end{aligned}$$

In the plane defined by $\sigma_2 = 0$, strict equality in the first and third inequalities of (2.25) define two lines parallel to the σ_3 and σ_1 axes respectively. These are given by

$$\sigma_1 = \frac{2c\cos\phi}{\pm 1-\sin\phi}, \tag{2.26}$$

$$\sigma_3 = \frac{2c\cos\phi}{\pm 1-\sin\phi}. \tag{2.27}$$

These six lines are shown in Figure 2.6 and the boundary of the green hexagonal region represents the admissible stress states when in yield. The interior shaded region represents the region satisfying the six strict inequalities and represents all possible states of stress within the elastic phase. The stresses are not permitted to lie in the unshaded region. Equations (2.26) and (2.27) can be easily extended to planes defined by other constant values of σ_2.

Figure 2.7 is a graphical representation of all 6 inequalities given in (2.25). The surface of a hexagonal based pyramid is shaded green and shows all possible plastic stress states. Pre-yield elastic stress states fall inside the pyramid.

The Tresca yield criterion is an empirically derived approximation to the non-uniform behaviour of metals extruded through various shaped dies. Hill [1950] accredits the Tresca yield criterion as the first investigation into yielding carried out by Tresca [1864]. It states that a material reaches yield when the maximum shear stress reaches a certain value, σ_c say. Relative to the principal stresses this can be expressed in the form $\sigma_I - \sigma_{III} \leq \sigma_c$ or alternatively

$$\begin{cases} |\sigma_1 - \sigma_2| \leq \sigma_c, \\ |\sigma_1 - \sigma_3| \leq \sigma_c, \\ |\sigma_2 - \sigma_3| \leq \sigma_c. \end{cases} \tag{2.28}$$

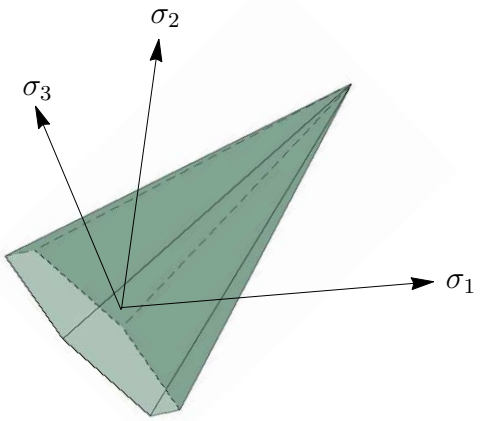

Figure 2.7: The Mohr-Coulomb yield surface in principal stress space. The surface of the hexagonal based pyramid represents the admissible stress states when in yield and the interior contains all possible pre-yield stress states.

Notice that this is a special case of the Mohr-Coulomb yield criterion (2.25) with $\phi = 0$ and $2c = \sigma_c$. In the plane $\sigma_2 = 0$, strict equality in the middle inequality of 2.28 represents the two parallel lines $\sigma_1 = \sigma_3 \pm \sigma_c$. Similarly, equality in the first and third inequalities gives the two lines $\sigma_1 = \pm\sigma_c$ parallel to the σ_3 axis and the two lines $\sigma_3 = \pm\sigma_c$ parallel to the σ_1 axis. Figure 2.8 shows these six equations as dashed lines. The boundary of the green shaded hexagonal region represents the admissible in-yield stress states and the interior depicts the pre-yield elastic stress states.

Figure 2.9 shows the yield surface in three-dimensional principal stress space which forms the surface of a hexagonal prism.

The von Mises yield criterion, von Mises [1913], states that yielding occurs when the second invariant of the deviatoric stress tensor reaches a certain value, k^2. Namely,

$$J_2 \leq k^2. \tag{2.29}$$

The expression used to define J_2 is given by (2.8). Hill [1950] provides an in-depth discussion of this yield criterion but attributes to Hencky [1924] the physical

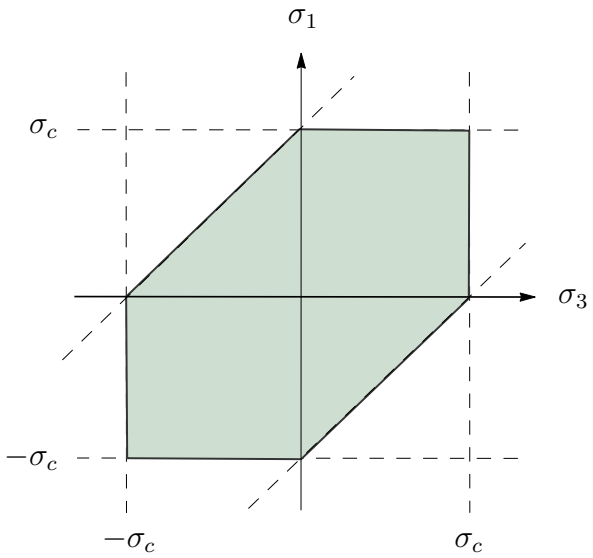

Figure 2.8: The Tresca yield surface in the plane defined by $\sigma_2 = 0$. The shaded hexagonal region represents the admissible pre-yield stress states and the black edge lines denote the in-yield plastic states of stress.

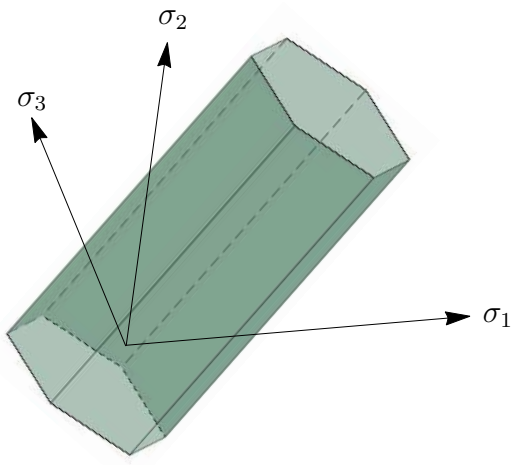

Figure 2.9: The Tresca yield surface in principal stress space. The surface of the hexagonal prism represents the admissible stress states when in yield and the interior contains all possible pre-yield stress states.

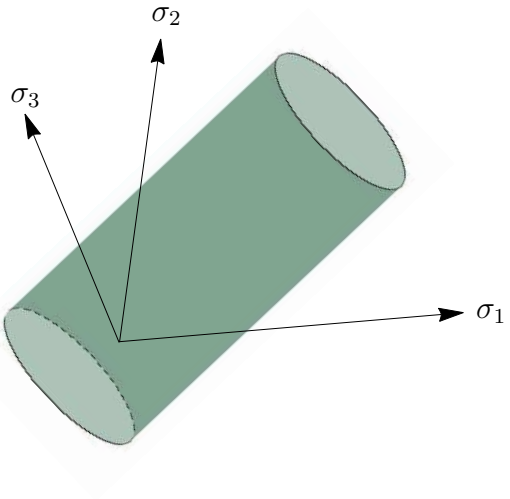

Figure 2.10: The von Mises yield surface in principal stress space. The surface of the cylinder represents the admissible stress states when in yield and the interior contains all possible pre-yield stress states.

interpretation that yielding occurs when the elastic energy of distortion reaches a critical value. Plasticity models that use the von Mises yield criterion are often referred to as J_2 plasticity. In three-dimensional principal stress space the von Mises yield criterion is an elliptical cross-sectioned tube as shown in Figure 2.10.

2.5.2 Work Hardening

As granular materials deform their grains re-order themselves relative to one another, often leading to dilatation or compaction. The change in structure leads to a change in the material properties and therefore the subsequent deformation. This can result in a change in the yield surface and such an effect is called *work-hardening* or *strain-hardening*, the two differing only in the choice of parameter which encapsulates the history of the deformation.

A material which does not undergo work-hardening is referred to as a *perfectly plastic* material and is characterised by a yield surface, such as the ones shown in the previous section, which remains fixed throughout the deformation. In a strain-hardening material the yield surface expands as the plastic strains increase. A general strain hardening yield criterion can then be expressed as $f(\sigma_{ij}; k(\epsilon^p))$.

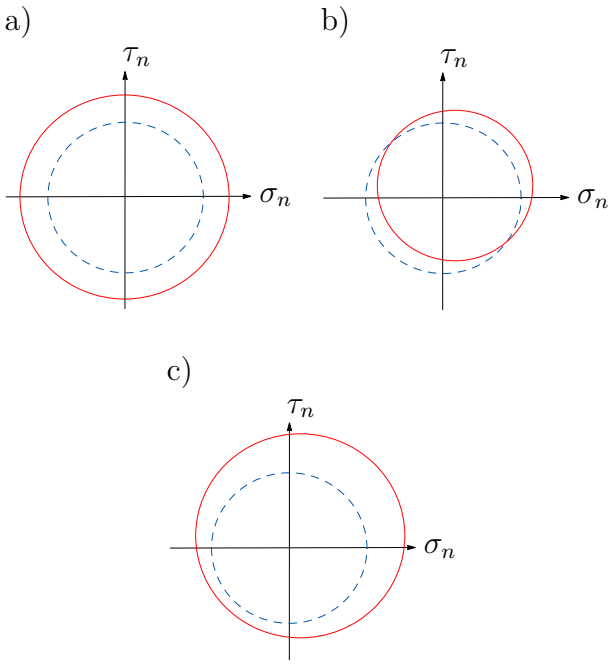

Figure 2.11: Graphical representation of 2-D work-hardening yield criterion where the dashed circle transforms into the solid red circle after the material has undergone some plastic strain. Figure a) shows an isotropic yield criterion, b) demonstrates the effect of a kinematic hardening and c) exhibits combined isotropic and kinematic work hardening behaviour.

The effect of k on the yield criterion can, in general, be decomposed into an isotropic and a kinematic constituent; although most models only encompass one or the other. Isotropic hardening sees the yield locus expand radially about its centre to enlarge but not distort its shape. This can be seen in Figure 2.11a). The dashed blue circle shows the initial yield locus and the red solid line represents its form after some plastic straining. In kinematic hardening the yield locus translates but its shape remains unchanged as demonstrated in Figure 2.11b). Figure 2.11c) shows a combined isotropic and kinematic hardening in which the yield locus enlarges and translates with increasing plastic strain. For simplicity, we employ an isotropic strain hardening model.

2.5.3 Dilatancy

The behaviour of a granular material depends significantly on the arrangement of its grains. An initially dense packing will dilate under shearing as the grains are forced up and over the lower grains. This is demonstrated in Figure 2.12 which shows a perfectly packed initial arrangement in which each row of grains is nestled among the grains in the row below. Post deformation, the grains sit on top of one another to form a rectangle of larger height than the initial parallelogram. Conversely, Figure 2.13 shows an initially loose packing in which each grain rests directly on top of its adjacent grain. After shearing the grains come to rest in between the grains on the row below. The height of such a parallelogram is less than the initial square and the material has compacted. With variations in the initial organisation of the grains causing such opposing effects the study of packing problems has drawn much attention in recent years, Nowak et al. [1997] and Nicolas et al. [2000].

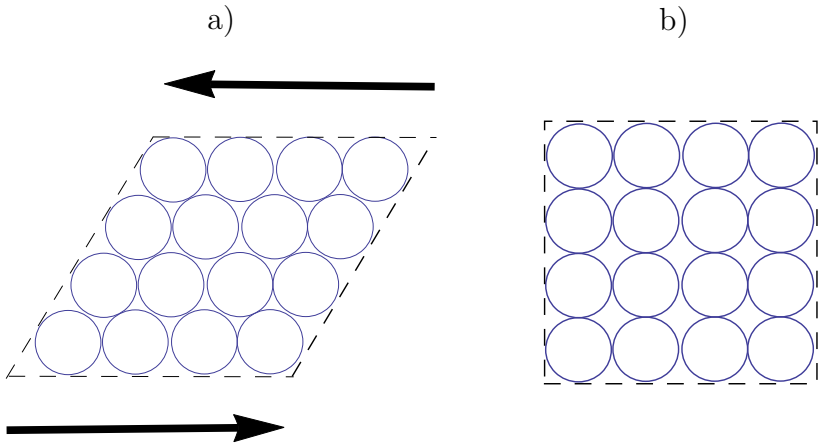

Figure 2.12: A graphical representation of dilatation in which an initial dense arrangement of grains, a), dilates when sheared to a state that occupies a larger area (volume), b).

In many situations this characteristic is limited to only the initial stages of the deformation and during a well-developed flow can often be considered negligible. A material which never dilates is referred to as *incompressible* whereas a dilatant medium which exhibits no dilatation is called *isochoric*. The dilatation is incorporated into a model through the flow rule as outlined in the following

section.

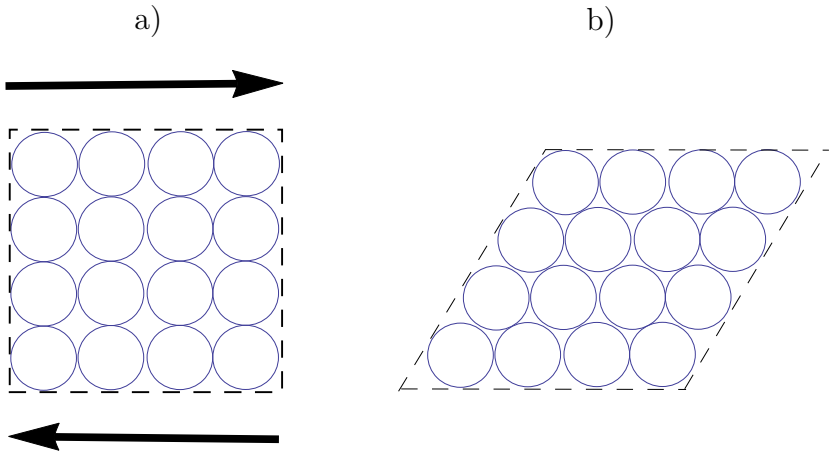

Figure 2.13: A graphical representation of compaction in which an initial loose arrangement of grains, a), dilates when sheared to a state that occupies a smaller area (volume), b).

2.5.4 Constitutive Equations

Constitutive equations relating deformation-rate to the stresses or stress-rates are multifarious and a comprehensive review is impractical. A review of the most widely used and historically significant is presented.

Many theories are based on the concept of a *plastic potential*, denoted g, which, like the yield function, depends on the stress as well as other material parameters and in general can be written $g(\sigma_{ij}; k)$. It is, however, restricted to be independent of the stress-rate. Like f, the plastic potential can be represented as a surface in stress space. The flow rule

$$d^p_{ij} = \dot{\lambda}\frac{\partial g}{\partial \sigma_{ij}}, \tag{2.30}$$

assumes that the plastic strain-rate is coaxial to the normal of the surface g. Hill [1950] suggests the necessity of coaxiality of the strain-rate and stress tensors which is widely accepted for metal plasticity but there is experimental evidence that this is not the case for soils, Roscoe et al. [1967] and Drescher and de Jong [1972]. The experiments by Roscoe [1970] found that the non-coaxiality was found to be more pronounced during the early stages of the deformation when undergoing simple shear but the principal axes of stress and strain-rate rotated to coincide at larger shear strains.

Plastic deformation is dissipative and so the rate of plastic working by the stresses, $\dot{W}$, is non-negative. Therefore, by definition of $\dot{W}$,

$$\dot{W} = \sigma_{ij} d^p_{ij} \geq 0.$$

Substiting in the flow rule, (2.30), gives

$$\dot{\lambda}\sigma_{ij}\frac{\partial g}{\partial \sigma_{ij}} \geq 0. \tag{2.31}$$

In six-dimensional stress space, the instantaneous state of stress at a point can be described by a position vector. Similarly, the normal to the surface $g = 0$ can be represented as a vector where each component is the partial derivative of g with respect to the corresponding stress component. In such a six-dimensional

space, the scalar product of the stress position vector and the normal to the surface $g = 0$ is given by $\sigma_{ij}\frac{\partial g}{\partial \sigma_{ij}}$. For the yield criterions discussed in this thesis, see Section 2.5.1, these two vectors form an acute angle and consequently their scalar product is positive. Therefore, the dissipative nature of plastic deformation stipulates that $\dot{\lambda} \geq 0$ through (2.31).

When $f = g$ the flow rule is said to be *associated*. An incompressible material requires g to be independent of the pressure since the plastic volume change can be expressed in terms of the trace of the deformation-rate tensor, which, through (2.30), requires

$$d^p_{kk} = \dot{\lambda}\frac{\partial g}{\partial \sigma_{kk}} = 0.$$

Drucker and Prager [1952] use the associated generalisation of the von Mises yield criterion

$$f = g = \sqrt{J_2} + \xi_1 I_1 - \xi_2,$$

where ξ_1 and ξ_2 are material parameters which can be expressed in terms of the angle of internal friction and cohesion in the Mohr-Coulomb yield criterion as

$$\begin{aligned} \xi_1 &= -\frac{6c\cos\phi}{\sqrt{3}(3 \pm \sin\phi)}, \\ \xi_2 &= \frac{2\sin\phi}{\sqrt{3}(3 \pm \sin\phi)}. \end{aligned}$$

The plus or minus determines whether the yield surface circumscribes or inscribes the Mohr-Coulomb yield surface, Doran et al. [1998] and Ivorra et al. [2010]. The dilatation is equal to the angle of internal friction but according to Spencer [1964] this overestimates the dilation experienced during experiments.

Plane-deformation models incorporating a Mohr-Coulomb yield condition have been proposed by Harris [1993], Coombs and Crouch [2010], Paterson and Wong [1977] and Hermann et al. [1997] which use a non-associated flow rule whose plastic potential is similar to the Mohr-Coulomb yield criterion but the angle of internal friction is replaced by the angle of dilatation, ν. These use a plastic potential of

the form

$$g = q - p \sin \nu,$$

where p and q are defined as

$$\begin{aligned} p &= -\frac{1}{2}(\sigma_{11} + \sigma_{22}), \\ q &= \frac{1}{2}\sqrt{(\sigma_{11} - \sigma_{22})^2 + 4\sigma_{12}^2}. \end{aligned}$$

Here the third coordinate axis, z, points out of the plane of deformation.

Spencer [1964] builds on the work by de Jong [1959] to construct kinematic equations for a rigid-perfectly plastic, incompressible Mohr-Coulomb material in plane deformation. The equations assume that deformation occurs by shear along a pair of stress characteristics, hence its name the *double shearing model*. Define the angle between the largest principal stress and the x axis by ψ, given by the expression

$$\tan 2\psi = \frac{2\sigma_{12}}{\sigma_{11} - \sigma_{22}}.$$

The two characteristics, termed α and β lines, are given by

$$\begin{aligned} \frac{dy}{dx} &= \tan(\psi - \frac{1}{4}\pi - \frac{1}{2}\phi), \\ \frac{dy}{dx} &= \tan(\psi + \frac{1}{4}\pi + \frac{1}{2}\phi), \end{aligned}$$

The proposed kinematic equation is

$$\sin 2\psi \left(\frac{\partial u}{\partial x} - \frac{\partial v}{\partial y}\right) - \cos 2\psi \left(\frac{\partial u}{\partial y} + \frac{\partial u}{\partial y}\right) - \sin \phi \left(\frac{\partial u}{\partial y} + \frac{\partial v}{\partial x} + 2\frac{D\psi}{Dt}\right) = 0,$$

where (u, v) is the in-plane velocity field. This equation appears in addition to the two non-trivial equilibrium equations, the Mohr-Coulomb yield criterion and the incompressibility condition $\nabla \cdot (u, v) = 0$.

Two different methods have been employed to extend this theory to incorporate dilatancy by Spencer and Kingston [1973] and Mehrabadi and Cowin [1978]. The

former replaces the incompressibility with the continuity equation for the density ρ,

$$\frac{\partial u}{\partial x} + \frac{\partial v}{\partial y} + \frac{1}{\rho}\frac{D\rho}{Dt} = 0.$$

The latter modifies Spencer's kinematic equation to give

$$\cos\nu \left[\sin 2\psi \left(\frac{\partial u}{\partial x} - \frac{\partial v}{\partial y}\right) - \cos 2\psi \left(\frac{\partial u}{\partial y} + \frac{\partial u}{\partial y}\right)\right] - \sin(\phi - \nu)\left(\frac{\partial u}{\partial y} - \frac{\partial v}{\partial x} + 2\frac{D\psi}{Dt}\right) = 0,$$

and replaces the incompressibility condition by the equation

$$\sin\nu \left[\left(\frac{\partial u}{\partial x} - \frac{\partial v}{\partial y}\right)\cos 2\psi + \left(\frac{\partial u}{\partial y} + \frac{\partial u}{\partial y}\right)\sin 2\psi\right] - \left(\frac{\partial u}{\partial x} + \frac{\partial v}{\partial y}\right)\cos(\phi - \nu) = 0.$$

The work by Harris [1993] and Harris [1995] creates one unified theory which incorporates both the plastic potential and the double shearing models. Harris [1992] further demonstrates that the model encapsulates several other models including that by Hill [1950].

Chapter 3

Background: Theory of Finite Differences

A *boundary value problem* consists of a differential equation for an unknown $\mathbf{u}(\mathbf{x})$ and boundary conditions that stipulate values of $\mathbf{u}(\mathbf{x})$ or its derivatives on the boundary of the domain. For all but the simplest of equations and of domains it is not possible to find an analytical solution to the boundary value problem and in such circumstances a numerical method must be implemented to find a numerical solution, denoted $\mathbf{u}_h$, that approximates the exact solution. The focus of this thesis is on homogeneous, linear boundary value problems with one unknown and only these shall be discussed here. For a study of a wider class of problems see, for example, Courant and Hilbert [1962].

The first step towards finding a numerical solution is to divide the continuous domain and equations into a finite number of discrete counterparts. This process is referred to as discretisation. The domain is discretised into a finite number of grid points or nodes and these are joined by edges. Collectively the grid points and edges are referred to as a mesh. Examples of meshes are shown in Figure 3.1 and the n-gon shapes created by the edges have the same value of n across the domain. A mesh which resembles a tiling of the domain by polygons of a single size and shape is called a regular mesh.

A numerical scheme is implemented to calculate information about $\mathbf{u}_h$ at the grid points only. We denote a representative distance between neighbouring grid

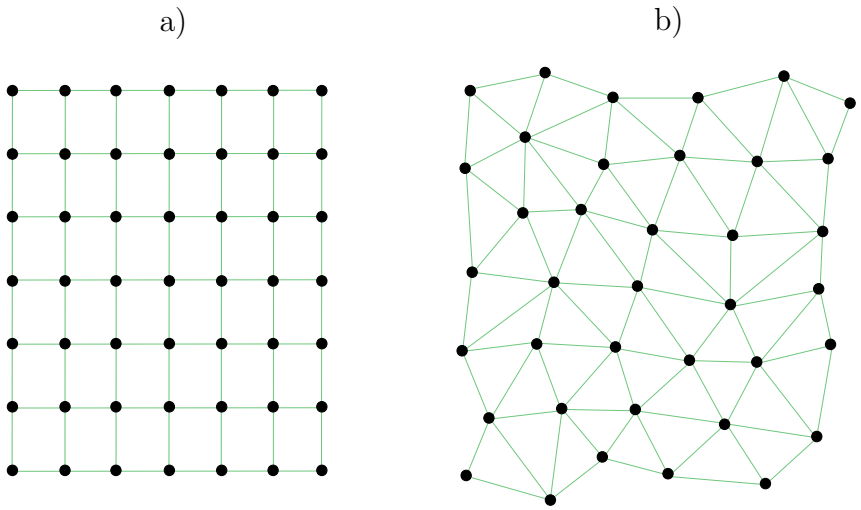

Figure 3.1: A figure showing examples of meshes. The black dots are the nodes and the edges are shown in green. Figure a) shows a regular rectangular mesh usually associated with the finite difference method and b) shows an irregular triangular mesh commonly used with the finite element method.

points by h so that the numerical solution depends on the grid spacing. The scheme should be constructed so that $\mathbf{u}_h$ converges on the actual solution as the distance between neighbouring grid points decreases. Mathematically, this is expressed as $||\mathbf{u}_h - \mathbf{u}|| \to 0$ as $h \to 0$, where $||\cdot||$ represents a suitable norm. The definition of h must therefore decrease uniformly across the domain as the mesh is refined. The rate of convergence is given by the largest value of n for which $||\mathbf{u}_h - \mathbf{u}|| < \frac{M}{h^n}$, for some constant M. Linear convergence has a value $n = 1$ and if $n = 2$ then the numerical scheme converges quadratically.

Two of the most commonly implemented numerical schemes are the *finite difference method* (FDM) and the *finite element method* (FEM). The FEM formulates the problem as an integral equation and approximates the solution by polynomials in each of the polygonal subdomains of the mesh outlined by the edges. The FDM approximates the derivatives in the differential equation by linear combinations of the nodal values of $\mathbf{u}_h$ and as such the edges of the mesh are of no consequence. The FDM has the advantage of being more intuitive and simpler to implement when applied to rectangular domains, Jing and Hudson [2002] and Ozisik [1994].

In contrast, the FEM can provide a better approximation for the solution in irregular shaped domains with curved boundaries and for inhomogeneous materials but it is more complicated to implement. Commercial FEM packages are available, such as ABAQUS, which hide the complexities of the implementation behind an easy to use user interface. This thesis is concerned with homogenous materials in rectangular domains for which the FDM is ideal. The elasto-plastic boundary adds some complexity but not sufficient to necessitate a more complicated numerical model to be implemented globally. Furthermore, we wish to investigate in detail the plastic behaviour of the fault material and wish to have more flexibility than is offered by commercial packages.

This section presents a brief introduction to the finite difference method with the main intention of deriving the finite difference approximations to the first and second derivatives which are used later in the work. The finite difference expressions on regular domains are included for completeness and to make the thesis self-contained whereas the approximations over irregular meshes are less common in the literature. For a more detailed discussion and alternative methods for deriving finite difference approximations see, for example Smith [1985].

3.1 Regular Meshes

Expressions for the finite difference approximations to the derivatives can be obtained using Taylor series expansions of the unknown functions to replace derivatives with expressions involving the values of the functions only. Consider a function $f(x)$ defined over a discretised domain with grid spacing δ. The Taylor series expansion of a function $f(x)$ are

$$f(x-\delta) = f(x) - \delta f'(x) + \frac{\delta^2}{2} f''(x) - \frac{\delta^3}{3!} f'''(x) + O(\delta^4), \tag{3.1}$$

$$f(x+\delta) = f(x) + \delta f'(x) + \frac{\delta^2}{2} f''(x) + \frac{\delta^3}{3!} f'''(x) + O(\delta^4). \tag{3.2}$$

The first can be rearranged to give an expression for the first derivative,

$$f'(x) = \frac{f(x) - f(x-\delta)}{\delta} + O(\delta). \tag{3.3}$$

By approximating the first derivative by

$$f'(x) \approx \frac{f(x) - f(x-\delta)}{\delta}, \tag{3.4}$$

we have neglected terms of order $O(\delta)$. This is referred to as a *first order* finite difference due to the errors being order $O(\delta)$. Furthermore, it is a *backwards* difference owing to the $f(x-\delta)$ term which is the value of f at the neighbouring grid point in the negative x direction. A similar first order *forwards* difference can be obtained from the Taylor expansion of $f(x+\delta)$, given by (3.2), thus

$$f'(x) \approx \frac{f(x+\delta) - f(x)}{\delta}. \tag{3.5}$$

First order differences are often straightforward to implement, however, their accuracy only being of order $O(\delta)$ often requires smaller grid spacings and thus more dense meshes and longer computational time.

A second order *centred* difference can be obtained by subtracting the Taylor series expansion (3.1) from (3.2) to obtain

$$f(x+\delta) - f(x-\delta) = 2\delta f'(x) + O(\delta^3), \tag{3.6}$$

and rearranging to give the first derivative

$$f'(x) = \frac{f(x+\delta) - f(x-\delta)}{2\delta} + O(\delta^2).$$

Neglecting the $O(\delta^2)$ terms gives the *second order* accurate centred finite difference for the first derivative

$$f'(x) \approx \frac{f(x+\delta) - f(x-\delta)}{2\delta}. \tag{3.7}$$

This is referred to as a *centred difference* due to the evaluation of the function f at neighbouring points in both the positive and negative x directions. The errors here are of an order less than in the first order differencing leading to better convergence with fewer grid points.

Although centred differences have smaller errors it is not always possible to

avoid using one-sided differences. The convergence of the overall system depends on the largest errors in the finite difference scheme across all grid points and so using a first order difference at just a few points will change the convergence of the entire scheme. Second order one-sided differences can be obtained using a Taylor expansion at additional grid points, namely

$$f(x-2\delta) = f(x) - 2\delta f'(x) + 2\delta^2 f''(x) - \frac{4\delta^3}{3} f'''(x) + O(\delta^4), \tag{3.8}$$

$$f(x+2\delta) = f(x) + 2\delta f'(x) + 2\delta^2 f''(x) + \frac{4\delta^3}{3} f'''(x) + O(\delta^4). \tag{3.9}$$

Eliminating $f''(x)$ between (3.1) and (3.8) yields

$$f(x-2\delta) - 4f(x-\delta) = -3f(x) + 2\delta f'(x) + O(\delta^3),$$

which can be rearranged to give the backwards difference for first derivative

$$f'(x) \approx \frac{3f(x) - 4f(x-\delta) + f(x-2\delta)}{2\delta}. \tag{3.10}$$

The errors here are of order $O(\delta^2)$ as required for second order accuracy. The analogous forwards difference can be obtained in a similar manner using (3.2) and (3.9).

$$f'(x) \approx \frac{-3f(x) + 4f(x+\delta) - f(x+2\delta)}{2\delta}. \tag{3.11}$$

Equivalent expressions with errors of any order can be obtained using the same method with Taylor expansions for $f(x-n\delta)$ and $f(x+n\delta)$ for $n \geq 3$.

Finite difference approximations for higher order derivatives can also be derived. Addition of equations (3.1) and (3.2) yields

$$f(x-\delta) + f(x+\delta) = 2f(x) + \delta^2 f''(x) + O(\delta^4).$$

This can be rearranged to give a second order centred difference for the second

derivative

$$f''(x) \approx \frac{f(x+\delta) - 2f(x) + f(x-\delta)}{\delta^2}. \tag{3.12}$$

The finite difference expressions (3.7), (3.10), (3.11) and (3.12) can trivially be extended into two dimensions and modified for y derivatives. For example

$$\frac{\partial f}{\partial x}(x,y) \approx \frac{f(x+\delta,y) - f(x-\delta,y)}{2\delta}, \tag{3.13}$$

$$\frac{\partial f}{\partial y}(x,y) \approx \frac{f(x,y+\epsilon) - f(x,y-\epsilon)}{2\epsilon}, \tag{3.14}$$

$$\frac{\partial^2 f}{\partial y^2}(x,y) \approx \frac{f(x,y+\epsilon) - 2f(x,y) + f(x,y-\epsilon)}{\epsilon^2}, \tag{3.15}$$

where ϵ is the grid spacing in the y direction. The errors here of order $O(\delta^2)$ and $O(\epsilon^2)$ for the x and y derivatives respectively. A scheme which approximates both x and y derivatives will therefore have its accuracy depending on both δ and ϵ.

In addition to the second y derivative given by (3.15) and the analogous x derivative the mixed derivative can be approximated by a finite difference expression. This can be seen as a sequence of first derivatives and its finite difference expression can be constructed in stages using (3.13) and (3.14).

$$\begin{aligned}
\frac{\partial^2 f}{\partial x \partial y} &= \frac{\partial}{\partial y}\frac{\partial f}{\partial x} \\
&= \frac{\partial}{\partial y}\frac{f(x+\delta,y) - f(x-\delta,y)}{2\delta} + O(\delta^2) \\
&\approx \frac{f(x+\delta,y+\epsilon) - f(x+\delta,y-\epsilon) - f(x-\delta,y+\epsilon) + f(x-\delta,y-\epsilon)}{4\delta\epsilon}.
\end{aligned}$$

This is the second order centred difference for the first mixed derivative but this maybe modified for one-sided differences using the two-dimensional equivalents of (3.10) and (3.11). Higher order mixed derivatives can be achieved in a similar manner using the finite difference forms of the higher x and y derivatives such as (3.15).

3.2 Irregular Meshes

The theory presented in the previous section relates specifically to discretisations with equally spaced grid points in each of the x and y directions. It can, however, be extended to situations where irregularly spaced grids are necessary. Denote the grid spacing about the point x as δ_1 and δ_2 in the negative and positive x directions respectively, as shown in Figure 3.2.

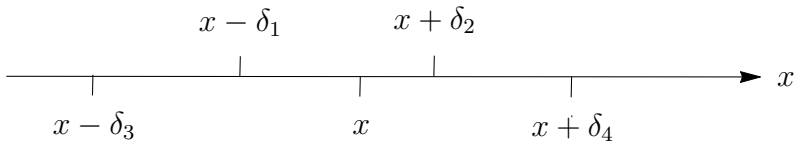

Figure 3.2: The relative positions of the irregularly spaced x coordinates about which f is expanded on a number line.

The Taylor expansions at the neighbouring points to x are

$$f(x-\delta_1) = f(x) - \delta_1 f'(x) + \frac{\delta_1^2}{2} f''(x) - \frac{\delta_1^3}{3!} f'''(x) + O(\delta_1^4), \tag{3.16}$$

$$f(x+\delta_2) = f(x) + \delta_2 f'(x) + \frac{\delta_2^2}{2} f''(x) + \frac{\delta_2^3}{3!} f'''(x) + O(\delta_2^4). \tag{3.17}$$

Elliminating the $f''(x)$ terms and rearranging gives the second order centred finite difference for the first derivative

$$f'(x) \approx \frac{(\delta_2^2 - \delta_1^2)\, f(x) + \delta_1^2 f(x+\delta_2) - \delta_2^2 f\,(x-\delta_1)}{\delta_1 \delta_2\, (\delta_1 + \delta_2)}, \tag{3.18}$$

which reduces to (3.7) in the limit $\delta_1 \to \delta_2$. The accuracy of such expressions is $O(\delta_1 \delta_2)$. Denote the coordinates of the neighbouring grid point of $x - \delta_1$ in the negative x direction by $x - \delta_3$. The Taylor expansion of f at this point is

$$f(x-\delta_3) = f(x) - \delta_3 f'(x) + \frac{\delta_3^2}{2} f''(x) - \frac{\delta_3^3}{3!} f'''(x) + O(\delta_3^4), \tag{3.19}$$

which can be combined with (3.16) to give the second order backwards difference

$$f'(x) \approx \frac{(\delta_1^2 - \delta_3^2)\, f(x) - \delta_1^2 f(x-\delta_3) + \delta_3^2 f\,(x-\delta_1)}{\delta_1 \delta_3\, (\delta_1 - \delta_3)}, \tag{3.20}$$

with accuracy $O(\delta_1\delta_3)$. Similarly, if the coordinates of the next grid point to $(x+\delta_2, y)$ in the positive x direction is denoted $(x+\delta_4, y)$ then the second order forwards difference is

$$f'(x) \approx \frac{(\delta_4^2 - \delta_2^2)\, f(x) + \delta_2^2 f\,(x+\delta_4) - \delta_4^2 f(x+\delta_2)}{\delta_2\delta_4\,(\delta_2 - \delta_4)}, \tag{3.21}$$

in which we have neglected terms of order $O(\delta_2\delta_4)$.

In the derivation of the finite difference approximation to the second order second derivative (3.12), the elimination of $f'''(x)$ between (3.1) and (3.2) also removes the $f'(x)$ terms. Eliminating $f'''(x)$ between (3.16) and (3.17) yields

$$\begin{aligned} \delta_2^3 f(x-\delta_1) + \delta_1^3 f(x+\delta_2) &= (\delta_1^3 + \delta_2^3) f(x) + (\delta_2\delta_1^3 - \delta_1\delta_2^3) f'(x) \\ &\quad + \frac{1}{2}(\delta_1^2\delta_2^3 + \delta_2^2\delta_1^3) f''(x) + O(\delta_1^3\delta_2^3), \end{aligned} \tag{3.22}$$

in which the $f'(x)$ terms are still present. To remove such terms and still obtain a second order difference it is necessary to utilize the Taylor expansions for $f(x-\delta_3)$ or $f(x+\delta_4)$. Eliminating $f'''(x)$ between (3.17) and (3.19) yields

$$\begin{aligned} \delta_2^3 f(x-\delta_3) + \delta_3^3 f(x+\delta_2) &= (\delta_2^3 + \delta_3^3) f(x) + (\delta_2\delta_3^3 - \delta_3\delta_2^3) f'(x) \\ &\quad + \frac{1}{2}(\delta_3^2\delta_2^3 + \delta_2^2\delta_3^3) f''(x) + O(\delta_2^3\delta_3^3). \end{aligned} \tag{3.23}$$

The $f'(x)$ terms can now be cancelled using (3.22) and (3.23) to give the second order accurate expression for the second derivative

$$\begin{aligned} f''(x) \approx\ & 2\left(\frac{\delta_2 - \delta_1 - \delta_3}{\delta_1\delta_2\delta_3}\right) f(x) \\ & + 2\left(\frac{\delta_2 - \delta_3}{\delta_1(\delta_1+\delta_2)(\delta_1-\delta_3)}\right) f(x-\delta_1) \\ & + 2\left(\frac{\delta_1 + \delta_3}{\delta_2(\delta_1+\delta_2)(\delta_2+\delta_3)}\right) f(x+\delta_2) \\ & + 2\left(\frac{\delta_1 - \delta_2}{\delta_3(\delta_2+\delta_3)(\delta_1-\delta_3)}\right) f(x-\delta_3). \end{aligned} \tag{3.24}$$

This could equally be derived using the Taylor expansion for $f(x+\delta_4)$ to arrive

at the expression

$$\begin{aligned} f''(x) \;\approx\; & 2\left(\frac{\delta_1-\delta_2-\delta_4}{\delta_1\delta_2\delta_4}\right) f(x) \\ & +2\left(\frac{\delta_2+\delta_4}{\delta_1(\delta_1+\delta_2)(\delta_1+\delta_4)}\right) f(x-\delta_1) \\ & +2\left(\frac{\delta_1-\delta_4}{\delta_2(\delta_1+\delta_2)(\delta_2-\delta_4)}\right) f(x+\delta_2) \\ & +2\left(\frac{\delta_2-\delta_1}{\delta_4(\delta_2-\delta_4)(\delta_1+\delta_4)}\right) f(x+\delta_4). \end{aligned} \tag{3.25}$$

Chapter 4

Background: Classifying PDEs

Partial differential equations (PDEs) contain one or more unknown dependent variables and their derivatives with respect to two or more independent variables. Several PDEs are required to find the unknowns for problems containing multiple dependent variables. Like ordinary differential equations, PDEs can be classed as linear, quasi-linear or non-linear but they can also be classified as either hyperbolic, parabolic or elliptic. Their method of solution as well as the required number of boundary conditions is often determined by their type. Therefore, it is important to ascertain such information about a PDE before trying to solve it.

In this thesis we only deal with homogeneous PDEs with 2 independent variables and for simplicity the theory reviewed in this chapter is limited to functions of x and y. For a broader class of problems see, for example Pinchova and Rubinstein [2005] and Agarwal and O'Regan [2009]. A general PDE for one unknown, $u(x, y)$, can be expressed in the form

$$F(x, y, u, u_x, u_y, u_{xx}, u_{yy}, u_{xy}, ...) = 0. \tag{4.1}$$

The subscripts denote differentiation with respect to the specified variable. The order of a PDE is given by the highest order partial derivative. Denote the order of F by n. If F is a linear combination of u and its derivatives with coefficients that are functions of x and y only then equation (4.1) is described as *linear*. If n^{th} order derivatives appear only as a linear combination, with coefficients which depend on some lower order derivatives as well as explicitly on x and y, then the PDE is

called *quasi-linear*. An equation which is neither linear nor quasi-linear is referred to as *non-linear*. The theory reviewed in the proceeding sections is presented in relation to linear PDEs but the theory is also applicable to quasi-linear equations.

4.1 A Single First Order Equation

Consider a single linear, first order partial differential equation

$$a(x,y)\frac{\partial u}{\partial x} + b(x,y)\frac{\partial u}{\partial y} = c(x,y), \tag{4.2}$$

for known continuous functions a, b and c. Suppose the solution can be written in terms of a single variable, s say. Then by the chain rule

$$\frac{du}{ds} = \frac{\partial u}{\partial x}\frac{dx}{ds} + \frac{\partial u}{\partial y}\frac{dy}{ds}. \tag{4.3}$$

Along a curve parameterised by s, such that $x = x(s)$ and $y = y(s)$ satisfy

$$\frac{dx}{ds} = a(x(s), y(s)), \qquad \frac{dy}{ds} = b(x(s), y(s)), \tag{4.4}$$

then the chain rule (4.3) reduces the PDE, (4.2), to the ODE

$$\frac{du}{ds} = c(x(s), y(s)), \tag{4.5}$$

which can be integrated subject to a suitable initial condition for s. The system of ODEs given by (4.4) and (4.5) are called the *characteristic equations* and the parameterised curve defined by the coordinates $(x(s), y(s), u(s))$ is called the *characteristic curve*. There are infinitely many such curves, each distinguished by a parameter, s_0 say, which is constant along a given characteristic and any point in the domain lies on exactly one characteristic curve.

We offer now a geometric interpretation of the above theory. Consider a surface, S, in three dimensional (x, y, u) space given by $u = \zeta(x, y)$, the normal to which is $\mathbf{n} = \nabla(\zeta(x,y) - u) = \left(\frac{\partial \zeta}{\partial x}, \frac{\partial \zeta}{\partial y}, -1\right)$. The PDE, (4.2), can therefore be written as $(a, b, c) \cdot \mathbf{n} = 0$. Geometrically this implies that the vector (a, b, c) is tangential

to S. The system of ODEs given by (4.4) and (4.5) ensure that for an initial condition on $u = \zeta(x, y)$ the $(x(s), y(s), u(s))$ coordinates evolve in such a manner that the characteristics remain on S. Suitable initial conditions are of the form $x(s = 0) = x_0$, $y(0) = y_0$ and $u(0) = u_0$ where (x_0, y_0, u_0) lie on S.

It is apparent from the geometrical interpretation that equation (4.2) only provides information about how u evolves on S since the characteristics lie in S. Consequently, given initial conditions (x_0, y_0, u_0) on S it is not possible to ascertain how u varies in the normal direction. Namely, the partial derivatives in $\mathbf{n}$ cannot be determined uniquely. For an alternative derivation of the characteristics using this explanation consider the additional equation given by the differential

$$du = \frac{\partial u}{\partial x}dx + \frac{\partial u}{\partial y}dy. \tag{4.6}$$

This represents an infinitesimal line segment which, when solved simultaneously with (4.2), lies on S. To solve these simultaneously write them in matrix form as

$$\begin{pmatrix} dx & dy \\ a & b \end{pmatrix} \begin{pmatrix} \dfrac{\partial u}{\partial x} \\ \dfrac{\partial u}{\partial y} \end{pmatrix} = \begin{pmatrix} du \\ c \end{pmatrix}. \tag{4.7}$$

The partial derivatives $\dfrac{\partial u}{\partial x}$ and $\dfrac{\partial u}{\partial y}$ and consequently $\dfrac{\partial \zeta}{\partial x}$ and $\dfrac{\partial \zeta}{\partial y}$ are uniquely determined unless the determinant of the coefficient matrix is zero. Thus

$$\begin{vmatrix} dx & dy \\ a & b \end{vmatrix} = bdx - ady = 0.$$

This can be rearranged to give $\frac{dy}{dx} = \frac{b}{a}$ which is equivalent to (4.4). For single first order PDEs the characteristic equations can be easily obtained straight from the PDE analogous to (4.2) but for systems of first order equations it is less trivial and equating the determinant of the coefficient matrix to zero provides a more robust method.

4.2 A System of First Order PDEs

In this section we extend the theory from the previous section to systems of first order PDEs. Consider the two PDEs

$$\begin{aligned} a_1(x,y)\frac{\partial u}{\partial x} + b_1(x,y)\frac{\partial u}{\partial y} + a_2(x,y)\frac{\partial v}{\partial x} + b_2(x,y)\frac{\partial v}{\partial y} &= c(x,y), \\ A_1(x,y)\frac{\partial u}{\partial x} + B_1(x,y)\frac{\partial u}{\partial y} + A_2(x,y)\frac{\partial v}{\partial x} + B_2(x,y)\frac{\partial v}{\partial y} &= C(x,y), \end{aligned} \tag{4.8}$$

for $u(x,y)$ and $v(x,y)$ where the coefficients a_i, b_i, A_i, B_i, c and C are continuous functions of x and y. These can be augmented by the differentials

$$\begin{aligned} du &= \frac{\partial u}{\partial x}dx + \frac{\partial u}{\partial y}dy, \\ dv &= \frac{\partial v}{\partial x}dx + \frac{\partial v}{\partial y}dy, \end{aligned}$$

and the characteristics are given by the determinant

$$\begin{vmatrix} dx & dy & 0 & 0 \\ 0 & 0 & dx & dy \\ a_1 & b_1 & a_2 & b_2 \\ A_1 & B_1 & A_2 & B_2 \end{vmatrix} = 0.$$

When expanded out this determinant will give a quadratic in $\frac{dy}{dx}$. If there are two distinct real roots then the system of equations (4.8) is called hyperbolic. The two roots give two families of characteristics and one and only one member of each family passes through each point in the domain. A parabolic equation has only one distinct root and if there are two distinct complex roots then the system of equations is elliptic.

For systems of many PDEs it can be impractical to calculate the determinant of such large matrices. The system of equations can be classified and possible characteristic equations obtained using the symbol of a differential equation given by Renardy and Roberts [2005] and an outline is given below. The advantage of this method is that without the differentials the coefficient matrices are of half the

size in each dimension.

Introduce two vector quantities

$$\mathbf{v} = \begin{pmatrix} u \\ v \end{pmatrix}, \qquad \mathbf{c} = \begin{pmatrix} c \\ C \end{pmatrix}, \tag{4.9}$$

and the matrices

$$\alpha = \begin{pmatrix} a_1 & b_1 \\ A_1 & B_1 \end{pmatrix}, \qquad \beta = \begin{pmatrix} a_2 & b_2 \\ A_2 & b_2 \end{pmatrix}, \tag{4.10}$$

so that the system of PDEs, (4.8), can be expressed in matrix form as

$$\alpha \frac{\partial \mathbf{v}}{\partial x} + \beta \frac{\partial \mathbf{v}}{\partial y} = \mathbf{c}. \tag{4.11}$$

The differential operator is denoted $\mathcal{L}$ and is given by

$$\mathcal{L} = \alpha \frac{\partial}{\partial x} + \beta \frac{\partial}{\partial y}, \tag{4.12}$$

so that the system of PDEs can be written $\mathcal{L}\mathbf{v} = \mathbf{c}$.

Relabel the partial derivatives with respect to x and y by

$$\frac{\partial}{\partial x} \mapsto i\xi_1, \qquad \frac{\partial}{\partial y} \mapsto i\xi_2,$$

where $i = \sqrt{-1}$, so that the vectorised PDE, (4.11), reduces to

$$i(\alpha\xi_1 + \beta\xi_2)\mathbf{v} = \mathbf{c}.$$

The matrix premultiplier $i(\alpha\xi_1 + \beta\xi_2)$ is called the symbol of the differential operator $\mathcal{L}$ given by (4.12). The classification and potential characteristics are given by equating the determinant of the symbol to zero. For the system (4.8) this is

$$\begin{vmatrix} a_1\xi_1 + a_2\xi_2 & b_1\xi_1 + b_2\xi_2 \\ A_1\xi_1 + A_2\xi_2 & B_1\xi_1 + B_2\xi_2 \end{vmatrix} = 0.$$

It is evident that this method only requires the calculation of the determinant of a 2×2 matrix as opposed to the 4×4 matrix of the previous method. The resulting quadratic, or higher order polynomial for other systems, can be expressed as a polynomial in $\frac{dy}{dx}$ using the identity $\frac{dy}{dx} = -\frac{\xi_1}{\xi_2}$. The characteristics are given by the roots of this equation and the classification is as previously discussed.

4.3 A Single Linear Second Order Partial Differential Equation

Consider the second order partial differential equation for $u(x, y)$

$$a(x,y)\frac{\partial^2 u}{\partial x^2} + 2b(x,y)\frac{\partial^2 u}{\partial x \partial y} + c(x,y)\frac{\partial^2 u}{\partial y^2} + f(u_x, u_y, u) = 0.$$

Here, the function f represents the lower order terms and the coefficients $a(x, y)$, $b(x, y)$ and $c(x, y)$ are known and are continuous. The classification of second order or higher PDEs depend only on the highest order derivatives; in the above example these are the three second derivatives. The combination of coefficients $b^2 - ac$ is called the *discriminant* and its value determines the type of the equation. If $b^2 - ac < 0$ then the equation in *elliptic*. In the case where the discriminant is identically zero, $b^2 - ac = 0$, the equation is described as *parabolic*. Positive values of the discriminant, $b^2 - ac > 0$, occur for *hyperbolic* equations. Some equations, most notably the Euler-Tricomi equation, change type in different regions of the domain depending on the values of the coefficients. Elliptic and parabolic equations are frequently solved with numerical schemes such as the finite difference or the finite element methods whereas hyperbolic equations are usually reduced to a system of first order equations and solutions obtained by integrating along the characteristics. This often has to be done numerically.

Chapter 5

The Model

5.1 The Geometry

In this chapter we encapsulate the physical problem of earthquake faulting into a mathematical formulation.

Figure 1.4 from Chapter 1 is repeated as Figure 5.1 for convenience. Define the cartesian coordinate system (x, y, z) with the x axis aligned vertically downwards, the y axis horizontal and normal to the fault and the z axis directed along the length of the fault. The thickness of the lithosphere is h and a far field boundary condition is applied at a distance L from the centre of the fault. The fault lies between the two tectonic plates and is bounded by the planes $y = \pm w$.

5.2 Assumptions and Simplifications

Owing to the timescale over which stress and strain accumulates coupled with the large stresses present in the Earth, it is assumed that the inertia of the system is negligible and the governing momentum equations, (2.17), reduce to the equilibrium equations, (2.18). Furthermore, the effect of gravity is assumed to not vary with the deformation. Taking the partial time derivative of the equilibrium

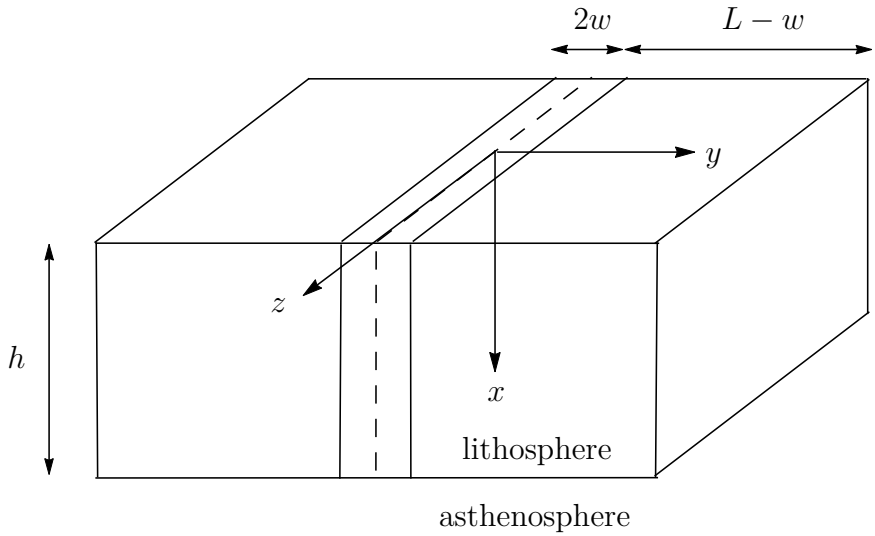

Figure 5.1: The 3D geometry of the problem. A cuboid fault region of width $2w$ is embedded between two other cuboidal regions representing the tectonic plates. The depth in the x direction of the tectonic plate and fault material is h and the two tectonic plates extended a distance L from the centre of the fault in the y direction.

equations, (2.18), gives

$$\rho\frac{\partial b_1}{\partial t}+\frac{\partial \dot{\sigma}_{11}}{\partial x}+\frac{\partial \dot{\sigma}_{12}}{\partial y}+\frac{\partial \dot{\sigma}_{13}}{\partial z}=0,$$
$$\rho\frac{\partial b_2}{\partial t}+\frac{\partial \dot{\sigma}_{12}}{\partial x}+\frac{\partial \dot{\sigma}_{22}}{\partial y}+\frac{\partial \dot{\sigma}_{23}}{\partial z}=0,$$
$$\rho\frac{\partial b_3}{\partial t}+\frac{\partial \dot{\sigma}_{13}}{\partial x}+\frac{\partial \dot{\sigma}_{23}}{\partial y}+\frac{\partial \dot{\sigma}_{23}}{\partial z}=0.$$

Here the superposed dot denotes the partial time derivative. Since the only body force is gravity, which is time independent, the equilibrium equations reduce to

$$\frac{\partial \dot{\sigma}_{11}}{\partial x}+\frac{\partial \dot{\sigma}_{12}}{\partial y}+\frac{\partial \dot{\sigma}_{13}}{\partial z}=0,$$
$$\frac{\partial \dot{\sigma}_{12}}{\partial x}+\frac{\partial \dot{\sigma}_{22}}{\partial y}+\frac{\partial \dot{\sigma}_{23}}{\partial z}=0,$$
$$\frac{\partial \dot{\sigma}_{13}}{\partial x}+\frac{\partial \dot{\sigma}_{23}}{\partial y}+\frac{\partial \dot{\sigma}_{23}}{\partial z}=0.$$

Although the gravity effects have been removed from the governing equations they still influence the state of stress, and hence also the yield, through the pre-stress resulting from the weight of the tectonic plates. A derivation of the pre-stress is given in Section 5.5.1.

The focus of this thesis is on the behaviour of the system in the vertical direction and it is assumed that there is no variation along the length of the fault in the z direction. Therefore, the domain in which the problem is solved reduces to a 2D problem in each plane defined by $z = const$. While in reality earthquake rupture does not occur simultaneously along the full length of the fault, this simplification greatly reduces the complexity of the problem as well as the computational cost. The rate-form of the equilibrium equations therefore reduces further to

$$\begin{aligned} \frac{\partial \dot{\sigma}_{11}}{\partial x} + \frac{\partial \dot{\sigma}_{12}}{\partial y} &= 0, \\ \frac{\partial \dot{\sigma}_{12}}{\partial x} + \frac{\partial \dot{\sigma}_{22}}{\partial y} &= 0, \\ \frac{\partial \dot{\sigma}_{13}}{\partial x} + \frac{\partial \dot{\sigma}_{23}}{\partial y} &= 0. \end{aligned} \tag{5.1}$$

There is evidence at the surface of strike-slip earthquake faults that there is little motion of the tectonic plates or the fault material in the vertical direction or normal to the fault. Consequently, it is assumed that the velocity components in the x and y directions are negligible compared to the velocity in the z direction, denoted by V.

It is assumed that the deformation of the region $y < 0$ is of equal magnitude and opposite sign to that occuring in the region $y > 0$. This introduces antisymmetry and the problem need only be solved in the half domain $(x, y) \in [0, h] \times [0, L]$ shown in Figure 5.2.

The fault material is assumed to have undergone a continuous deformation for thousands of years and is now in an isochoric state in which the grains are suitably packed so as to not undergo compaction or dilation when sheared.

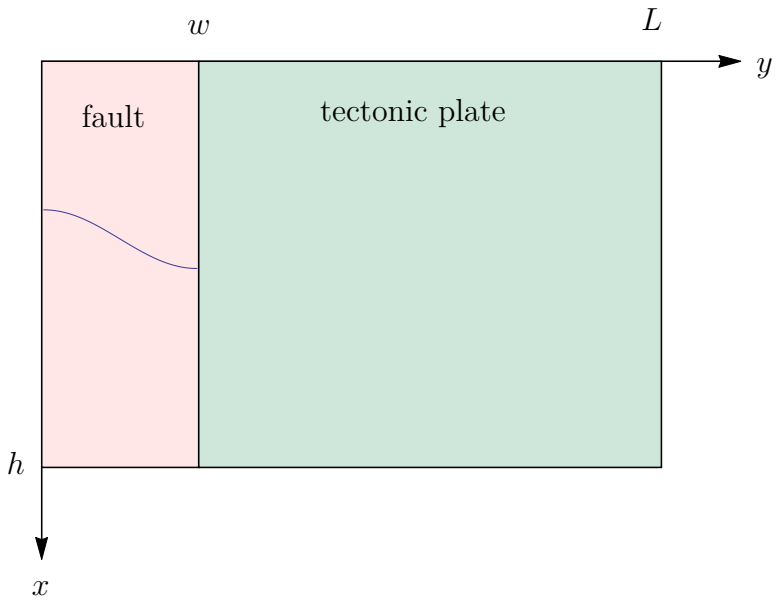

Figure 5.2: The 2D geometry of the problem. The green region represents the cross section of the tectonic plate and the red region is the fault. The elasto-plastic boundary that separates the fault material that is yield from that which has not reached yield is shown by the blue curve across the fault.

5.3 Governing Equations

The equations of motion for a system independent of z with no inertia and time independent body force can be expressed as the partial time derivative of the equilibrium equations, (5.1), which is stated again below for convenience

$$\begin{aligned} \frac{\partial \dot{\sigma}_{11}}{\partial x} + \frac{\partial \dot{\sigma}_{12}}{\partial y} &= 0, \\ \frac{\partial \dot{\sigma}_{12}}{\partial x} + \frac{\partial \dot{\sigma}_{22}}{\partial y} &= 0, \\ \frac{\partial \dot{\sigma}_{13}}{\partial x} + \frac{\partial \dot{\sigma}_{23}}{\partial y} &= 0. \end{aligned} \tag{5.2}$$

The constitutive behaviour of the tectonic plate is assumed to be isotropic, homogeneous linear elastic and as such obeys the generalised Hooke's law as outlined in Section 2.4. The partial time derivative of the generalised Hooke's law is

$$\dot{\sigma}_{ij} = \lambda \delta_{ij} d_{kk} + 2\mu d_{ij}. \tag{5.3}$$

The shear modulus is taken to be $500kbar$ in line with Rowshandel and Nemat-Nasser [1986]. Since it is assumed that there is only one non-zero velocity component, which is independent of z, there are only four non-zero components of the deformation-rate tensor, $d_{13} = d_{31}$ and $d_{23} = d_{32}$. There are, therefore, only two non-trivial constitutive equations from (5.3) which are

$$\begin{aligned} \dot{\sigma}_{13} &= \mu \frac{\partial V}{\partial x}, \\ \dot{\sigma}_{23} &= \mu \frac{\partial V}{\partial y}. \end{aligned} \tag{5.4}$$

The first two equilibrium-rate equations in (5.2) then become trivial and the third reduces to the two-dimensional Laplace's equation for the velocity $V(x, y, t)$

$$\frac{\partial^2 V}{\partial x^2} + \frac{\partial^2 V}{\partial y^2} = 0, \tag{5.5}$$

within the tectonic plate.

The material within the fault is taken to be an elasto-plastic granular medium which initially deforms as a linear elastic solid governed by (5.5) and, once equality in the yield criterion occurs, then the material undergoes work hardening plasticity. The yield criterion that determines the onset of the elasto-plastic deformation is given by

$$f(\sigma, k(\epsilon^p)) \leq 0,$$

where k is a function of the plastic strain ϵ^p which is given by

$$\epsilon^p = \int_0^t \left\{ (d^p_{13})^2 + (d^p_{23}) \right\}^{\frac{1}{2}} d\tau. \tag{5.6}$$

Here d^p_{ij} is the plastic part of the deformation-rate tensor and is assumed to obey an additive relation with the elastic part to form the total deformation-rate

$$d_{ij} = d^e_{ij} + d^p_{ij}. \tag{5.7}$$

The elastic part can be found using the time derivative of the generalised Hooke's

law, (5.3),

$$d^e_{ij} = \frac{\dot{\sigma}_{ij}}{2\mu}, \tag{5.8}$$

and the plastic part is given by the associated flow rule, (2.30), which is restated here

$$d^p_{ij} = \dot{\lambda}\frac{\partial g}{\partial \sigma_{ij}} = \dot{\lambda}\frac{\partial f}{\partial \sigma_{ij}}, \tag{5.9}$$

where g is the isochoric plastic potential equal to the yield function f. The condition that plastic deformation continues once instigated is $\dot{f} = 0$ as this maintains a stress state which lies on the yield surface given by $f = 0$. This can be used to find the expression for the parameter $\dot{\lambda}$. Taking the partial time derivative of f gives

$$\dot{f} = f_{i3}\dot{\sigma}_{i3} + \frac{\partial f}{\partial k}\frac{dk}{d\epsilon^p}\dot{\epsilon}^p.$$

The subscripts on f denote partial differentiation with respect to the corresponding component of the stress tensor. The definition of ϵ^p, (5.6), and the flow rule, (5.9), can be used to replace $\dot{\epsilon}^p$

$$\begin{aligned} \dot{f} &= f_{i3}\dot{\sigma}_{i3} + \frac{\partial f}{\partial k}\frac{dk}{d\epsilon^p}\left\{\left(d^p_{13}\right)^2 + \left(d^p_{23}\right)\right\}^{\frac{1}{2}} \\ &= f_{i3}\dot{\sigma}_{i3} + \dot{\lambda}\frac{\partial f}{\partial k}\frac{dk}{d\epsilon^p}\left(f^2_{13} + f^2_{23}\right)^{\frac{1}{2}}. \end{aligned} \tag{5.10}$$

Here we have used the fact that $\dot{\lambda} \geq 0$, as given by (2.31), to remove the $\dot{\lambda}$ from the inside square root.

This can be equated to zero and rearranged to find $\dot{\lambda}$

$$\dot{\lambda} = -\frac{f_{i3}\dot{\sigma}_{i3}}{\frac{\partial f}{\partial k}\frac{dk}{d\epsilon^p}\left(f^2_{13} + f^2_{23}\right)^{\frac{1}{2}}}. \tag{5.11}$$

The parameter, H, can then be defined as

$$H = -\frac{\partial f}{\partial k}\frac{dk}{d\epsilon^p}\left(f^2_{13} + f^2_{23}\right)^{\frac{1}{2}}. \tag{5.12}$$

Therefore, the total deformation-rate, (5.7), can be found by adding the non-zero components of the time derivative of the generalised Hooke's law, (5.8), and the flow rule, (5.9),

$$\begin{aligned} d_{13} &= \frac{\dot{\sigma}_{13}}{2\mu} + \dot{\lambda} f_{13}, \\ d_{23} &= \frac{\dot{\sigma}_{23}}{2\mu} + \dot{\lambda} f_{23}. \end{aligned}$$

The definitions of $\dot{\lambda}$ and H given by (5.11) and (5.12) are used to write

$$\begin{aligned} d_{13} &= \frac{\dot{\sigma}_{13}}{2\mu} + \frac{f_{13} f_{i3} \dot{\sigma}_{i3}}{H}, \\ d_{23} &= \frac{\dot{\sigma}_{23}}{2\mu} + \frac{f_{23} f_{i3} \dot{\sigma}_{i3}}{H}. \end{aligned}$$

Finally, these are rearranged to give the elasto-plastic constitutive behaviour of the fault material

$$d_{13} = \left(\frac{1}{2\mu} + \frac{f_{13}^2}{H} \right) \dot{\sigma}_{13} + \frac{f_{13} f_{23}}{H} \dot{\sigma}_{23}, \tag{5.13}$$

$$d_{23} = \frac{f_{13} f_{23}}{H} \dot{\sigma}_{13} + \left(\frac{1}{2\mu} + \frac{f_{23}^2}{H} \right) \dot{\sigma}_{23}. \tag{5.14}$$

These equations can be inverted to obtain expressions for the stress-rates in terms of the strain-rates. This is done by taking linear combinations of (5.13) and (5.14)

$$\begin{aligned} \left(\frac{1}{2\mu} + \frac{f_{23}^2}{H} \right) d_{13} &= \left(\frac{1}{2\mu} + \frac{f_{23}^2}{H} \right) \left(\frac{1}{2\mu} + \frac{f_{13}^2}{H} \right) \dot{\sigma}_{13} + \frac{f_{13} f_{23}}{H} \left(\frac{1}{2\mu} + \frac{f_{23}^2}{H} \right) \dot{\sigma}_{23}, \\ \frac{f_{13} f_{23}}{H} d_{23} &= \frac{f_{13}^2 f_{23}^2}{H^2} \dot{\sigma}_{13} + \frac{f_{13} f_{23}}{H} \left(\frac{1}{2\mu} + \frac{f_{23}^2}{H} \right) \dot{\sigma}_{23}. \end{aligned}$$

Subtracting the second from the first and rearranging gives

$$\dot{\sigma}_{13} = \frac{1}{\det \Sigma} \left(\frac{1}{2\mu} + \frac{f_{23}^2}{H} \right) d_{13} - \frac{1}{\det \Sigma} \frac{f_{13} f_{23}}{H} d_{23}, \tag{5.15}$$

where

$$\det \Sigma = \left(\frac{1}{2\mu} + \frac{f_{13}^2}{H}\right)\left(\frac{1}{2\mu} + \frac{f_{23}^2}{H}\right) - \frac{f_{13}^2 f_{23}^2}{H^2}.$$

Similarly,

$$\dot{\sigma}_{23} = -\frac{1}{\det \Sigma}\frac{f_{13}f_{23}}{H}d_{13} + \frac{1}{\det \Sigma}\left(\frac{1}{2\mu} + \frac{f_{13}^2}{H}\right)d_{23}. \tag{5.16}$$

The constitutive equations in either the form given by (5.13) and (5.14) or (5.15) and (5.16) are augmented by the rate form of the equilibrium equations,

$$\frac{\partial \dot{\sigma}_{13}}{\partial x} + \frac{\partial \dot{\sigma}_{23}}{\partial y} = 0,$$

to provide the governing equations in the elasto-plastic phase of the fault material.

5.4 Boundary Conditions

The traction on the surface of the Earth is that due to air pressure which is taken to be constant throughout the deformation and contributes only to the pre-stress. The traction-rate applied during the subsequent deformation is then zero. This translates into the boundary condition

$$\dot{\sigma}_{13}(0, y, t) = 0.$$

The relations (5.4) from the generalised Hooke's law give

$$\left.\frac{\partial V}{\partial x}\right|_{x=0} = 0, \tag{5.17}$$

at the top of the tectonic plate and the pre-yield fault. When the top of the fault reaches yield relations (5.15) can be used to express the boundary condition as

$$\frac{1}{\det \Sigma}\left(\frac{1}{2\mu} + \frac{f_{23}^2}{H}\right)\left.\frac{\partial V}{\partial x}\right|_{x=0} - \frac{1}{\det \Sigma}\frac{f_{13}f_{23}}{H}\left.\frac{\partial V}{\partial y}\right|_{x=0} = 0. \tag{5.18}$$

The far field boundary condition is intended to restrict the effects of the fault to near $y = 0$ so that beyond $y = L$ the tectonic plate moves as a rigid body. We apply a shear strain-rate of $2 \times 10^{-5} rad/yr$, as reported by Thatcher [1983] as a measured surface strain-rate. The corresponding far field velocity at this point is denoted $\frac{v_0}{2}$ and takes the value $0.05myr^{-1}$. In the absence of data regarding the depth dependence of the strain-rate the surface measurement is assumed to hold at all depths. We apply a constant strain-rate at $y = L$ which, for generality, is denoted γ. The boundary condition is

$$\dot{\sigma}_{23}(x, L, t) = \mu\gamma,$$

or alternatively

$$\left.\frac{\partial V}{\partial y}\right|_{y=L} = \gamma. \tag{5.19}$$

The lower surface of the domain is under the influence of the asthenosphere driving force. This interaction is taken to be an applied traction rate

$$\dot{\sigma}_{13}(h, y, t) = \mu\mathcal{G}(y, t), \tag{5.20}$$

where $\mathcal{G}$ is to be defined. This can be written as

$$\left.\frac{\partial V}{\partial x}\right|_{x=h} = \mathcal{G}(y, t), \tag{5.21}$$

on the tectonic plate and the pre-yield fault. When the base of the fault reaches yield the boundary condition is

$$\frac{1}{2\det\Sigma}\left(\frac{1}{\mu} + \frac{f_{23}^2}{H}\right)\left.\frac{\partial V}{\partial x}\right|_{x=h} - \frac{1}{2\det\Sigma}\frac{f_{13}f_{23}}{H}\left.\frac{\partial V}{\partial y}\right|_{x=h} = \mu\mathcal{G}(y, t). \tag{5.22}$$

The antisymmetry of the problem requires that for a continuous velocity field the velocity at the centre of the fault must be zero, thus

$$V(x, 0, t) = 0. \tag{5.23}$$

Across the boundary between the fault and the tectonic plate it is required that the traction-rate is continuous in order to maintain quasi-static equilibrium. Due to the edge of the fault being parallel to the x axis, this takes the form

$$\lim_{y \to w^-} \dot{\sigma}_{23}(x, y, t) = \lim_{y \to w^+} \dot{\sigma}_{23}(x, y, t). \tag{5.24}$$

During the elastic phase of the fault material, generalised Hooke's law gives

$$\left.\frac{\partial V}{\partial y}\right|_{y=w^+} = \left.\frac{\partial V}{\partial y}\right|_{y=w^-}. \tag{5.25}$$

The relation (5.16) is used to write this boundary condition as

$$\mu \left.\frac{\partial V}{\partial y}\right|_{y=w^+} = -\frac{1}{\det \Sigma} \frac{f_{13} f_{23}}{H} \left.\frac{\partial V}{\partial x}\right|_{y=w^-} + \frac{1}{\det \Sigma} \left(\frac{1}{2\mu} + \frac{f_{13}^2}{H}\right) \left.\frac{\partial V}{\partial y}\right|_{y=w^-}, \tag{5.26}$$

during the plastic phase of the fault material.

It is also assumed that there is sufficient friction between the tectonic plate and the fault material to prevent slipping so that the velocity is continuous

$$\lim_{y \to w^-} V(x, y, t) = \lim_{y \to w^+} V(x, y, t). \tag{5.27}$$

The elasto-plastic boundary separates two different material responses of one medium. The boundary conditions across it are chosen to be continuity of velocity, which ensures the material remains intact, and also continuity of normal traction-rate. This latter condition maintains quasi-static equilibrium and conserves the initial continuous stress field, as Prescott and Nur [1981] shows is necessary.

5.5 Initial Conditions

In addition to boundary conditions applied to the edge of the domain at each time step we additionally require intial conditions to allow the time stepping and accumulation of the stresses and strains. These take the form of intial velocities, stress-rates and stresses. The latter is given by the lithostatic pressure and is outlined in the next section. Simple expressions for the velocities in the asthenosphere

are given in Sections 5.5.2. This is then used to define a boundary value problem for the initial velocity in the lithosphere.

5.5.1 Lithostatic Presure and Pre-Stress

The stress field that is present in the Earth as a result of its own weight is called the *overburden pressure* or *lithostatic pressure* and is given by

$$p(x) = p_0 + g_a \int_0^x \rho(x)dx. \tag{5.28}$$

The acceleration due to gravity, g_a, is taken to be a constant, the density of the rock is $\rho(x)$ and the air pressure at the Earth's surface is p_0. The value of p_0 is taken to be $1bar$, the pressure at sea level. The stress tensor of such a stress state is

$$\sigma = \begin{pmatrix} -p & 0 & 0 \\ 0 & -p & 0 \\ 0 & 0 & -p \end{pmatrix}, \tag{5.29}$$

and acts as an initial condition for the stress state at later times. Since this pre-stress is independent of time the stress tensor at time t can be expressed as

$$\sigma_{ij}(x, y, z, t) = -p(x)\delta_{ij} + \int_0^t \dot{\sigma}_{ij}(x, y, z, \tau)d\tau. \tag{5.30}$$

5.5.2 Velocity in the Asthenosphere

The elevated temperatures and thermal stresses present in the Earth's mantle cause the rock to flow through viscous creep. Due to the inaccessible location of the material its precise rheology is unknown but it is most commonly assumed that the constitutive equations relate the strain-rate to the stresses through a power law of the form

$$\dot{\epsilon}_{ij} = C_a \sigma_{ij}^n e^{\frac{E}{\kappa T}}, \tag{5.31}$$

where C_a and n are material parameters, E is the activation energy, T is the absolute temperature and κ is the Boltzmann's constant. The value of n hypothesised in the literature typically ranges from 2 to 8, Heard [1976] and Elsasser [1969], but we follow Rowshandel and Nemat-Nasser [1986] and take $n = 1$ for simplicity.

We adapt the model of Melosh [1977] to calculate the stress within the asthenosphere. The asthenosphere is taken to be of thickness d in the x direction. Its constitutive behaviour is assumed to follow the power law given by (5.31) with $n = 1$ and is in equilibrium. The effect of gravity on the velocity in the asthenosphere is beyond this thesis and is neglected. We further neglect the x and y components of velocity in order to match that of the lithosphere. Substitution of (5.31) into the equilibrium equations (2.18) yields Laplace's equation for the non-zero velocity V_a

$$\frac{\partial^2 V_a}{\partial x^2} + \frac{\partial^2 V_a}{\partial y^2} = 0.$$

The top surface of the asthenosphere is assumed to be stress free initially and the lower surface at $x = h + d$, has an applied stress, $\sigma_{13} = \sigma_b$. On $y = L$ the strain-rate is taken to be γ and the velocity at $(h, 0)$ is zero to match the tectonic plate above. By adopting the stress field in Melosh [1977], which varies linearly with depth, we write the velocity as

$$V_a = -\frac{\sigma_b}{2\eta_a d}x(2h - x) + \frac{\sigma_b}{2\eta_a d}y(2L - y) + \gamma y + \frac{h^2\sigma_b}{2\eta_a d},$$

where $\eta_a = C_a e^{\frac{E}{\kappa T}}$. The velocity along the base of the tectonic plate is chosen to match the velocity at the top of the asthenosphere and is therefore

$$V_b(y) = V_a(h, y) = \frac{\sigma_b}{2\eta_a d}y(2L - y) + \gamma y. \tag{5.32}$$

The values assigned to the parameters η_a, d and σ_b are taken from Melosh [1977] and are $\eta_a = 5e^{19}$Poise, $d = 100km$ and $\sigma_b = 3.5bar$. The initial velocity within the lithosphere is given by the solution to Laplace's equation with the same boundary conditions on the boundaries defined by $x = 0$ and $y = 0, L$ given by (5.17), (5.19) and (5.23). On $x = h$ we apply continuity of velocity with the asthenosphere and

as such the velocity is (5.32). The velocity can then be differentiated to give the stress-rate on the lower surface of the tectonic plate and fault.

5.6 The Yield Criterion

In Chapter 2 the Mohr-Coulomb, Tresca and von Mises yield criterions were stated in a general three dimensional geometry. We study now the effects of the geometry of the current problem on these three yield criterions.

The Mohr-Coulomb yield criterion is stated in terms of the principal stresses. For the current problem the stress tensor, given by (5.30), reduces to

$$\sigma = \begin{pmatrix} -p & 0 & \sigma_{13} \\ 0 & -p & \sigma_{23} \\ \sigma_{13} & \sigma_{23} & -p \end{pmatrix}.$$

The principal stresses are found by finding the roots of the characteristic polynomial

$$(p+\lambda)\left[(p+\lambda)^2 - \sigma_{13}^2 - \sigma_{23}^2\right] = 0.$$

Denote $q = \sqrt{\sigma_{13}^2 + \sigma_{23}^2}$ so that the principal stresses can be written $\sigma_I = -p + q$, $\sigma_{II} = p$ and $\sigma_{III} = -p - q$. The linear combinations of the principal stresses that appear in the Mohr-Coulomb yield criterion in the form (2.24) are related to p and q through

$$\begin{aligned} p &= -\frac{\sigma_I + \sigma_{III}}{2}, \\ q &= \frac{\sigma_I - \sigma_{III}}{2}. \end{aligned}$$

The yield criterion (2.24) can then be expressed as

$$q - p\sin\phi - c\cos\phi \leq 0.$$

Since p is a constant with respect to time this could equally be expressed as

$$q \leq p \sin\phi + c\cos\phi,$$

where the right hand side is independent of time. In this form the Mohr-Coulomb yield criterion is equivalent to the Tresca yield criterion, given by (2.28), with $\sigma_c = 2p\sin\phi + 2c\cos\phi$.

The deviatoric stress tensor for the current problem is

$$s = \begin{pmatrix} 0 & 0 & \sigma_{13} \\ 0 & 0 & \sigma_{23} \\ \sigma_{13} & \sigma_{23} & 0 \end{pmatrix},$$

and its second invariant, given by (2.8), is $J_2 = q^2$. Setting $k = p\sin\phi + c\cos\phi$ in the von Mises yield criterion therefore gives the same expression as both the Mohr-Coulomb and the Tresca yield criterions for the current problem. The yield criterion for the current problem is taken to be

$$f = q - k \leq 0, \tag{5.33}$$

where $q = \sqrt{\sigma_{13}^2 + \sigma_{23}^2}$ and $k = p\sin\phi + c\cos\phi$.

We now define the work hardening parameter k. The work by Rowshandel and Nemat-Nasser [1987] defines several material parameters that are important in the constitutive response of fault gouge which depend on temperature and pressure and this incorporates depth dependence into the yield criterion. They use experimental data from Rummel et al. [1978] and Caristan [1982] to derive the following material parameters for granite

$$\begin{aligned} \frac{\partial k}{\partial p} &= (1.05 - 9\times 10^{-7}\hat{T}^2)(0.81 + 0.6e^{-1.8\hat{p}}), \\ \hat{\alpha} &= 1.04e^{-0.002\hat{T}}(775 - 500e^{-3\hat{p}}), \\ \hat{\rho} &= (0.21 + 0.42e^{-0.0027\hat{T}})(40 + 120e^{-4\hat{p}}), \end{aligned}$$

where $\hat{p}$ is the numerical value of p in $kbar$ and $\hat{T}$ is the temperature in $^\circ C$. The first expression gives the pressure dependence of the yield criterion and measures

the internal friction. The latter two are combined to give the work hardening behaviour of the yield criterion

$$\frac{\partial k}{\partial \epsilon^p} = \hat{\alpha} e^{-\hat{\rho}}.$$

We define the work hardening parameter k as

$$k = p\frac{\partial k}{\partial p} + \epsilon^p \hat{\alpha} e^{-\hat{\rho}} + c, \tag{5.34}$$

where c is the cohesion. Depth dependence of the cohesion is not given by Rowshandel and Nemat-Nasser [1987] but they use a value of the order of $0.2kbar$ and so we set its value to be equal to $\frac{\partial k}{\partial p}$ in $kbar$. The density of granite is in the range $2.7 - 2.8 \times 10^3 kgm^{-3}$ and the density that appears in the definition of p is assigned the constant value $2.7 \times 10^3 kgm^{-3}$. The value of the acceleration due to gravity is $g_a = 9.81ms^{-2}$ and the pressure at the Earth's surface is taken to be the pressure at sea level which is $1bar$. The temperature within the lithosphere takes the value $20°C$ at the Earth's surface and increases with constant gradient of $20°Ckm^{-1}$.

5.6.1 Ellipticity of the Elasto-plastic Governing Equations

In Chapter 4, the significance of a PDE's type was expressed. This section provides a classification of the system of equations given by the third equation in (5.2), (5.13) and (5.14) using the symbol notation described in Chapter 4. The system of equations can be written in matrix form using the labellings $i\xi_1 = \frac{\partial}{\partial x}$ and $i\xi_2 = \frac{\partial}{\partial y}$ as

$$\begin{pmatrix} \mu i\xi_1 & -\left(1 + \frac{\mu}{H} f_{13}^2\right) & -\frac{\mu}{H} f_{13} f_{23} \\ \mu i\xi_2 & -\frac{\mu}{H} f_{13} f_{23} & -\left(1 + \frac{\mu}{H} f_{23}^2\right) \\ 0 & i\xi_1 & i\xi_2 \end{pmatrix} \begin{pmatrix} V \\ \dot{\sigma}_{13} \\ \dot{\sigma}_{23} \end{pmatrix} = 0.$$

Taking the determinant of the coefficient matrix gives

$$i\xi_1 \mu \left[i\xi_1 \left(1 + \frac{\mu}{H} f_{23}^2\right) - i\xi_2 \frac{\mu}{H} f_{13} f_{23} \right] - \mu i\xi_2 \left[i\xi_1 \frac{\mu}{H} f_{13} f_{23} - i\xi_2 \left(1 + \frac{\mu}{H} f_{13}^2\right) \right] = 0.$$

Dividing through by $i^2\xi_2^2\mu$ and replacing $\frac{dy}{dx} = -\frac{\xi_1}{\xi_2}$ gives

$$\left(\frac{dy}{dx}\right)^2 \left(1 + \frac{\mu}{H} f_{23}^2\right) + \frac{2\mu}{H} f_{13} f_{23} \frac{dy}{dx} + \left(1 + \frac{\mu}{H} f_{13}^2\right) = 0. \tag{5.35}$$

The discriminant of this quadratic is

$$\begin{aligned} &4\frac{\mu^2}{H^2} f_{13}^2 f_{23}^2 - 4\left(1 + \frac{\mu}{H} f_{13}^2\right)\left(1 + \frac{\mu}{H} f_{23}^2\right) \\ &\quad = 4\frac{\mu^2}{H^2} f_{13}^2 f_{23}^2 - 4\left(1 + \frac{\mu}{H} f_{13}^2 + \frac{\mu}{H} f_{23}^2 + \frac{\mu^2}{H^2} f_{13}^2 f_{23}^2\right) \\ &\quad = -4\left(1 + \frac{\mu}{H}\left(f_{13}^2 + f_{23}^2\right)\right). \end{aligned} \tag{5.36}$$

The term $f_{13}^2 + f_{23}^2$ is strictly positive, as is μ. Although H contains a negative sign, (5.12), this is cancelled out by $\frac{\partial f}{\partial k}$ which is negative from (5.33). Furthermore, $\frac{dk}{d\epsilon^p}$ is assumed positive since we are applying isotropic hardening in which the yield surface expands. Consequently H is always positive. The right hand side of (5.36) is therefore always negative and the system is elliptic.

Since the system of equations given by the third equation in (5.2), (5.13) and (5.14) are elliptic a numerical method, such as the finite difference method, is applied. The three first order equations are combined into one second order equation for the velocity component V. Substitution of the constitutive equations (5.13) and (5.14) into the rate-form of the equilibrium equations (5.2) gives

$$\Sigma_1 \frac{\partial^2 V}{\partial x^2} + \Sigma_3 \frac{\partial^2 V}{\partial y^2} - 2\Sigma_2 \frac{\partial^2 V}{\partial x \partial y} + M_1 \frac{\partial V}{\partial x} + M_2 \frac{\partial V}{\partial y} = 0. \tag{5.37}$$

where

$$
\begin{aligned}
M_1 &= \frac{1}{\mu}\frac{\partial}{\partial x}\left\{\frac{1}{\det\Sigma}\left(\frac{1}{2\mu}+\frac{f_{23}^2}{H}\right)\right\}-\frac{1}{\mu}\frac{\partial}{\partial y}\left\{\frac{1}{\det\Sigma}\frac{f_{13}f_{23}}{H}\right\},\\
M_2 &= -\frac{1}{\mu}\frac{\partial}{\partial x}\left\{\frac{1}{\det\Sigma}\frac{f_{13}f_{23}}{H}\right\}+\frac{1}{\mu}\frac{\partial}{\partial y}\left\{\frac{1}{\det\Sigma}\left(\frac{1}{2\mu}+\frac{f_{13}^2}{H}\right)\right\},\\
\Sigma_1 &= \frac{1}{\mu\det\Sigma}\left(\frac{1}{2\mu}+\frac{f_{23}^2}{H}\right),\\
\Sigma_2 &= \frac{1}{\mu\det\Sigma}\frac{f_{13}f_{23}}{H},\\
\Sigma_3 &= \frac{1}{\mu\det\Sigma}\left(\frac{1}{2\mu}+\frac{f_{13}^2}{H}\right).
\end{aligned}
$$

Here we have divided through by the shear modulus, μ, so that the coefficients are of order $O(1)$ to match Laplace's equation and facilitate the numerical calculations.

Chapter 6

Analytical Solution to Elastic Phase of the Fault Material

Prior to any of the fault material reaching yield the governing equation in both the tectonic plate and the fault is Laplace's equation for the respective velocities V^t and V^f. This can be solved analytically using separation of variables and this work is presented in this chapter. The velocity and traction-rate boundary conditions across the edge of the fault are replaced by Fourier series expansions of two arbitrary functions $\mathcal{F}(x)$ and $F(x)$. On the boundary of the tectonic plate at $y = w$ the velocity is set to $\mathcal{F}(x)$ and at the edge of the fault the non-zero component of traction-rate is equated to $F(x)$. The solutions for V^t and V^f are found in terms of the Fourier coefficients of the $\mathcal{F}(x)$ and $F(x)$ respectively. These Fourier coefficients are then evaluated by applying the continuity of velocity and traction-rate boundary conditions which is done by replacing $\mathcal{F}(x)$ and $F(x)$ by their alternate definitions in terms of V^f and V^t. The far field strain-rate is taken to be zero for simplicity.

The analytical solution is used in Chapter 8 to check the accuracy of the numerical solution and the rate of convergence of the novel finite difference scheme devised in the vicinity of the curved boundary.

6.1 The Elastic Plate

The solution to Laplace's equation in the tectonic plate defined by $(x, y) \in [0, h] \times [w, L]$ subject to the boundary conditons,

$$\begin{aligned}
\left.\frac{\partial V^t}{\partial x}\right|_{x=0} &= 0, \\
\left.\frac{\partial V^t}{\partial x}\right|_{x=h} &= \mathcal{G}(y), \\
\left.\frac{\partial V^t}{\partial y}\right|_{y=L} &= 0, \\
V(x, w) &= \mathcal{F}(x),
\end{aligned}$$

is obtained by superposition of two solutions.

Case A: consists of the boundary conditions

$$\begin{aligned}
\left.\frac{\partial V^t}{\partial x}\right|_{x=0} &= 0, \\
\left.\frac{\partial V^t}{\partial x}\right|_{x=h} &= \mathcal{G}(y), \\
\left.\frac{\partial V^t}{\partial y}\right|_{y=L} &= 0, \\
V^t(x, w) &= 0.
\end{aligned}$$

Case B: comprises the boundary conditions

$$\begin{aligned}
\left.\frac{\partial V^t}{\partial x}\right|_{x=0} &= 0, \\
\left.\frac{\partial V^t}{\partial x}\right|_{x=h} &= 0, \\
\left.\frac{\partial V^t}{\partial y}\right|_{y=L} &= 0, \\
V^t(x, w) &= \mathcal{F}(x).
\end{aligned}$$

Laplace's Equation can be solved by separation of variables by assuming the velocity can be expressed as $V(x,y) = X(x)Y(y)$ to obtain

$$\frac{X''}{X} = -\frac{Y''}{Y} = \mu^2. \tag{6.1}$$

It can be shown that only $\mu^2 > 0$ leads to a non-trivial solution for case A and then the solutions for X and Y are

$$\begin{aligned} X(x) &= A\cosh\mu x + B\sinh\mu x, \\ Y(y) &= a\cos\mu y + b\sin\mu y. \end{aligned}$$

The boundary condition at $y = w$ requires $Y(w) = 0$ and, for a suitably defined $\hat{a}$, implies $Y = \hat{a}\sin\mu(y-w)$. Consequently, the boundary condition at $y = L$ requires $Y'(L) = \hat{a}\mu\cos\mu(y-w) = 0$ and, for non-trivial solutions, eigenvalues are defined as

$$\mu_m = \frac{(2m-1)\pi}{2(L-w)}, \qquad \text{for } m = 1, 2, ...$$

Finally, the condition at $x = 0$ implies $B = 0$ and this gives the eigenfunctions

$$V_m^t(x,y) = a_m \sin\mu_m(y-w)\cosh\mu_m x. \tag{6.2}$$

The values of the a_m are related to the Fourier coefficients of $\mathcal{G}(y)$ but relations shall be derived at the end of the section once the full solution is constructed.

For a non-trivial solution to case B it is required that $\mu^2 < 0$ so we define $\lambda^2 = -\mu^2$. The solutions to equations (6.1) are

$$\begin{aligned} X(x) &= A\cos\lambda x + B\sin\lambda x, \\ Y(y) &= a\cosh\lambda y + b\sinh\lambda y. \end{aligned}$$

Now the boundary conditon at $x = 0$ implies $b = 0$ and the condition at $x = h$ then requires the eigenvalues to be

$$\lambda_n = \frac{n\pi}{h}, \qquad \text{for } n = 1, 2, ...$$

The condition at $y = L$ gives the solutions $Y_n = \hat{A} \cosh \lambda_n (L - y)$. For this case the eigenmodes are

$$V_n^t(x, y) = b_n \cosh \lambda_n (L - y) \cos \lambda_n x. \tag{6.3}$$

In addition, there is a non-trivial solution when $\mu = 0$ that is

$$V_0^t(x, y) = \mathcal{F}_0. \tag{6.4}$$

The full solution is the sum of the three solutions (6.2), (6.3) and (6.4) with sums over m and n. Thus

$$V^t(x, y) = \mathcal{F}_0 + \sum_{m=1}^{\infty} a_m \sin \mu_m (y - w) \cosh \mu_m x + \sum_{n=1}^{\infty} b_n \cosh \lambda_n (L - y) \cos \lambda_n x. \tag{6.5}$$

The final two boundary conditions are used to evaluate the a_m and the b_n. These give

$$\left. \frac{\partial V^t}{\partial x} \right|_{x=h} = \sum_{m=1}^{\infty} a_m \mu_m \sin \mu_m (y - w) \sinh \mu_m h = \mathcal{G}(y), \tag{6.6}$$

$$V^t(x, w) = \mathcal{F}_0 + \sum_{n=1}^{\infty} b_n \cosh \lambda_n (L - w) \cos \lambda_n x = \mathcal{F}(x). \tag{6.7}$$

Equations (6.6) and (6.7) represent Fourier expansions for the functions $\mathcal{G}(y)$ and $\mathcal{F}(x)$. The a_m and b_n can therefore be isolated by multiplying by $\sin \mu_k (y - w)$ and $\cos \lambda_k (L - y)$ repectively and integrating. Thus

$$\sum_{m=1}^{\infty} a_m \mu_m \sinh \mu_m h \int_w^L \sin \mu_m (y - w) \sin \mu_k (y - w) dy = \int_w^L \mathcal{G}(y) \sin \mu_k (y - w) dy.$$

Using orthogonality of the sin terms reduces this to

$$a_k \mu_k \frac{L - w}{2} \sinh \mu_k h = \int_w^L \mathcal{G}(y) \sin \mu_k (y - w) dy,$$

which can be rearranged to give

$$a_k = \frac{4}{(2k-1)\pi \sinh \mu_k h} \int_w^L \mathcal{G}(y) \sin \mu_k (y-w) dy.$$

Similarly for (6.7)

$$\mathcal{F}_0 = \frac{1}{h} \int_0^h \mathcal{F}(x) dx, \tag{6.8}$$

$$b_k = \frac{2}{h \cosh \lambda_k (L-w)} \int_0^h \mathcal{F}(x) \cos \lambda_k x dx. \tag{6.9}$$

6.2 Elastic Fault Material

We now solve Laplace's equation in the fault region defined by $(x, y) \in [0, h] \times [0, w]$ subject to the following boundary conditons,

$$\left.\frac{\partial V^f}{\partial x}\right|_{x=0} = 0,$$
$$\left.\frac{\partial V^f}{\partial x}\right|_{x=h} = \mathcal{G}(y),$$
$$\left.\frac{\partial V^f}{\partial y}\right|_{y=w} = F(x),$$
$$V^f(x, 0) = 0,$$

Again, the full solution shall be obtained by superposition of two solutions.

Case A: has the following boundary conditions

$$\left.\frac{\partial V^f}{\partial x}\right|_{x=0} = 0,$$
$$\left.\frac{\partial V^f}{\partial x}\right|_{x=h} = \mathcal{G}(y),$$
$$\left.\frac{\partial V^f}{\partial y}\right|_{y=w} = 0,$$
$$V^f(x, 0) = 0.$$

Case B: involves the boundary conditions

$$\begin{aligned}
\left.\frac{\partial V^f}{\partial x}\right|_{x=0} &= 0, \\
\left.\frac{\partial V^f}{\partial x}\right|_{x=h} &= 0, \\
\left.\frac{\partial V^f}{\partial y}\right|_{y=w} &= F(x), \\
V^f(x,0) &= 0.
\end{aligned}$$

Again applying separation of variables to Laplace's equation yields

$$\frac{X''}{X} = -\frac{Y''}{Y} = \eta^2.$$

For case A the non-trivial solution occurs only when $\eta^2 > 0$. The solution for Y is

$$Y(y) = a\cos\eta y + b\sin\eta y.$$

The boundary condition at $y = 0$ gives $a = 0$ and the condition at $y = w$ gives the eigenvalues

$$\eta_m = \frac{(2m-1)\pi}{2w}, \qquad \text{for } m = 1, 2, ...$$

Finally the solution for X is

$$X = A\cosh\eta_m x + B\sinh\eta_m x,$$

and the boundary condition at $x = 0$ gives $B = 0$. Therefore, the eigenfunctions for case A are

$$V_m^f(x,y) = \alpha_m \cosh\eta_m x \sin\eta_m y. \tag{6.10}$$

For case B) we set $\eta^2 = -\lambda^2$ for non-trivial solutions and so

$$\begin{aligned} X &= A\cos\lambda x + B\sin\lambda x, \\ Y &= a\cosh\lambda_n y + b\sinh\lambda_n y. \end{aligned}$$

The condition at $x = 0$ gives $B = 0$ and the boundary condition at $x = h$ requires the eigenvalues

$$\lambda_n = \frac{n\pi}{h}, \qquad \text{for } n = 1, 2, ...$$

Setting the value of V to be zero on $y = 0$ gives $a = 0$ and so eigenfunctions are

$$V_n^f(x, y) = \beta_n \sinh\lambda_n y \cos\lambda_n x.$$

There is also a non-trivial solution when $\eta = 0$. In this case

$$V_0^f = F_0 y.$$

The full solution in the elastic fault is

$$V^f(x, y) = F_0 y + \sum_{m=1}^{\infty} \alpha_m \cosh\eta_m x \sin\eta_m y + \sum_{n=1}^{\infty} \beta_n \sinh\lambda_n y \cos\lambda_n x. \qquad (6.11)$$

The coefficients F_0, α_m and β_n are related to the Fourier Coefficients of $\mathcal{G}(y)$ and $F(x)$. The boundary conditions at $x = h$ and $y = w$ become

$$\left.\frac{\partial V^f}{\partial x}\right|_{x=h} = \sum_{m=1}^{\infty} \alpha_m \eta_m \sinh\eta_m h \sin\eta_m y = \mathcal{G}(y), \qquad (6.12)$$

$$\left.\frac{\partial V^f}{\partial y}\right|_{y=w} = F_0 + \sum_{n=1}^{\infty} \beta_n \lambda_n \cosh\lambda_n w \cos\lambda_n x = F(x). \qquad (6.13)$$

Then, analogous to the previous section, the coefficients are given by

$$\alpha_k = \frac{4}{(2k-1)\pi \sinh\eta_k h} \int_0^w \mathcal{G}(y) \sin\eta_k y dy,$$

and

$$F_0 = \frac{1}{h}\int_0^h F(x)dx, \tag{6.14}$$

$$\beta_k = \frac{2}{k\pi \cosh \lambda_k w}\int_0^h F(x)\cos\lambda_k x dx. \tag{6.15}$$

6.3 Equating Solutions

The previous two sections solve Laplace's Equation for arbitrary boundary conditions at $y = w$. In order to couple the two solutions and evaluate the Fourier coefficients of $\mathcal{F}(x)$ and $F(x)$ it is necessary to equate the two solutions at the interface $y = w$ of their domains of validity using the continuity of velocity and traction-rate boundary conditions that are applied on $y = w$. Using the solution (6.5) the function $F(x)$ can be writen as

$$\begin{aligned} F(x) &= \left.\frac{\partial V^t}{\partial y}\right|_{y=w} \\ &= \sum_{m=1}^{\infty} a_m \mu_m \cosh \mu_m x - \mu_r \sum_{n=1}^{\infty} b_n \lambda_n \sinh \lambda_n (L-w)\cos\lambda_n x. \end{aligned}$$

Substituting into (6.14) gives

$$F_0 = \frac{1}{h}\sum_{m=1}^{\infty} a_m \sinh \mu_m h, \tag{6.16}$$

and (6.15) yields

$$\begin{aligned}
\beta_k &= \frac{2}{k\pi \cosh \lambda_k w} \left\{ \sum_{m=1}^{\infty} a_m \mu_m \int_0^h \cosh \mu_m x \cos \lambda_k x dx \right. \\
&\quad \left. - \sum_{n=1}^{\infty} b_n \lambda_n \sinh \lambda_n (L-w) \int_0^h \cos \lambda_n x \cos \lambda_k x dx \right\} \\
&= \frac{2}{k\pi \cosh \lambda_k w} \left\{ \sum_{m=1}^{\infty} \frac{a_m \mu_m}{\mu_m^2 + \lambda_k^2} [\mu_m \sinh \mu_m x \cos \lambda_k x \right. \\
&\quad \left. + \lambda_k \cosh \mu_m x \sin \lambda_k x]_{x=0}^h - b_k \frac{k\pi}{2} \sinh \lambda_n (L-w) \right\} \\
&= \frac{2}{k\pi \cosh \lambda_k w} \left\{ \sum_{m=1}^{\infty} \frac{a_m \mu_m^2}{\mu_m^2 + \lambda_k^2} (-1)^k \sinh \mu_m h - b_k \frac{k\pi}{2} \sinh \lambda_k (L-w) \right\}.
\end{aligned} \tag{6.17}$$

The expression for $\mathcal{F}(x)$, derived using (6.11), is

$$\mathcal{F}(x) = V^f(x,w) = F_0 w + \sum_{m=1}^{\infty} \alpha_m \cosh \eta_m x \sin \eta_m w + \sum_{n=1}^{\infty} \beta_n \sinh \lambda_n w \cos \lambda_n x.$$

Using the definition of η_m the identity $\sin \eta_m w = (-1)^{m+1}$ reduces this to

$$\mathcal{F}(x) = V^f(x,w) = F_0 w + \sum_{m=1}^{\infty} \alpha_m (-1)^{m+1} \cosh \eta_m x + \sum_{n=1}^{\infty} \beta_n \sinh \lambda_n w \cos \lambda_n x.$$

Substitution into (6.8) yields

$$\mathcal{F}_0 = F_0 w + \frac{1}{h} \sum_{m=1}^{\infty} \frac{\alpha_m}{\eta_m} (-1)^{m+1} \sinh \eta_m h. \tag{6.18}$$

Similarly, equation (6.9) gives

$$\begin{aligned} b_k &= \frac{2}{h\cosh\lambda_k(L-w)}\left\{\sum_{m=1}^{\infty}\alpha_m(-1)^{m+1}\int_0^h \cosh\eta_m x\cos\lambda_k x dx + \beta_k\frac{h}{2}\sinh\lambda_k w\right\} \\ &= \frac{2}{h\cosh\lambda_k(L-w)}\left\{\sum_{m=1}^{\infty}\frac{\alpha_m(-1)^{m+1}}{\eta_m^2+\lambda_k^2}\left[\eta_m\sinh\eta_m x\cos\lambda_k x\right.\right. \\ &\quad \left.\left.+\lambda_k\cosh\eta_m x\sin\lambda_k x\right]_{x=0}^{h} + \beta_k\frac{h}{2}\sinh\lambda_k w\right\} \\ &= \frac{2}{h\cosh\lambda_k(L-w)}\left\{\sum_{m=1}^{\infty}\frac{\alpha_m\eta_m}{\eta_m^2+\lambda_k^2}(-1)^{k+m+1}\sinh\eta_m h + \beta_k\frac{h}{2}\sinh\lambda_k w\right\}. \end{aligned} \tag{6.19}$$

Equations (6.16), (6.17), (6.18) and (6.19) represent a set of pairs of simultaneous equations for b_k and β_k which can be solved for each value of k. Equations (6.16) and (6.18) can be used to find

$$\mathcal{F}_0 = \frac{w}{h}\sum_{m=1}^{\infty}a_m\sinh\mu_m h + \frac{1}{h}\sum_{m=1}^{\infty}\frac{\alpha_m}{\eta_m}(-1)^{m+1}\sinh\eta_m h.$$

To simplify the algebra, introduce the notation

$$\begin{aligned} \Sigma_\mu^k &= \sum_{m=1}^{\infty}\frac{a_m\mu_m^2}{\mu_m^2+\lambda_k^2}(-1)^k\sinh\mu_m h, \\ \Sigma_\eta^k &= \sum_{m=1}^{\infty}\frac{\alpha_m\eta_m}{\eta_m^2+\lambda_k^2}(-1)^{k+m+1}\sinh\eta_m h, \end{aligned}$$

which can be simplified further by defining

$$\begin{aligned} \tilde{a}_k &= a_k\sinh\mu_k h = \frac{4}{(2k-1)\pi}\int_w^L \mathcal{G}(y)\sin\mu_k(y-w)dy, \\ \tilde{\alpha}_k &= \alpha_k\sinh\eta_k h = \frac{4}{(2k-1)\pi}\int_0^w G(y)\sin\eta_k y dy, \end{aligned} \tag{6.20}$$

so that

$$\Sigma_\mu^k = \sum_{m=1}^{\infty} \frac{\tilde{a}_m \mu_m^2}{\mu_m^2 + \lambda_k^2}(-1)^k, \tag{6.21}$$

$$\Sigma_\eta^k = \sum_{m=1}^{\infty} \frac{\tilde{\alpha}_m \eta_m}{\eta_m^2 + \lambda_k^2}(-1)^{k+m+1}. \tag{6.22}$$

Equations (6.17) and (6.19) also simplify to

$$\begin{aligned} \beta_k &= \frac{2}{k\pi \cosh \lambda_k w}\Sigma_\mu^k - b_k \frac{\sinh \lambda_k (L-w)}{\cosh \lambda_k w}, \\ b_k &= \frac{2}{h \cosh \lambda_k (L-w)}\Sigma_\eta^k + \beta_k \frac{\sinh \lambda_k w}{\cosh \lambda_k (L-w)}. \end{aligned}$$

The solutions to which are

$$b_k = \frac{2}{hk\pi \cosh \lambda_k (L-w)} \cdot \frac{k\pi \Sigma_\eta^k + h \tanh \lambda_k w \Sigma_\mu^k}{1 + \tanh \lambda_k (L-w) \tanh \lambda_k w},$$

and

$$\beta_k = \frac{2}{hk\pi \cosh \lambda_k w} \cdot \frac{h\Sigma_\mu^k - k\pi \tanh \lambda_k (L-w) \Sigma_\eta^k}{1 + \tanh \lambda_k (L-w) \tanh \lambda_k w}.$$

Finally, we introduce the notation

$$\tilde{b}_k = \frac{2}{hk\pi} \cdot \frac{k\pi \Sigma_\eta^k + h \tanh \lambda_k w \Sigma_\mu^k}{1 + \tanh \lambda_k (L-w) \tanh \lambda_k w},$$

and

$$\tilde{\beta}_k = \frac{2}{hk\pi} \cdot \frac{h\Sigma_\mu^k - k\pi \tanh \lambda_k (L-w) \Sigma_\eta^k}{1 + \tanh \lambda_k (L-w) \tanh \lambda_k w},$$

so that the solutions may be written as

$$V^t(x,y) = \mathcal{F}_0 + \sum_{m=1}^{\infty} \tilde{a}_m \sin \mu_m (y-w) \frac{\cosh \mu_m x}{\sinh \mu_m h} + \sum_{n=1}^{\infty} \tilde{b}_n \frac{\cosh \lambda_n (L-y)}{\cosh \lambda_n (L-w)} \cos \lambda_n x, \tag{6.23}$$

and

$$V^f(x,y) = F_0 y + \sum_{m=1}^{\infty} \tilde{\alpha}_m \frac{\cosh \eta_m x}{\sinh \eta_m h} \sin \eta_m y + \sum_{n=1}^{\infty} \tilde{\beta}_n \frac{\sinh \lambda_n y}{\cosh \lambda_n w)} \cos \lambda_n x. \quad (6.24)$$

6.4 Asymptotic Approximation to Truncation Errors

The expressions for the velocities (6.23) and (6.24) are exact in their current form with infinite sums. A computer can only calculate these sums using a finite number of terms, M say, and a standard Fourier Series such as the terms involving $\tilde{a}_n$ and $\tilde{\alpha}_n$ will be accurate because the $\tilde{a}_n$ and $\tilde{\alpha}_n$ can be calculated to a high degree of accuracy. In contrast, each of the $\tilde{b}_n$ and $\tilde{\beta}_n$ terms involve an infinite sum in the Σ_μ^k and Σ_η^k which each must be truncated. The number of terms required in each of the Σ_μ^k and Σ_η^k to ensure suitable convergence depends on k and so they become very costly to compute for large k. The error that arises as a result of truncating these sums can be approximated asymptotically to improve the accuracy of each of the $\tilde{b}_n$ and $\tilde{\beta}_n$. The leading order and first order approximations to Σ_μ^k are given here. Since the Σ_η^k converge at a rate of m^{-3} the corresponding asymptotic terms are negligible and so are omitted from the current work.

6.4.1 Leading Order Term

Consider Σ_μ^k in the form given by (6.21) and split the infinite sum into two, one from 1 to M and the other from $M+1$ to ∞.

$$\Sigma_\mu^k = (-1)^k \sum_{m=1}^{M} \frac{\tilde{a}_m \mu_m^2}{\mu_m^2 + \lambda_k^2} + (-1)^k \sum_{m=M+1}^{\infty} \frac{\tilde{a}_m \mu_m^2}{\mu_m^2 + \lambda_k^2}. \quad (6.25)$$

The first term can therefore be calculated numerically and the second is dealt with asymptotically assuming M is sufficiently large. Consider the term

$$\frac{\mu_m^2}{\mu_m^2 + \lambda_k^2} = \frac{1}{1 + \frac{\lambda_k^2}{\mu_m^2}}. \quad (6.26)$$

The ratio $\frac{\lambda_k}{\mu_m}$ can be writen as

$$\frac{\lambda_k}{\mu_m} = \frac{L-w}{h}\frac{k}{m-\frac{1}{2}},$$

using the definitions of λ_k and μ_m. In the current thesis L and h are comparable and so the $\frac{L-w}{h}$ term is of order $O(1)$. Similar asymptotics can be carried out for the cases of $\frac{L-w}{h} \ll 1$ and $\frac{L-w}{h} \gg 1$ but are not presented here. By taking M to be sufficiently large the ratio $\frac{\lambda_k}{\mu_m} \ll 1$. The right hand side of equation (6.26) can therefore be replaced by its Taylor series expansion for small $\frac{\lambda_k}{\mu_m}$. Thus

$$\frac{\mu_m^2}{\mu_m^2+\lambda_k^2} = 1 - \frac{\lambda_k^2}{\mu_m^2} + O\left(\frac{\lambda_k^4}{\mu_m^4}\right). \tag{6.27}$$

To leading order this reduces the expression for Σ_μ^k given by (6.25) to

$$\Sigma_\mu^k \sim (-1)^k \sum_{m=1}^{M} \frac{\tilde{a}_m \mu_m^2}{\mu_m^2+\lambda_k^2} + (-1)^k \sum_{m=M+1}^{\infty} \tilde{a}_m + O\left(\frac{\lambda_k^2}{\mu_m^2}\right). \tag{6.28}$$

We further assume that $\tilde{a}_m \sim \frac{A}{m^2}$ for sufficiently large m to reduce this to

$$\Sigma_\mu^k \sim (-1)^k \sum_{m=1}^{M} \frac{\tilde{a}_m \mu_m^2}{\mu_m^2+\lambda_k^2} + A(-1)^k \sum_{m=M+1}^{\infty} \frac{1}{m^2}.$$

The latter sum can then be written as a sum from 1 to ∞ with the terms from 1 to M subtracted off, so giving

$$\Sigma_\mu^k \sim (-1)^k \sum_{m=1}^{M} \frac{\tilde{a}_m \mu_m^2}{\mu_m^2+\lambda_k^2} + A(-1)^k \sum_{m=1}^{\infty} \frac{1}{m^2} - A(-1)^k \sum_{m=1}^{M} \frac{1}{m^2}.$$

The second sum $\sum_{m=1}^{\infty} \frac{1}{m^2}$ converges on the value $\frac{\pi^2}{6}$ and so the leading order behaviour of Σ_μ^k is written

$$\Sigma_\mu^k \sim (-1)^k \sum_{m=1}^{M} \frac{\tilde{a}_m \mu_m^2}{\mu_m^2+\lambda_k^2} + A(-1)^k \frac{\pi^2}{6} - A(-1)^k \sum_{m=1}^{M} \frac{1}{m^2}.$$

6.4.2 First Order Term

The $O\left(\frac{\lambda_k^2}{\mu_m^2}\right)$ terms in equation (6.28) can be obtained using (6.27) in the original definition of Σ_μ^k given at the start of the section, (6.21), and are found to be

$$-\frac{4}{h^2}(L-w)^2Ak^2(-1)^k\sum_{m=M+1}^{\infty}\frac{1}{m^2(2m-1)^2}. \tag{6.29}$$

The assumption $\tilde{a}_m \sim \frac{A}{m^2}$ has been applied again. The summands can be decomposed into partial fractions

$$-\frac{4}{h^2}(L-w)^2Ak^2(-1)^k\sum_{m=M+1}^{\infty}\left(\frac{8}{2m}-\frac{8}{2m-1}+\frac{4}{(2m)^2}+\frac{4}{(2m-1)^2}\right). \tag{6.30}$$

The summation of the two terms of order $O\left(\frac{1}{m}\right)$ in the parenthesise can be combined to give

$$\sum_{m=M+1}^{\infty}\left(\frac{8}{2m}-\frac{8}{2m-1}\right)=8\sum_{m=2M+1}^{\infty}\frac{(-1)^m}{m},$$

which can then be expressed as the two summations

$$\sum_{m=M+1}^{\infty}\left(\frac{8}{2m}-\frac{8}{2m-1}\right)=8\sum_{m=1}^{\infty}\frac{(-1)^m}{m}-8\sum_{m=1}^{2M}\frac{(-1)^m}{m},$$

the former of which converges on the value $-8\ln(2)$. Hence

$$\sum_{m=M+1}^{\infty}\left(\frac{8}{2m}-\frac{8}{2m-1}\right)=-8\ln(2)-8\sum_{m=1}^{2M}\frac{(-1)^m}{m}.$$

In a similar manner the remaining two terms in (6.30) can be expressed as

$$\sum_{m=M+1}^{\infty}\left(\frac{4}{(2m)^2}+\frac{4}{(2m-1)^2}\right)=\frac{2\pi^2}{3}-4\sum_{m=1}^{2M}\frac{1}{m^2}.$$

The first order term, (6.29), is therefore

$$-\frac{4}{h^2}(L-w)^2Ak^2(-1)^k\left(-8\ln(2)+\frac{2\pi^2}{3}-8\sum_{m=1}^{2M}\frac{(-1)^m}{m}-4\sum_{m=1}^{2M}\frac{1}{m^2}\right). \quad (6.31)$$

To first order, Σ_μ^k is approximated by

$$\begin{aligned}\Sigma_\mu^k \sim\ & (-1)^k\sum_{m=1}^{M}\frac{\tilde{a}_m\mu_m^2}{\mu_m^2+\lambda_k^2}+A\frac{\pi^2}{6}-A(-1)^k\sum_{m=1}^{M}\frac{1}{m^2}\\ & -\frac{4}{h^2}(L-w)^2Ak^2(-1)^k\left(\frac{2\pi^2}{3}-8\ln(2)-8\sum_{m=1}^{2M}\frac{(-1)^m}{m}-4\sum_{m=1}^{2M}\frac{1}{m^2}\right).\end{aligned}$$

6.4.3 Convergence

To check the convergence of the Σ_μ^k terms we chose a $\mathcal{G}$ which is constant, σ_b say, across the base of the tectonic plate. The $\tilde{a}_m$ are then given by (6.20) which becomes

$$\begin{aligned}\tilde{a}_m &= \frac{4\sigma_b}{(2m-1)\pi}\int_w^L \sin\mu_m(y-w)dy\\ &= \frac{8\sigma_b(L-w)}{\pi^2(2m-1)^2}.\end{aligned}$$

The value of A such that $\tilde{a}_m \sim \frac{A}{m^2}$ as $m\to\infty$ can be obtained from the limit of $\tilde{a}_m m^2$ as $m\to\infty$ which is

$$A=\lim_{m\to\infty}\tilde{a}_m m^2=\frac{2\sigma_b(L-w)}{\pi^2}. \quad (6.32)$$

The convergence of the Σ_μ^k terms are shown in Figure 6.1. Σ_μ^k is plotted against $\frac{M}{k}$ on the x axis for a range of values for k. For all values of k the truncated sum does not converge for even $M=10k$ terms. Calculating a summation over 10000 terms is costly and renders it impractical to calculate Σ_μ^k to sufficient accuracy for high values of k required to ensure convergence of the velocity field given by (6.23) and (6.24). With the addition of the leading order approximation to the truncation errors the Σ_μ^k converge well for $M=5k$. Including the first order terms in the truncation error provides sufficient convergence for values of M as low as

$2k$.

The inclusion of an asymptotic approximation to the error introduced by truncating the infinte summation in the Σ_μ^k significantly improves the convergence of these terms. A reliable and accurate analytic solution is important as it is used to check convergence of the numerical scheme given in Chapters 7 and 8.

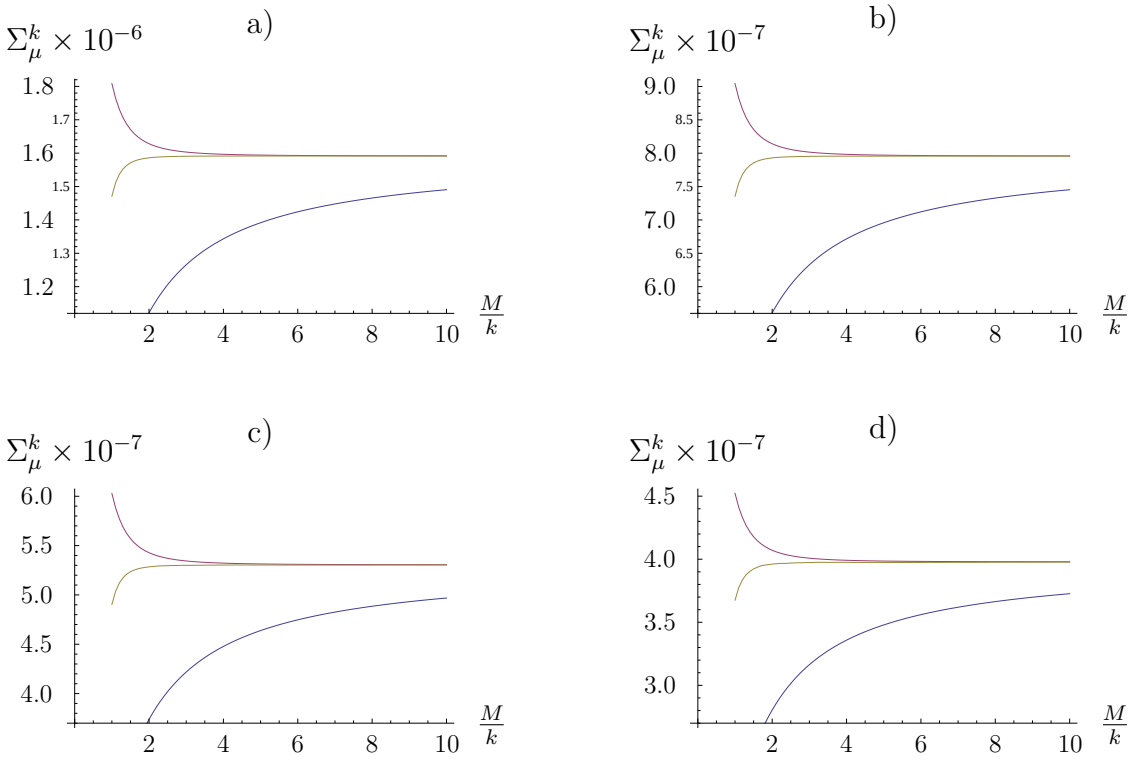

Figure 6.1: Convergence of Σ_μ^k for $k = 1000, 2000, 3000, 4000$ in plots a) - d) respectively. The blue line is the truncated sum, the purple line shows the effect of the addition of the leading order term and the yellow line has the first order term added in.

Chapter 7

Finite Difference Approximations to the Model Equations

In order to create a consistent set of algebraic simultaneous equations for the nodal values of the solution, it is necessary that the number of equations equals the number of unknowns. Since the unknowns are the nodal values of the dependent variables, the total number of unknowns is equal to the product of the number of grid points and the number of dependent variables. In the problem discussed in this thesis there is just one unknown dependent variable, the velocity V, appearing in the governing equations. Therefore, the number of unknowns is equal to the number of grid points. Therefore, for each point in the discretisation of the domain, we require an algebraic equation to be satisfied by the nodal velocities.

This section contains derivations of expressions for the finite difference approximations to the governing partial differential equations. For points in the interior of the domain we satisfy a finite difference approximation to the governing partial differential equations. These are derived in Section 7.1. At the points on the boundary we derive expressions which encapsulate the behaviour of the boundary conditions. These equations are derived in Section 7.2 for the boundaries of the fault and the tectonic plate. The first half of the section focuses on the boundaries excluding the corner points. At the corners of the domain there are two boundary conditions to satisfy and deriving one finite difference approximation which satisfies both of these takes a little more work. The second half of the section is

dedicated to the derivation of these equations. The curved nature of the elasto-plastic boundary adds much complexity and numerical treatment of this is allotted its own chapter, Chapter 8.

7.1 Finite Difference Approximations to the Governing Equations

In the tectonic plate and the fault material during its elastic phase the governing equation is Laplace's equation for the velocity, $V(x, y)$,

$$\frac{\partial^2 V}{\partial x^2}(x, y) + \frac{\partial^2 V}{\partial y^2}(x, y) = 0. \tag{7.1}$$

We non-dimensionalise this using the far field velocity, $\frac{v_0}{2}$, for the velocity and the lithosphere thickness, h, for x. The variable y gets non-dimensionalised by w in the fault and L in the tectonic plate. Laplace's equation is then written

$$\begin{aligned}
\frac{w^2}{h^2}\frac{\partial^2 \bar{V}^f}{\partial \bar{x}^2}(\bar{x}, \bar{y}) + \frac{\partial^2 \bar{V}^f}{\partial \bar{y}^2}(\bar{x}, \bar{y}) = 0, \\
\frac{L^2}{h^2}\frac{\partial^2 \bar{V}^t}{\partial \bar{x}^2}(\bar{x}, \bar{y}) + \frac{\partial^2 \bar{V}^t}{\partial \bar{y}^2}(\bar{x}, \bar{y}) = 0,
\end{aligned}$$

in the fault and the tectonic plate respectively. The superposed bar respresents the non-dimensional quantities. The domains of the fault and tectonic plate now map to unit squares in the variables $(\bar{x}, \bar{y})$ and the difference in definition of $\bar{y}$ in the two regions is assumed to be obvious from the context. Furthermore, we do not distinguish between nodal velocities in the fault and tectonic plate unless necessary and as such the superscript f and t are dropped. The two domains are discretised with N points in the x direction and K points in the y direction. In the y direction the first grid points lie on $y = 0$ and the K_p^{th} lie on $y = w$. The number of grid points across the tectonic plate is $K - K_p + 1$ and the left column of grid points in the tectonic plate coincides with the right most column in the fault. The grid spacing in the x direction is $\delta_x = \frac{1}{N-1}$ and in the y direction is $\delta_y = \frac{1}{K_p - 1}$ and $\epsilon_y = \frac{1}{K - K_p}$ in the fault and tectonic plates respectively.

Denote an arbitrary $(i,k)^{th}$ grid point in the fault by $P_{i,k}$ and its velocity by $V_{i,k}$, for $i = 2 : N-1$ and $k = 2 : K_p - 1$. The finite difference approximation for the second derivative, (3.15), can be used to write the second order approximation to Laplace's equation at $P_{i,k}$

$$\frac{w^2}{h^2}\frac{\bar{V}_{i+1,k} - 2\bar{V}_{i,k} + \bar{V}_{i-1,k}}{\delta_x^2} + \frac{\bar{V}_{i,k+1} - 2\bar{V}_{i,k} + \bar{V}_{i,k-1}}{\delta_y^2} = 0,$$

which can be factorised as

$$\frac{w^2}{h^2}\frac{\delta_y^2}{\delta_x^2}\left[\bar{V}_{i+1,k} + \bar{V}_{i-1,k}\right] - 2\left(\frac{w^2}{h^2}\frac{\delta_y^2}{\delta_x^2} + 1\right)\bar{V}_{i,k} + \bar{V}_{i,k+1} + \bar{V}_{i,k-1} = 0. \quad (7.2)$$

We adopt the convention that when V is specified in relation to the point $P_{i,k}$ in the discretisation it is the non-dimensional quantity. Otherwise it is in dimensional form unless otherwise stated. The bar notation shall now be neglected in subsequent finite difference approximations. At an arbitrary point in the tectonic plate, given by $k = K_p + 1 : K - 1$, V must satisfy

$$\frac{L^2}{h^2}\frac{\epsilon_y^2}{\delta_x^2}\left[V_{i+1,k} + V_{i-1,k}\right] - 2\left(\frac{L^2}{h^2}\frac{\epsilon_y^2}{\delta_x^2} + 1\right)V_{i,k} + V_{i,k+1} + V_{i,k-1} = 0. \quad (7.3)$$

Define the non-dimensional parameter, r, by

$$r(k) = \begin{cases} r_p = \dfrac{w\delta_y}{h\delta_x}, & k = 2 : K_p - 1 \\ r_e = \dfrac{L\epsilon_y}{h\delta_x}, & k = K_p + 1 : K - 1 \end{cases} \quad (7.4)$$

Then the two finite difference forms of Laplace's equation can be combined into the expression

$$r(k)^2\left[V_{i+1,k} + V_{i-1,k}\right] - 2\left(r(k)^2 + 1\right)V_{i,k} + V_{i,k+1} + V_{i,k-1} = 0. \quad (7.5)$$

Once part of the fault material satisfies equality in the yield criterion its governing equation in that region changes to the elasto-plastic equation, (5.37),

$$\Sigma_1 \frac{\partial^2 V}{\partial x^2} + \Sigma_3 \frac{\partial^2 V}{\partial y^2} - 2\Sigma_2 \frac{\partial^2 V}{\partial x \partial y} + M_1 \frac{\partial V}{\partial x} + M_2 \frac{\partial V}{\partial y} = 0. \tag{7.6}$$

The coefficients are restated for completeness.

$$\begin{aligned}
M_1 &= \frac{1}{\mu}\frac{\partial}{\partial x}\left\{\frac{1}{\det\Sigma}\left(\frac{1}{2\mu} + \frac{f_{23}^2}{H}\right)\right\} - \frac{1}{\mu}\frac{\partial}{\partial y}\left\{\frac{1}{\det\Sigma}\frac{f_{13}f_{23}}{H}\right\}, \\
M_2 &= -\frac{1}{\mu}\frac{\partial}{\partial x}\left\{\frac{1}{\det\Sigma}\frac{f_{13}f_{23}}{H}\right\} + \frac{1}{\mu}\frac{\partial}{\partial y}\left\{\frac{1}{\det\Sigma}\left(\frac{1}{2\mu} + \frac{f_{13}^2}{H}\right)\right\}, \\
\Sigma_1 &= \frac{1}{\mu\det\Sigma}\left(\frac{1}{2\mu} + \frac{f_{23}^2}{H}\right), \\
\Sigma_2 &= \frac{1}{\mu\det\Sigma}\frac{f_{13}f_{23}}{H}, \\
\Sigma_3 &= \frac{1}{\mu\det\Sigma}\left(\frac{1}{2\mu} + \frac{f_{13}^2}{H}\right).
\end{aligned}$$

We apply the same non-dimensionalisation as was applied to Laplace's equation in the fault with the addition of the definitions $M_i = \frac{1}{w}\bar{M}_i$. The non-dimensional form of equation (7.6) is therefore

$$\Sigma_1 \frac{w^2}{h^2}\frac{\partial^2 \bar{V}}{\partial \bar{x}^2} + \Sigma_3 \frac{\partial^2 \bar{V}}{\partial \bar{y}^2} - 2\Sigma_2 \frac{w}{h}\frac{\partial^2 \bar{V}}{\partial \bar{x}\partial \bar{y}} + \bar{M}_1 \frac{w}{h}\frac{\partial \bar{V}}{\partial \bar{x}} + \bar{M}_2 \frac{\partial \bar{V}}{\partial \bar{y}} = 0. \tag{7.7}$$

Using the second order, centred finite difference expressions for the derivatives given in Section 3.1 the elasto-plastic equation (7.6) can be approximated at $P_{i,k}$ by

$$\begin{aligned}
&2r_p^2\Sigma_1^{i,k}[V_{i+1,k} + V_{i-1,k} - 2V_{i,k}] + 2\Sigma_3^{i,k}[V_{i,k+1} + V_{i,k-1} - 2V_{i,k}] \\
&-r_p h\delta\Sigma_2^{i,k}\left[V_{i+1,k+1} - V_{i+1,k-1} - V_{i-1,k+1} + V_{i-1,k-1}\right] \\
&+r_p M_1^{i,k}[V_{i+1,k} - V_{i-1,k}] + M_2^{i,k}[V_{i,k+1} - V_{i,k-1}] = 0,
\end{aligned}$$

where the superscripts i, k correspond to the value at the point $P_{i,k}$ and carry the same meaning as the subscripts on V. It is understood that all terms are the

non-dimensional quantities when specified at $P_{i,k}$. This can be rearranged into the form

$$\begin{aligned} & r_p \left[2r_p\Sigma_1^{i,k} + M_1^{i,k}\right] V_{i+1,k} + r_p \left[2r_p\Sigma_1^{i,k} - M_1^{i,k}\right] V_{i-1,k} \\ & -2 \left[2r_p^2\Sigma_1^{i,k} + 2\Sigma_3^{i,k}\right] V_{i,k} + \left[2\Sigma_3^{i,k} + M_2^{i,k}\right] V_{i,k+1} \\ & + \left[2\Sigma_3^{i,k} - M_2^{i,k}\right] V_{i,k-1} - r_p\Sigma_2^{i,k} \left[V_{i+1,k+1} - V_{i+1,k-1}\right. \\ & \qquad \left. - V_{i-1,k+1} + V_{i-1,k-1}\right] = 0. \end{aligned} \tag{7.8}$$

7.2 Finite Difference Approximations to the Boundary Conditions

The previous section presented approximations to the governing partial differential equations at general interior points in the domain. We now derive expressions which approximate the boundary conditions. Dirichlet boundary conditions can be incorporated into a numerical scheme by prescribing the nodal values of the solution at grid points which lie on the boundary. This is applied at the grid points down the centre of the fault. Neuman boundary conditions require their derivatives to be replaced by finite difference approximations.

7.2.1 Finite Difference Approximations on the Open Interval Parts of the Boundary

The boundary condition on the right hand edge of the domain, as given by (5.19), is

$$\left.\frac{\partial V}{\partial y}\right|_{y=L} = 0. \tag{7.9}$$

Non-dimensionalising and then replacing the derivative by the finite difference approximation (3.7) yields

$$\frac{V_{i,K+1} - V_{i,K-1}}{2\epsilon_y} = 0, \tag{7.10}$$

or equivalently $V_{i,K+1} = V_{i,K-1}$. The point $P_{i,K+1}$ is outside the domain and so this finite difference introduces additional unknowns to the problem. This in turn requires an additional equation to maintain a consistency in the system. Assuming that Laplace's equation also holds at grid points on the boundary provides this necessary equation. The finite difference form of Laplace's equation, (7.5), on the boundary takes the form

$$r_e^2 \left[V_{i+1,K} + V_{i-1,K}\right] - 2\left(r_e^2 + 1\right) V_{i,K} + V_{i,K+1} + V_{i,K-1} = 0, \qquad (7.11)$$

for $i = 2 : N-1$. The two corner points represented by $i = 1, N$ are special cases and are dealt with later in the section. Computing a solution using a numerical method can take a considerable length of time, due to the vast number of grid points that are often required. In the interest of minimising the number used in this problem we eliminate $V_{i,K+1}$ at this point to maintain a system containing only $N \times K$ grid points. Substituting (7.10) into (7.11) gives the equation

$$r_e^2 \left[V_{i+1,K} + V_{i-1,K}\right] - 2\left(r_e^2 + 1\right) V_{i,K} + 2V_{i,K-1} = 0. \qquad (7.12)$$

Consider the boundary condition on the top edge of the domain, (5.17) and (5.18). The analogous expression to (7.12) for the grid points along the boundary defined by $x = 0$ is

$$2r(k)^2 V_{2,k} - 2\left(r(k)^2 + 1\right) V_{1,k} + V_{1,k+1} + V_{1,k-1} = 0, \qquad (7.13)$$

valid for $k = 2 : K_p - 1$ and $k = K_p + 1 : K - 1$. This is valid for $k = K_p + 1 : K - 1$ for all times and for $k = 2 : K_p - 1$ when the fault material at these points has not reached yield. When the points on the upper surface of the fault reach yield the governing equation changes to (7.8), these equations are already rather cumbersome and together with the more complicated definitions of the stresses, (5.15) and (5.16), the analogous method to that used to derive (7.13) is impractical. Instead we use the second order forwards difference, (3.11), for the x derivative in (5.18) together with a centred difference for the y derivative

$$-r_p \Sigma_1^{1,k} \left[3V_{1,k} - 4V_{2,k} + V_{3,k}\right] - \Sigma_2^{1,k} \left[V_{1,k+1} + V_{1,k-1}\right] = 0.$$

Thus by using a one-sided difference to approximate the x derivative we have avoided introducing any additional unknowns which require additional steps to eliminate. The point P_{1,K_p} lies on 2 boundaries and the finite difference approximation is left until later in the section.

The inhomogeneous basal boundary condition given by (5.21) and (5.22) is non-dimensionalised to

$$\left.\frac{\partial \bar{V}}{\partial \bar{x}}\right|_{\bar{x}=1} = \frac{2h}{v_0}\bar{\mathcal{G}}(\bar{y}). \tag{7.14}$$

The derivative is replaced by the centred finite difference (3.7) such that

$$\frac{V_{N+1,k} - V_{N-1,k}}{2\delta} = \bar{\mathcal{G}}_k.$$

This can be rearranged and the $V_{N+1,k}$ term eliminated in the finite difference approximation of Laplace's equation at the grid points where $i = N$ to obtain

$$2r(k)^2 V_{N-1,k} - 2\left(r(k)^2 + 1\right) V_{N,k} + V_{N,k+1} + V_{N,k-1} = -2\delta_x r(k)^2 \bar{\mathcal{G}}_k. \tag{7.15}$$

This is valid for $k = K_p + 1 : K - 1$ for all times and for $k = 2 : K_p - 1$ when the fault material at these points has not reached yield. When the lower portion of the fault reaches yield the boundary condition is given by (5.22). We use the second order backwards difference, (3.10), for the x derivative in $\dot{\sigma}_{13}$ and equate this to $\mathcal{G}(y)$. First, non-dimensionalise the boundary condition

$$\frac{w}{h}\bar{\Sigma}_1 \frac{\partial \bar{V}}{\partial \bar{x}} - \bar{\Sigma}_2 \frac{\partial \bar{V}}{\partial \bar{y}} = \frac{4w}{v_0}\bar{\mathcal{G}}(\bar{y}),$$

and then replace the derivatives by finite difference approximations

$$r_p \bar{\Sigma}_1^{N,k} \left[3V_{N,k} - 4V_{N-1,k} + V_{N-2,k}\right] - \bar{\Sigma}_2^{N,k} \left[V_{N,k+1} + V_{N,k-1}\right] = \frac{4\delta_x w}{h}\bar{\mathcal{G}}_k.$$

This boundary equation holds for $k = 2 : K_p - 1$ when these points are in yield.

Along the edge of the fault there are two continuity boundary conditions which are applied, (5.24) and (5.27). A point P_{i,K_p} on this boundary lies on the boundary of both the fault domain and the tectonic plate domain. Denote the limit of the velocity at this point when approached from the left hand side by V^f_{i,K_p}. Namely,

$$\lim_{y\to w^-} V((i-1)\delta h, y) = \frac{v_0}{2} V^f_{i,K_p},$$

where $(i-1)\delta h$ is the x coordinate of the i^{th} row of grid points. Similarly, the limiting value for the velocity when approached from the right hand side is defined as

$$\lim_{y\to w^+} V((i-1)\delta h, y) = \frac{v_0}{2} V^t_{i,K_p},$$

The value of V^f_{i,K_p} is required in the finite difference equation representing Laplace's equation at a point P_{i,K_p-1}. Namely,

$$r_p^2 \left[V_{i+1,K_p-1} + V_{i-1,K_p-1}\right] - 2\left(r_p^2+1\right) V_{i,K_p-1} + V^f_{i,K_p} + V_{i,K_p-2} = 0.$$

Likewise, the value of V^t_{i,K_p} also appears in the finite difference equation imposed at the $^{th}_{i,K_p+1}$ grid point,

$$r_e^2 \left[V_{i+1,K_p+1} + V_{i-1,K_p+1}\right] - 2\left(r_e^2+1\right) V_{i,K_p+1} + V_{i,K_p+2} + V^t_{i,K_p} = 0.$$

By setting $V^f_{i,K_p} = V^t_{i,K_p} = V_{i,K_p}$, continuity of velocity is obtained. Continuity of normal traction rate is approximated by using the second order backwards difference, (3.10), for the y derivative at the edge of the fault and the second order forward difference, (3.11), for the derivative at the edge of the tectonic plate. By first non-dimensionalising and then applying continuity of velocity the finite difference approximation to (5.25) at P_{i,K_p} is written

$$3V_{i,K_p} - 4V_{i,K_p-1} + V_{i,K_p-2} = \frac{w\delta_y}{L\epsilon_y}\left[-3V_{i,K_p} + 4V_{i,K_p+1} - V_{i,K_p+2}\right]. \quad (7.16)$$

This equation only holds during the elastic phase of the fault, once in yield the left hand side of (7.16) must be replaced by the analogous expression (5.26). Thus

$$-\frac{w\delta_y}{h\delta_x}\Sigma_2^{i,K_p}\left[V_{i+1,K_p}-V_{i-1,K_p}\right]+\Sigma_3^{i,K_p}\left[3V_{i,K_p}-4V_{i,K_p-1}+V_{i,K_p-2}\right]$$
$$=\frac{w\delta_y}{L\epsilon_y}\left[-3V_{i,K_p}+4V_{i,K_p+1}-V_{i,K_p+2}\right]. \tag{7.17}$$

7.2.2 Finite Difference Approximations at the Corners of the Domain

The corners are subject to both of the boundary conditions on the edges of the domain which radiate from them and expressions which encapsulate this are presented here.

Consider the two corners on the right hand side of the domain. The corner at $(0, L)$ is one such point and must satisfy both (5.17) and (5.19). Equation (7.13) satisfies the boundary condition on the upper surface and into this can be substituted the other boundary condition given by (7.10)

$$2r_e^2V_{2,K}-2\left(r_e^2+1\right)V_{1,K}+2V_{1,K-1}=0.$$

This now satisfies both the boundary conditions as required. Similarly, at (h, L) equation (7.10) can be substituted into (7.15) to yield

$$2r_e^2V_{N-1,K}-2\left(r_e^2+1\right)V_{N,K}+2V_{N,K-1}=-2\delta_v r_e^2\bar{\mathcal{G}}_K, \tag{7.18}$$

which satisfies both the conditions (5.19) and (5.20).

The point at the top of the edge of the fault at $(\mathbf{0}, \mathbf{w})$ is part of the top boundary and the velocity, therefore, must satisfy (5.17) which has an analogous finite difference approximation to (7.10). This gives the condition $V_{2,K_p} = V_{0,K_p}$. This condition is used previously to eliminate the V_{0,K_p} term from the finite difference form of the governing equation. As the point $(0, w)$ lies on the boundary of the fault and the tectonic plate it has the potential to be governed by both of the

forms of Laplace's equation (7.2) and (7.5). Only one, however, can be applied. Fortunately, the choice is arbitrary and, with a mesh which gives sufficient convergence, the solutions obtained using the two different choices are indistinguishible. The choice is made to choose the equation satisfied in the tectonic plate. The top boundary condition is then satisfied by

$$2r_e^2 V_{2,K_p} - 2\left(r_e^2+1\right)V_{1,K_p} + V_{1,K_p+1} + \bar{V}\left(0, \frac{w}{L} - \epsilon_y\right) = 0. \tag{7.19}$$

The term with the superposed bar replaces the term that has previously been denoted V_{i,K_p-1} which was the velocity at the point P_{i,K_p-1}. Its value is the velocity a distance ϵ_y from the point $(0, w)$ in the negative y direction. This point is not only outside the domain of the tectonic plate but, due to the different grid spacings used in the fault and the tectonic plate, may not coincide with a grid point. Therefore we must eliminate this term from the equation and replace it with expressions including V evaluated at existing grid points using the boundary condition on $y = w$. First, approximate the y derivative at the point $(0, w)$ using the centred finite difference (3.7), viewed as part of the tectonic plate

$$\left.\frac{\partial V}{\partial y}\right|_{1,K_p} = \frac{V_{1,K_p+1} - \bar{V}\left(0, \frac{w}{L} - \epsilon_y\right)}{2\epsilon_y}.$$

Using the boundary condition along $y = w$ the left hand side can be replaced by the backwards difference, (3.10), and taking into account the different non-dimensionalisations in the two regions this becomes

$$\frac{L}{w}\left(\frac{3V_{1,K_p-2} - 4V_{1,K_p-1} + V_{1,K_p}}{2\delta_y}\right) = \frac{V_{1,K_p+1} - \bar{V}\left(0, \frac{w}{L} - \epsilon_y\right)}{2\epsilon_y}. \tag{7.20}$$

This can then be substituted into (7.19) to eliminate $\bar{V}\left(0, \frac{w}{L} - \epsilon_y\right)$

$$2r_e^2 V_{2,K_p} - 2\left(r_e^2+1\right)V_{1,K_p} + 2V_{1,K_p+1} - \frac{L\epsilon_y}{w\delta_y}\left[3V_{1,K_p-2} - 4V_{1,K_p-1} + V_{1,K_p}\right] = 0. \tag{7.21}$$

When the top of the fault reaches yield the finite difference approximation on the edge of the fault is given by (7.17) with $i = 1$

$$-\frac{w\delta_y}{h\delta_x}\Sigma_2^{1,K_p}\left[V_{2,K_p} - V_{0,K_p}\right] + \Sigma_3^{1,K_p}\left[3V_{1,K_p} - 4V_{1,K_p-1} + V_{1,K_p-2}\right] = \frac{w\delta_y}{L\epsilon_y}\left[-3V_{1,K_p} + 4V_{1,K_p+1} - V_{1,K_p+2}\right],$$

The finite difference approximation to the top boundary condition on the top of the tectonic plate gives $V_{2,K_p} = V_{0,K_p}$, as previously discussed. This, together with continuity of velocity across $y = w$, is used to eliminate V_{0,K_p} and give

$$\Sigma_3^{1,K_p}\left[3V_{1,K_p} - 4V_{1,K_p-1} + V_{1,K_p-2}\right] = \frac{w\delta_y}{L\epsilon_y}\left[-3V_{1,K_p} + 4V_{1,K_p+1} - V_{1,K_p+2}\right].$$

Consider the corner at the base of the edge of the fault. When the material at the point (h, w) is in its elastic phase, the boundary conditions can be approximated in a similar manner to the point $(0, w)$. Begin with the equation approximating the basal boundary condition (7.15)

$$2r_e^2 V_{N-1,K_p} - 2\left(r_e^2 + 1\right)V_{N,K_p} + V_{N,K_p+1} + \bar{V}\left(h, \frac{w}{L} - \epsilon_y\right) = -2\delta_x r_e^2 \bar{\mathcal{G}}_{K_p},$$

and then eliminate the $\bar{V}\left(h, \frac{w}{L} - \epsilon_y\right)$ term using the finite difference approximation to the boundary condition along $y = w$, which is analogous to (7.20), namely

$$2r_e^2 V_{N-1,K_p} - 2\left(r_e^2 + 1\right)V_{N,K_p} + 2V_{N,K_p+1} - \frac{L\epsilon_y}{w\delta_y}\left[3V_{N,K_p-2} - 4V_{N,K_p-1} + V_{N,K_p}\right] = 0. \tag{7.22}$$

When the fault material reaches yield, continuity of traction-rate boundary condition given by (5.24) can be expressed as

$$\frac{\partial V^e}{\partial y} = -\bar{\Sigma}_2\frac{\partial V^p}{\partial x} + \bar{\Sigma}_3\frac{\partial V^p}{\partial y}. \tag{7.23}$$

The two y derivatives are approximated by second order accurate one-sided differences. Using the continuity of velocity boundary condition, the x derivative on the

edge of the fault can be replaced by the x derivative on the edge of the tectonic plate. This can subsequently be replaced by $\mathcal{G}$ to apply the second boundary condition that holds at the base of the lithosphere. Collectively, the finite difference approximations to the derivatives in the boundary condition (7.23) give

$$\begin{aligned}&\bar{\Sigma}_3^{N,K_p}\left(3\bar{V}_{N,K_p} - 4\bar{V}_{N,K_p-1} + \bar{V}_{N,K_p-2}\right)\\ &+\frac{w\delta_y}{L\epsilon_y}\left(3\bar{V}_{N,K_p} - 4\bar{V}_{N,K_p+1} + \bar{V}_{N,K_p+2}\right) = 2w\delta_y\bar{\Sigma}_2^{N,K_p}\bar{\mathcal{G}}_{K_p}.\end{aligned}$$

Chapter 8

Finite Difference Approximations at the Elasto-Plastic Interface

8.1 Finite Differences Along a Curved Boundary

As mentioned in Chapter 7, curved boundaries can present a problem for numerical methods, especially the finite difference method which is most efficient on regular meshes. A compromise has to be met between the complexity of the numerical scheme and the treatment of the boundary conditions. The added complications at the boundaries for the FD method are often tolerated in order to benefit from the straightforward nature of the method at internal points away from the boundary. One method of incorporating the boundary conditions is to approximate the shape of the boundary by the edges of the mesh, Heaps [1973]. This is perhaps the simplest treatment but has the disadvantage of large errors in the solution near the boundary. Another method is to formulate the problem relative to a curvilinear coordinate system defined such that the curved boundary lies parallel to one of the axes, Thompson et al. [1974], Ryskin and Leal [1984] and Visbal and Gaitonde [2002]. This can often lead to more complicated governing equations in the curvilinear coordinate system and requires prior knowledge of the shape of the boundary before obtaining the solution. This requires an iterative method in the case of Ryskin and Leal [1984]. Furthermore, it is futile in finite domains with both curved and straight boundaries as it is rarely possible to also preserve the

straight boundaries during the transformation. Alternatively, the use of less standard forms of higher order accurate finite difference approximations can be used but often lose the simplicity associated with rectangular meshes, Liszka and Orkisz [1980] and Noye and Arnold [1990]. It is this method that is used in this thesis. We present a method that uses interpolation of the velocities onto non-standard grid points in order to maintain the simpler finite difference expressions on regular meshes. The main advantage of this method is that it uses a standard template of code that is applicable to all encountered elasto-plastic boundary positions. This is a novel method and has not been found in other publications. This simplicity does not come at the expense of the accuracy of the numerical scheme as reported by other methods. Convergence plots are presented at the end of the chapter for the elastic-elastic problem in which the entire fault is elastic but divided by an arbitrary curved boundary. The numerical results are compared with the analytic solution derived in Chapter 6.

To find the position of the elasto-plastic boundary each column of grid points, defined as the set of grid points positioned on lines of constant y, is treated separately. The stresses are calculated at each of the grid points in the column and the yield function evaluated. The elasto-plastic region is defined by $f = 0$, the elastically deforming region of the fault material is given by $f < 0$ and the boundary is then represented by the smallest x value at which $f = 0$. Using interpolation between the values of the discretised yield function down each column of grid points it is possible to approximate the smallest x value where $f = 0$. This can be carried out down each set of grid points defined by $y = const$ to find a set of points (z_n, y_n) which represent the discretised boundary between the elastically deforming fault material and the elasto-plastic regions. Here y_n represents the regularly spaced discretised points in the y direction across the fault and z_n represents the x-coordinate of the boundary at each of these values. The points (z_1, y_1) and (z_{K_p}, y_{K_p}) lie on $y = 0$ and $y = w$ respectively. These grid points on the interface are then added to the discretisation. We denote the number of the grid point in the n^{th} column which represents the elasto-plastic boundary as counted from the top boundary as m_n. For example, the $(m_n, n)^{th}$ grid point has the coordinates (z_n, y_n). We further denote the x coordinate of the point above the boundary by (x_n, y_n).

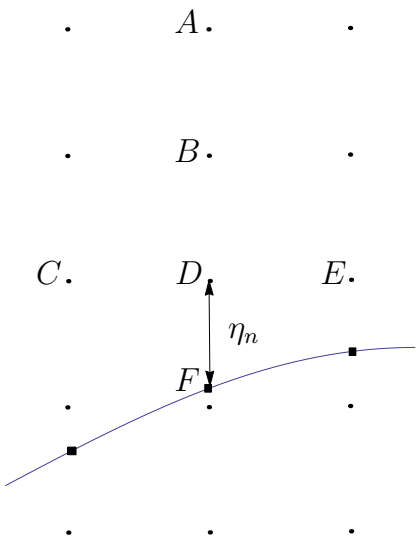

Figure 8.1: A representative section of the boundary with labelled points included in the finite difference approximations about D.

8.1.1 The Points Directly Above the Boundary

Following on from the notation explained at the start of the chapter, the point directly above the boundary point of the n^{th} column will be in the $(m_n - 1, n)^{th}$ position. The discretisation of Laplace's equation at this point shall be relative to the x and y directions and have irregular spaced points in the x direction but regular spacing in the y direction. Using *a posteriori* knowledge about the approximate horizontal nature of the elasto-plastic boundary we assume that the irregular grid spacing only affects the finite difference approximations at points directly above and below the boundary. The method can be extended to steeper boundaries but is unnecessary for the current problem and so is not presented here.

We begin by writing the finite difference approximation to Laplace's equation using the regular second y derivative (3.12) and the second x derivative on an irregular mesh (3.24). The point D in Figure 8.1 represents the $(m_n - 1)^{th}$ point of the n^{th} column. The x derivative is expressed in terms of V at the points A, B, D and F and the y derivative is given in terms of the velocity at the points C, D and E. Either or both of the points C and E can fall above or below the boundary depending on the local shape of the boundary; three of the possibilities are shown in Figures 8.1 and 8.2. Define the distance between D and F by η_n. The second

x derivative, (3.24), can therefore be written as

$$\begin{aligned} f''(x) &= \left(\frac{3\delta+\eta_n}{2\delta^2\eta_n}\right) f(x) \\ &\quad +2\left(\frac{2\delta-\eta_n}{\delta^2(\delta+\eta_n)}\right) f(x-\delta) \\ &\quad +\left(\frac{6\delta}{\eta_n(\delta+\eta_n)(2\delta+\eta_n)}\right) f(x+\eta_n) \\ &\quad +\left(\frac{\eta_n-\delta}{\delta^2(2\delta+\eta_n)}\right) f(x-2\delta). \end{aligned}$$

Laplace's equation at the points just above the elasto-plastic boundary can then be approximated by

$$\begin{aligned} & r_p^2\frac{\delta_y^2}{\delta^2}\left[+2\left(\frac{2\delta-\eta_n}{\delta^2(\delta+\eta_n)}\right) V_{m_j-2,j}\right. \\ & \left.+\left(\frac{6\delta}{\eta_n(\delta+\eta_n)(2\delta+\eta_n)}\right) V_{m_j,j}+\left(\frac{\eta_n-\delta}{\delta^2(2\delta+\eta_n)}\right) V_{m_j-3,j}\right] \\ & +\left[\frac{3\delta+\eta_n}{2\delta^2\eta_n}-2\right] V_{m_j-1,j}+V_C^e+V_E^e=0, \end{aligned} \tag{8.1}$$

where V_C^e and V_E^e are the values of the velocity at the points C and E respectively. In the case of figure 8.1 these are $V_{m_j-1,j-1}$ and $V_{m_j-1,j+1}$, however, it is possible that the points C and E lie below the elasto-plastic boundary as shown in Figure 8.2. Consequently, the standard nodal values, $V_{m_j-1,j-1}$ or $V_{m_j-1,j+1}$, cannot be used in the finite difference approximation at a point above the boundary. A derivation of the expressions used for these points is given in Section 8.2.

8.1.2 The Points Directly Below the Boundary

An equivalent expression to (8.1) for the elasto-plastic equation (5.37) can be derived using the points labelled $A, ..., F$ in Figure 8.3. The second derivative for

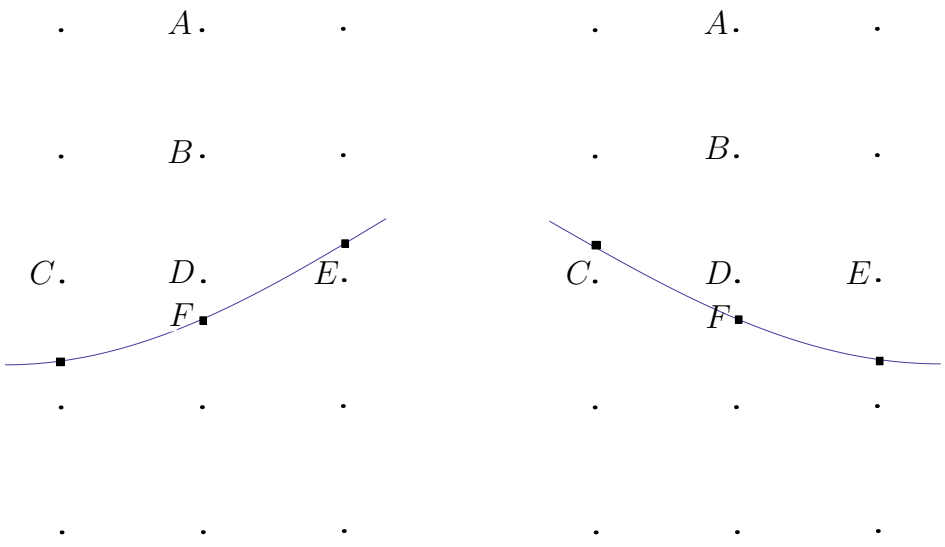

Figure 8.2: Figure showing two possible positions of the elasto-plastic boundary within the regularly spaced grid. The additional grid points on the boundary are represented by the square dots.

x given by (3.24) can be written as

$$\begin{aligned} f''(x) &= \left(\frac{4\delta-\eta_n}{2\delta\left(\delta-\eta_n\right)}\right) f(x) \\ &\quad + \left(\frac{6\delta}{\left(\delta-\eta_n\right)\left(2\delta-\eta_n\right)(3\delta-\eta_n)}\right) f(x-(\delta-\eta_n)) \\ &\quad +2\left(\frac{\delta+\eta_n}{\delta^2(2\delta-\eta_n)}\right) f(x+\delta) \\ &\quad -\left(\frac{\eta_n}{\delta^2(3\delta-\eta_n)}\right) f(x+2\delta), \end{aligned} \tag{8.2}$$

the centered difference approximation for the first derivative on an irregular grid is given by (3.11)

$$f'(x) = \frac{\eta_n\left(2\delta-\eta_n\right) f(x) + \left(\delta-\eta_n\right)^2 f(x+\delta) - \delta^2 f\left(x-(\delta-\eta_n)\right)}{\delta\left(\delta-\eta_n\right)\left(2\delta-\eta_n\right)},$$

and the mixed derivative with a forward difference in the x direction is given by

$$\begin{aligned} f'(x) &= \frac{-3}{4\delta\delta_y}\left[f(x,y+\delta_y)-f(x,y-\delta_y)\right] \\ &+\frac{1}{2\delta\delta_y}\left[f(x+\delta,y+\delta_y)-f(x+\delta,y-\delta_y)\right] \\ &-\frac{1}{4\delta\delta_y}\left[f(x+2\delta,y+\delta_y)-f(x+2\delta,y-\delta_y)\right]. \end{aligned}$$

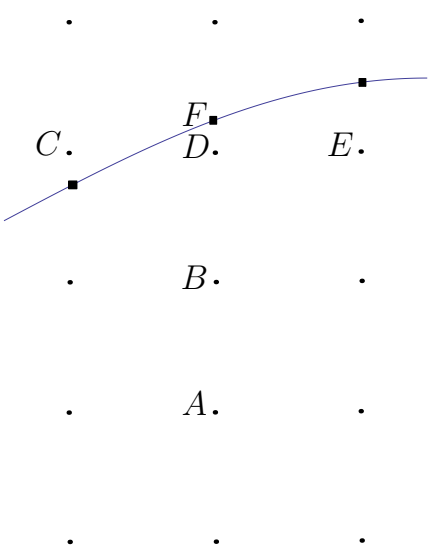

Figure 8.3: A representative section of the elasto-plastic boundary with labelled points included in the finite difference equation at a point D below the boundary.

The governing equation at points below the boundary can then be expressed

using the velocities at the points $A, ..., F$ as given by Figure 8.3

$$
\begin{aligned}
&2\Sigma_1^{m_j+1,j}\frac{w^2}{h^2}\left(\frac{4\delta-\eta_n}{2\delta\left(\delta-\eta_n\right)}\right)V_{m_j+1,j}\\
&+2\Sigma_1^{m_j+1,j}\frac{w^2}{h^2}\left(\frac{6\delta\delta_y^2}{\left(\delta-\eta_n\right)\left(2\delta-\eta_n\right)(3\delta-\eta_n)}\right)V_{m_j,j}\\
&+4\Sigma_1^{m_j+1,j}\frac{w^2}{h^2}\left(\frac{\delta_y^2(\delta+\eta_n)}{\delta^2(2\delta-\eta_n)}\right)V_{m_j+2,j}-2\Sigma_1^{m_j+1,j}\frac{w^2}{h^2}\left(\frac{\delta_y^2\eta_n}{\delta^2(3\delta-\eta_n)}\right)V_{m_j+3,j}\\
&+2\Sigma_3^{m_j+1,j}[V_C^p+V_E^p-2V_{m_j+1,j}]+3\Sigma_2^{m_j+1,j}\frac{w}{h}\frac{\delta_y}{\delta}\left[V_E-V_C\right]\\
&-\frac{1}{2}\Sigma_2^{m_j+1,j}\frac{w}{h}\frac{\delta_y}{\delta}\left[V_{m_j+2,j+1}-V_{m_j+2,j-1}\right]+\Sigma_2\frac{w}{h}\frac{\delta_y}{\delta}\left[V_{m_j+3,j+1}-V_{m_j+3,j-1}\right]\\
&+M_1^{m_j+1,j}\frac{w}{h}\frac{2\delta_y^2\eta_n\left(2\delta-\eta_n\right)}{\delta\left(\delta-\eta_n\right)\left(2\delta-\eta_n\right)}V_{m_j+1,j}+M_1^{m_j+1,j}\frac{w}{h}\frac{2\delta_y^2\left(\delta-\eta_n\right)^2}{\delta\left(\delta-\eta_n\right)\left(2\delta-\eta_n\right)}V_{m_j+2,j}\\
&-M_1^{m_j+1,j}\frac{w}{h}\frac{2\delta^2\delta_y^2}{\delta\left(\delta-\eta_n\right)\left(2\delta-\eta_n\right)}V_{m_j,j}+M_2^{m_j+1,j}[V_E^p-V_C^p]=0.
\end{aligned}
$$

This can be factorised to give

$$\begin{aligned}
&\left[2\Sigma_1^{m_j+1,j}\frac{w^2}{h^2}\left(\frac{\eta_n^2\delta_y^2}{\delta^2(2\delta-\eta_n)(\delta-\eta_n)}\right)-4\Sigma_3^{m_j+1,j}\right.\\
&\left.+M_1^{m_j+1,j}\frac{w}{h}\frac{2\delta_y^2\eta_n(2\delta-\eta_n)}{\delta(\delta-\eta_n)(2\delta-\eta_n)}\right]V_{m_j+1,j}\\
&+\left[2\Sigma_1^{m_j+1,j}\frac{w^2}{h^2}\left(\frac{6\delta\delta_y^2}{(\delta-\eta_n)(2\delta-\eta_n)(3\delta-\eta_n)}\right)\right.\\
&\left.-M_1^{m_j+1,j}\frac{w}{h}\frac{2\delta^2\delta_y^2}{\delta(\delta-\eta_n)(2\delta-\eta_n)}\right]V_{m_j,j}\\
&+\left[4\Sigma_1^{m_j+1,j}\frac{w^2}{h^2}\left(\frac{\delta_y^2(\delta+\eta_n)}{\delta^2(2\delta-\eta_n)}\right)+M_1^{m_j+1,j}\frac{w}{h}\frac{2\delta_y^2(\delta-\eta_n)^2}{\delta(\delta-\eta_n)(2\delta-\eta_n)}\right]V_{m_j+2,j}\\
&-2\Sigma_1^{m_j+1,j}\frac{w^2}{h^2}\left(\frac{\delta_y^2\eta_n}{\delta^2(3\delta-\eta_n)}\right)V_{m_j+3,j}\\
&+\left[2\Sigma_3^{m_j+1,j}-3\Sigma_2^{m_j+1,j}\frac{w}{h}\frac{\delta_y}{\delta}-M_2^{m_j+1,j}\right]V_C^p\\
&+\left[2\Sigma_3^{m_j+1,j}+3\Sigma_2^{m_j+1,j}\frac{w}{h}\frac{\delta_y}{\delta}+M_2^{m_j+1,j}\right]V_E^p\\
&-\frac{1}{2}\Sigma_2^{m_j+1,j}\frac{w}{h}\frac{\delta_y}{\delta}\left[V_{m_j+2,j+1}-V_{m_j+2,j-1}\right]\\
&+\Sigma_2^{m_j+1,j}\frac{w}{h}\frac{\delta_y}{\delta}\left[V_{m_j+3,j+1}-V_{m_j+3,j-1}\right]=0. \qquad (8.3)
\end{aligned}$$

8.2 Quadratic Interpolation-Extrapolation Method

In this section we derive expressions for V_C^e, V_E^e, V_C^p and V_E^p using quadratic interpolation between the points vertically above or below the boundary. This quadratic is then used to extrapolate the velocity smoothly from one region to ficticious points located at C or E outside of that region. We focus our attention first on the terms with a superscript e. Interpolate the velocity through the three points (m_n, n), (m_n-1, n) and (m_n-2, n) using a quadratic so that the velocity $\mathcal{V}$ at a point x is given by

$$\mathcal{V} = \alpha_n^e x^2 + \beta_n^e x + \gamma_n^e. \qquad (8.4)$$

At each of the three points this quadratic can be evaluated to give three simultaneous equations involving α_n^e, β_n^e and γ_n^e.

$$\begin{aligned} V_{m_n-2,n} &= \alpha_n^e \left(x_n-\delta\right)^2 + \beta_n^e \left(x_n-\delta\right) + \gamma_n^e, && (8.5)\\ V_{m_n-1,n} &= \alpha_n^e x_n^2 + \beta_n^e x_n + \gamma_n^e, && (8.6)\\ V_{m_n,n} &= \alpha_n^e z_n^2 + \beta_n^e z_n + \gamma_n^e. && (8.7) \end{aligned}$$

The differences (8.7)-(8.6) and (8.6)-(8.5) give

$$\begin{aligned} V_{m_n,n} - V_{m_n-1,n} &= \alpha_n^e \left(z_n^2 - x_n^2\right) + \beta_n^e \left(z_n - x_n\right) \\ &= \alpha_n^e \eta_n \left(z_n + x_n\right) + \beta_n^e \eta_n, && (8.8)\\ V_{m_n-1,n} - V_{m_n-2,n} &= \alpha_n^e \left(x_n^2 - \left(x_n-\delta\right)^2\right) + \beta_n^e \delta \\ &= \alpha_n^e \delta \left(2x_n - \delta\right) + \beta_n^e \delta. && (8.9) \end{aligned}$$

Taking a linear combination of (8.8) and (8.9) eliminates β_n^e to leave

$$\delta V_{m_n,n} - \left(\delta+\eta_n\right) V_{m_n-1,n} + \eta_n V_{m_n-2,n} = \alpha_n^e \eta_n \delta \left[z_n + x_n - \left(2x_n - \delta\right)\right],$$

which can be rearranged to give

$$\alpha_n^e = \frac{\delta V_{m_n,n} - \left(\delta+\eta_n\right) V_{m_n-1,n} + \eta_n V_{m_n-2,n}}{\eta_n \delta \left[z_n + x_n - \left(2x_n - \delta\right)\right]}.$$

Then (8.8) can be used to find β_n^e,

$$\beta_n^e = \frac{1}{\eta_n} V_{m_n,n} - \frac{1}{\eta_n} V_{m_n-1,n} - \alpha_n^e \left(z_n + x_n\right),$$

and finally (8.7) gives γ_n^e,

$$\gamma_n^e = V_{m_n,n} - \alpha_n^e z_n^2 - \beta_n^e z_n.$$

Introduce vector forms of α_n^e, β_n^e and γ_n^e such that $\alpha_n^e = \underline{\alpha}_n^e \cdot \mathbf{v}_n$, $\beta_n^e = \underline{\beta}_n^e \cdot \mathbf{v}_n$ and $\gamma_n^e = \underline{\gamma}_n^e \cdot \mathbf{v}_n$ where $\mathbf{v}_n$ is the vector

$$\mathbf{v}_n^e = \left(V_{m_n-2,n}, V_{m_n-1,n}, V_{m_n,n}\right).$$

This then requires the following definitions for $\underline{\alpha}_n^e$, $\underline{\beta}_n^e$ and $\underline{\gamma}_n^e$

$$\begin{aligned}
\underline{\alpha}_n^e &= \frac{(\eta_n, -(\delta+\eta_n), \delta)}{\eta_n \delta (\delta+\eta_n)}, \\
\underline{\beta}_n^e &= \frac{1}{\eta_n}(0,-1,1) - (z_n + x_n)\,\underline{\alpha}_n^e, \\
\underline{\gamma}_n^e &= (0,0,1) - z_n^2 \underline{\alpha}_n^e - z_n \underline{\beta}_n^e,
\end{aligned}$$

which are independent of the nodal velocities. The quadratic interpolation given by (8.4) now can be expressed as

$$\mathcal{V} = \left(x^2 \underline{\alpha}_n^e + x \underline{\beta}_n^e + \underline{\gamma}_n^e\right) \cdot \mathbf{v}_n^e.$$

The velocity at the point (x_n, y_{n-1}) is V_C^e and can now be expressed in terms of nodal velocities at grid points in the elastic region of the fault in the $(n-1)^{th}$ column of grid points as

$$V_C^e = \left(x_n^2 \underline{\alpha}_{n-1} + x_n \underline{\beta}_{n-1} + \underline{\gamma}_{n-1}\right) \cdot \mathbf{v}_{n-1},$$

where

$$\mathbf{v}_{n-1}^e = \left(V_{m_{n-1}-2,n-1}, V_{m_{n-1}-1,n-1}, V_{m_{n-1},n-1}\right).$$

Similarly the velocity V_E^e can be expressed as an interpolation down the $(n+1)^{th}$ column of grid points. Thus

$$V_E^e = \left(x_n^2 \underline{\alpha}_{n+1} + x_n \underline{\beta}_{n+1} + \underline{\gamma}_{n+1}\right) \cdot \mathbf{v}_{n+1}^e.$$

Analogous expressions can be derived for V_C^p and V_E^p using the velocities at the points (m_n, n), (m_n+1, n) and (m_n+2, n). The vectors $\underline{\alpha}_n^p$, $\underline{\beta}_n^p$, $\underline{\gamma}_n^p$ and $\mathbf{v}_n^p$ are

defined as

$$\begin{aligned}
\underline{\alpha}_n^p &= \frac{(\delta, \delta - \eta_n, \eta_n - 2\delta)}{\delta\,(\delta - \eta_n)\,(2\delta - \eta_n)}, \\
\underline{\beta}_n^p &= \frac{1}{\delta}\,(0, -1, 1) - (2x_n + 3\delta)\,\underline{\alpha}_n^p, \\
\underline{\gamma}_n^p &= (1, 0, 0) - z_n^2 \underline{\alpha}_n^p - z_n \underline{\beta}_n^p, \\
\mathbf{v}_n^p &= (V(m_n, n), V(m_n + 1, n), V(m_n + 2, n))\,.
\end{aligned}$$

so that the interpolated velocity at a point x is given by

$$\mathcal{V} = \left(x^2 \underline{\alpha}_n^p + x \underline{\beta}_n^p + \underline{\gamma}_n^p\right) \cdot \mathbf{v}_n^p.$$

The velocities V_C^p and V_E^p are then given by

$$\begin{aligned}
V_C^p &= \left((x_n + \delta)^2\,\underline{\alpha}_{n-1}^p + (x_n + \delta)\,\underline{\beta}_{n-1}^p + \underline{\gamma}_{n-1}^p\right) \cdot \mathbf{v}_{n-1}^p, \\
V_E^p &= \left((x_n + \delta)^2\,\underline{\alpha}_{n+1}^p + (x_n + \delta)\,\underline{\beta}_{n+1}^p + \underline{\gamma}_{n+1}^p\right) \cdot \mathbf{v}_{n+1}^p.
\end{aligned}$$

Part of the simplicity of this method is that the interpolation-extrapolation reduces simply to $V_C^e = V(m_j - 1, j - 1)$ and $V_E^e = V(m_j - 1, j + 1)$ in the case where C and E are standard grid points. This eliminates the need to ascertain the position of C and E relative to the elasto-plastic boundary and the one method can be used universally.

8.3 Finite Differencing Points on the Boundary

The finite difference expressions derived at the points directly above and below the boundary, (8.1) and (8.3), require the value of the velocity at points where the boundary crosses each column of grid points. This introduces K_p new grid points and we therefore need K_p more equations for the unknowns to maintain consistency of the system. At the points on the boundary we finite difference the continuity of traction-rate boundary condition. As shall be seen, the application of the continuity of velocity condition across the elasto-plastic boundary is automatically applied through the occurence of the velocity on the boundary, $V(m_n, n)$,

in the finite difference approximations to the governing equations both above and below the boundary, (8.1) and (8.3), as well as in the interpolation discussed in the previous section which is utilised further here.

For a curved line through the $x-y$ plane given by $z(y)$ the tangent vector can be writen as

$$\mathbf{t} = \left(\frac{dz}{dy}, 1\right).$$

A unit normal to this curve is then given by

$$\mathbf{n} = (n_1, n_2) = \left(1, -\frac{dz}{dy}\right)\left(1 + \left(\frac{dz}{dy}\right)^2\right)^{-\frac{1}{2}}.$$

In the current problem, only a discretised analogue of $z(y)$ given by the coordinates (z_n, y_n) is known and so the derivative of z with respect to y can be approximated by the centered finite difference

$$\left.\frac{dz}{dy}\right|_{z=z_n} = \frac{h(z_{n+1} - z_{n-1})}{2w\delta_y}.$$

The continuity of traction-rate boundary condition can be expressed as

$$\begin{aligned} n_1\frac{\partial V^e}{\partial x} + n_2\frac{\partial V^e}{\partial y} &= n_1\left(\Sigma_1\frac{\partial V^p}{\partial x} - \Sigma_2\frac{\partial V^p}{\partial y}\right) + n_2\left(-\Sigma_2\frac{\partial V^p}{\partial x} + \Sigma_3\frac{\partial V^p}{\partial y}\right) \\ &= \left(n_1\Sigma_1 - n_2\Sigma_2\right)\frac{\partial V^p}{\partial x} + \left(-n_1\Sigma_2 + n_2\Sigma_3\right)\frac{\partial V^p}{\partial y}. \end{aligned}$$

At the point (m_n, n) the non-dimensional equation to be satisfied is

$$\begin{aligned} &\frac{wn_1}{h}\left.\frac{\partial V^e}{\partial x}\right|_{m_n,n} + n_2\left.\frac{\partial V^e}{\partial y}\right|_{m_n,n} \\ &= \frac{w}{h}\left(n_1\Sigma_1^{m_n,n} - n_2\Sigma_2^{m_n,n}\right)\left.\frac{\partial V^p}{\partial x}\right|_{m_n,n} + \left(-n_1\Sigma_2^{m_n,n} + n_2\Sigma_3^{m_n,n}\right)\left.\frac{\partial V^p}{\partial y}\right|_{m_n,n} \end{aligned} \quad (8.10)$$

Assuming the elasto-plastic boundary is sufficiently far removed from the upper and lower boundaries the x derivatives can be replaced by one-sided differences on

irregular grids. The y derivatives are approximated by centered differences using the velocities at the points (z_n, y_{n-1}) and (z_n, y_{n+1}). Since the new boundary grid points do not lie within the regular grid spacing framework of the mesh there will not, in general, be a grid point in neighbouring columns with the same x coordinate. Such a situation is shown in Figure 8.4. The y derivative at E uses the velocity at the two points shown by the circles which represent the points (z_n, y_{n-1}) and (z_n, y_{n+1}). Using the same interpolation method described in the previous section expressions for these velocities can be approximated. For the point on the right, the interpolation method is used to express the required velocity in terms of the velocity at D, F and G. In the example, the point on the left is not only not on a grid point but is also outside the plastic region. The velocity at A, B and C are then used to extrapolate along the green dashed line to approximate the velocity where necessary.

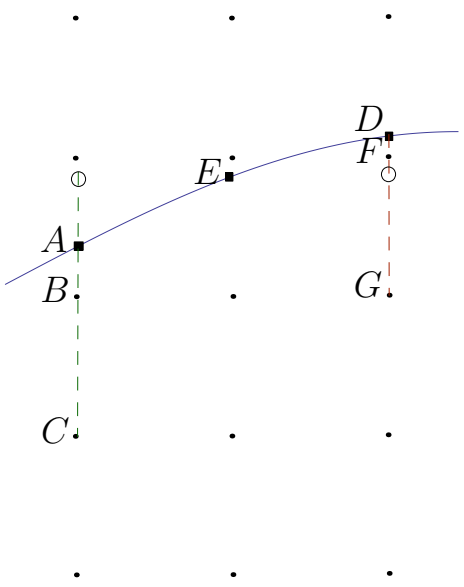

Figure 8.4: A representative section of the boundary with labelled points included in the finite difference approximation to the y derivative at a point E on the boundary. The values of the velocity at A, B and C are used to extrapolate along the green dashed line to approximate V at the left circular dot. Interpolation is carried out along the red dashed line to approximate the velocity at the right circular dot using the value of V at D, F and G.

The velocities at the points (z_n, y_{n-1}) and (z_n, y_{n-1}) are denoted V_l and V_r

respectively and receive a superposed e or p to denote whether they are being used in a derivative above or below the elasto-plastic boundary. The finite difference equation applied at the points on the boundary is

$$\begin{aligned} & n_2\left(\frac{V_r^e - V_l^e}{2\delta_y}\right) + \left(n_1\Sigma_2^{m_n,n} - n_2\Sigma_3^{m_n,n}\right)\left(\frac{V_r^p - V_l^p}{2\delta_y}\right) - \frac{w}{h}\left(n_1\Sigma_1^{m_n,n} - n_2\Sigma_2^{m_n,n}\right) \\ & \times\left(\frac{\delta\left(2\eta_n - 3\delta\right)V_{m_n,n} + \left(2\delta - \eta_n\right)^2 V_{m_n+1,n} - \left(\delta - \eta_n\right)^2 V_{m_n+2,n}}{\delta\left(\delta - \eta_n\right)\left(2\delta - \eta_n\right)}\right) \\ & \frac{wn_1}{h}\left(\frac{\delta\left(\delta + 2\eta_n\right)V_{m_n,n} - \left(\delta + \eta_n\right)^2 V_{m_n-1,n} + \eta_n^2 V_{m_n-2,n}}{\delta\eta_n\left(\delta + \eta_n\right)}\right) = 0, \end{aligned} \tag{8.11}$$

where

$$\begin{aligned} V_l^e &= \left(z_n^2\underline{\alpha}_{n-1}^e + z_n\underline{\beta}_{n-1}^e + \underline{\gamma}_{n-1}^e\right)\cdot\mathbf{v}_{n-1}^e, \\ V_r^e &= \left(z_n^2\underline{\alpha}_{n+1}^e + z_n\underline{\beta}_{n+1}^e + \underline{\gamma}_{n+1}^e\right)\cdot\mathbf{v}_{n+1}^e, \\ V_l^p &= \left(z_n^2\underline{\alpha}_{n-1}^p + z_n\underline{\beta}_{n-1}^p + \underline{\gamma}_{n-1}^p\right)\cdot\mathbf{v}_{n-1}^p, \\ V_r^p &= \left(z_n^2\underline{\alpha}_{n+1}^p + z_n\underline{\beta}_{n+1}^p + \underline{\gamma}_{n+1}^p\right)\cdot\mathbf{v}_{n+1}^p. \end{aligned}$$

At the end point where the elasto-plastic boundary meets the edge of the fault the expression analogous to (8.11) has backwards differences for the y derivatives and the velocities interpolated down the $K_p - 1$ and $K_p - 2$ columns of grid points.

8.4 Convergence of the Numerical Scheme

The finite difference scheme desribed in Chapter 7 has been derived using only second order accurate finite differences and so converges quadratically in the grid spacings δ_x, δ_y and ϵ_y. The purpose of this section is to show that the addition of the interpolation-extrapolation method applied to the finite difference scheme can be used to simply and efficiently model a range of curved boundaries while maintaining the second order accurate nature of the finite difference approximations.

We solve the finite difference scheme presented in the current and previous chapter for a model case where the fault and tectonic plate are both unit squares,

namely when $w = h = 1$ and $L = 2$. The basal traction-rate takes the form of $\mathcal{G}(y) = \sigma_b \tanh(4y)$ where $\sigma_b = 0.005$. The elasto-plastic boundary is a specified curve separating two elastic regions above and below. The convergence rates are calculated for curved boundaries of the form $z = \frac{1}{2} + A\cos(2\pi y)$ with the amplitude taking the values $A = \pm\frac{1}{20}, \pm\frac{1}{12}, \pm\frac{1}{8}, \pm\frac{1}{6}$ and compared with the known second order accurate scheme with a horizontal boundary. We define the same grid spacing in both the vertical and horizontal directions so that we can check the convergence of the system against just one parameter, K_p say. As K_p increases the mesh simultaneously refines everywhere at the same rate.

The numerical results are compared to the analytic solution derived in Chapter 6 and the errors in the numerical results calculated. We neglect the point (h, w) from the convergence check since the analytic solution is zero here due to its Fourier series expansions of $\mathcal{G}$ and G. Two different methods for checking the convergence are employed; the first simply calculates the maximum absolute error across the domain

$$E_{max}(K_p) = \max(|V - V_{an}|), \tag{8.12}$$

and the second investigates the ratio of the L^2 norm of the errors and the L^2 norm of the analytic solution, V_{an},

$$E_2(K_p) = \frac{||V - V_{an}||^2}{||V_{an}||^2}. \tag{8.13}$$

A comparison of these error measures is shown in Figure 8.5 with K_p ranging from 32 to 64. For all values of A and K_p the E_{max} error is larger than the E_2 error which is inevitable from its definition. The rate of convergence of the two error measures is, however, almost indistinguishable and verifies that at every point the nodal velocities of the numerical solution are converging on the analytic solution at the same rate as the overall system. For small amplitude of the curved boundary the sign of A makes little difference to either measures of the error, Figure 8.5a). For larger values of $|A|$ the effect of the sign of A has a more pronounced, though still minor, impact on the size of the errors but not the convergence rate, Figure 8.5d).

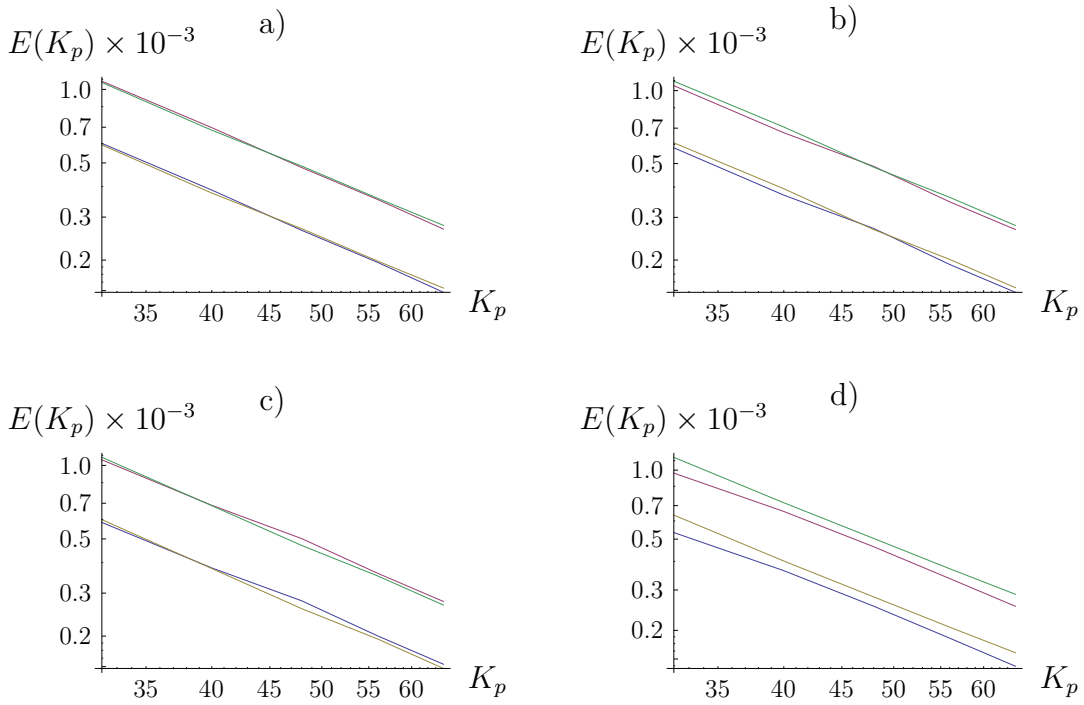

Figure 8.5: Convergence of the finite difference scheme for different shaped boundaries on a log-log plot. The red and green lines correspond to the maximum absolute value error, (8.12), and the blue and yellow show the convergence with the 2-norm given by (8.13). Plots a)- d) correspond to the values of $|A| = \frac{1}{20}, \frac{1}{12}, \frac{1}{8}, \frac{1}{6}$ respectively. Negative values of A are given by the blue and red lines and the yellow and green are positive values.

Figure 8.6 shows the rate of convergence of the E_2 norm for negative and positive values of A compared against that for a horizontal boundary, shown by the dashed line, for which the numerical scheme is known to converge quadratically. As can be seen, the errors decrease at the same rate for all shaped boundaries albeit with fractionally higher values of the errors than is obtained from a horizontal boundary. The values of the convergence rates given by

$$\frac{\log(E(64)) - \log(E(32))}{\log(64) - \log(32)},$$

are shown in Table 8.1 for all the boundaries considered. As can be seen the convergence rates are all comparable for both error measures and all shapes of boundary. A convergence rate of around -2 is required for quadratic convergence

and the scheme with a horizontal boundary gives rates of -1.9808 and -1.9710 for the E_2 and E_{max} errors respectively. The values for other shaped boundaries are comparable and we can conclude that the interpolation-extrapolation method does not alter the convergence of the numerical scheme. The maximum and minimum convergence rates are -2.0256 and -1.9259 which are obtained for $A = -\frac{1}{20}$ and $\frac{1}{8}$, respectively. It is a little unexpected that a slightly curved boundary with $A = -\frac{1}{20}$ gives a quicker convergence rate than a horizontal boundary, however, this is most probably due to the imperfectly straight nature of the convergence plots in Figure 8.5. The convergence rate is determined by the grid spacings and as the amplitude, A, of the boundary changes the grid spacing of the irregular mesh will change, this accounts for the small oscillations in the plots in Figure 8.5. These small variations in the errors are accountable for the unusual fluctuations in the convergence rates in Table 8.1.

Table 8.1: Convergence rates for the numerical scheme for a range of curved boundaries.

A	0	$-\frac{1}{20}$	$\frac{1}{20}$	$-\frac{1}{12}$	$\frac{1}{12}$
E_2	-1.9809	-2.0256	-1.9470	-1.9805	-1.9860
E_{max}	-1.9710	-2.0119	-1.9433	-1.9717	-1.9778
A	$-\frac{1}{8}$	$-\frac{1}{8}$	$-\frac{1}{6}$	$\frac{1}{6}$	
E_2	-1.9284	-2.0239	-1.9370	-1.9951	
E_{max}	-1.9259	-2.0095	-1.9306	-1.9853	

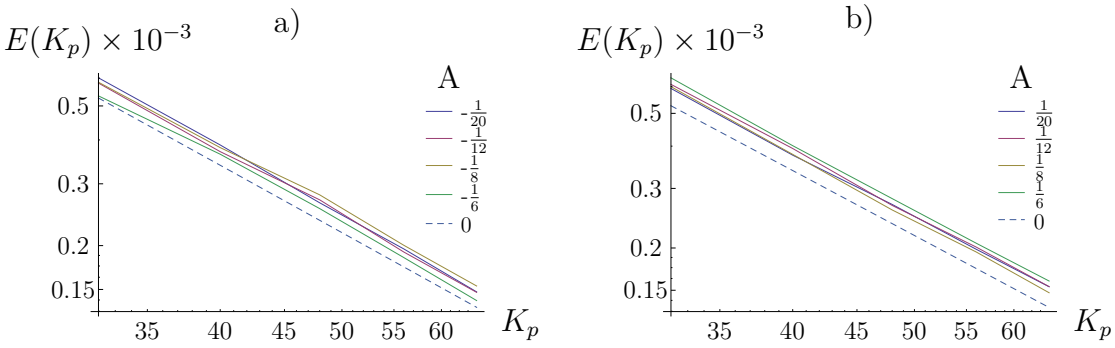

Figure 8.6: Convergence of the numerical scheme under the $E_n(K_p)$ error measure for different shaped boundaries on log-log plots. The dashed line shows the convergence of the numerical scheme for a horizontal boundary without the interpolation-extrapolation method.

Chapter 9

Corner Stress Singularities

9.1 Motivation

When the lower section of the fault reaches yield there is a different definition of $\dot{\sigma}_{13}$ at either side of $y = w$ near $x = h$. Straight forward finite differences struggles to resolve the solution near this corner without intensive mesh refinement. Despite specifying a value of $\dot{\sigma}_{13}$ along $x = h$, the finite difference equations are inconsistent and are unable to be all solved simultaneously. The outcome is that differentiating the computed velocity field is not sufficiently accurate so as to produce the correct stress-rate along the lower edge of the domain. This can be seen in Fig 9.1 and Fig 9.2. In both figures the dashed line represents the chosen value of $\mathcal{G}$ along $x = h$ and the other lines represent numerically calculated stress-rate divided by μ. The break in the line indicates the edge of the boundary at $y = w$ with the fault material to the left and the tectonic plate to the right. In Fig 9.1 the numerically computed value differs from the desired value for the 4 or 5 points nearest to corner, out to a distance of about 15-20m from the fault boundary. Even after the grid spacing is halved in Fig 9.2 the discrepency affects a region of the same width but this region now encompasses twice as many points.

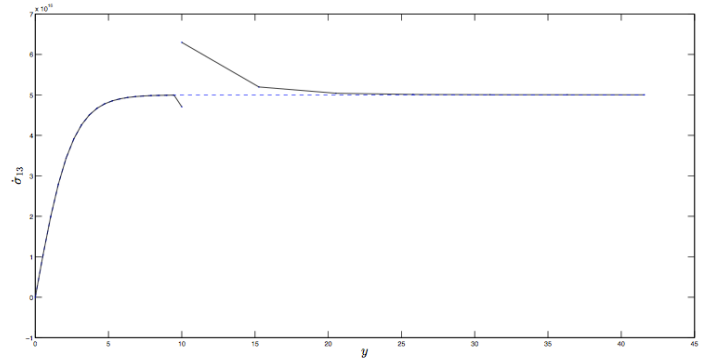

Figure 9.1: Inputted value of basal traction rate compared to the computed value.

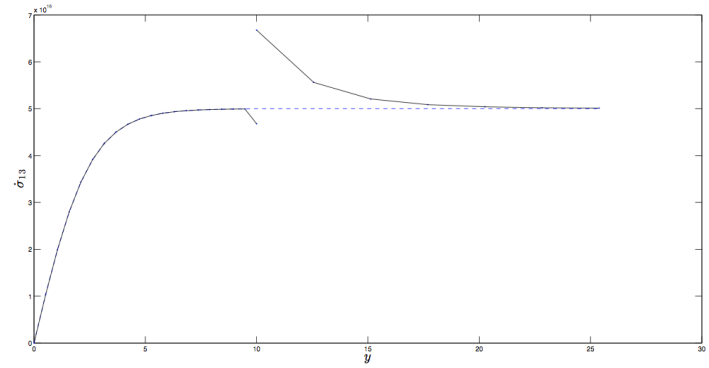

Figure 9.2: Inputted value of basal traction rate compared to the computed value with a refined mesh in the tectonic plate.

The cause of this descrepency is that the solution is varying too rapidly in the vicinity of the corner to be picked up by the grid spacing, even with a refined mesh and further mesh refinement would take too long to compute. To resolve

this problem we find an asymptotic solution near the corner which can suitably encapsulate the nature of the solution.

In addition, the point where the elasto-plastic boundary meets the edge of the fault causes inconsistencies in the finite difference equations. The boundary condition which equates the stress-rate, $\dot{\sigma}_{23}$, across the boundary $y = w$ cannot be satisfied by a practical grid spacing. Figure 9.3 shows the stress-rate on either side of $y = w$. The red curve is $\dot{\sigma}_{23}$ on the edge of the fault and the blue curve is the stress-rate on the edge of the tectonic plate. As can be seen the two are identical except at the grid points in the vicinity of the elasto-plastic boundary which lies where $\dot{\sigma}_{23}$ reaches its minimum value of $-1\ kbar\ yr^{-1}$.

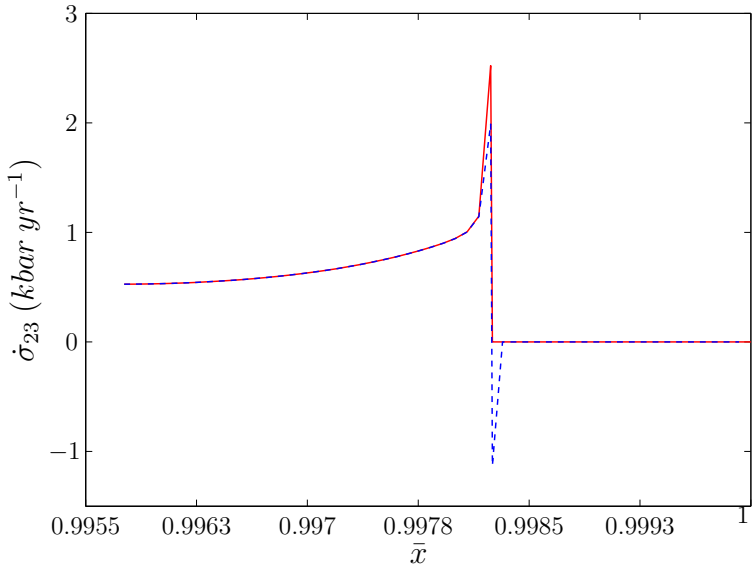

Figure 9.3: The stress-rate, $\dot{\sigma}_{23}$ either side of $y = w$. The red line shows the stress-rate at the edge of the fault and the blue line is $\dot{\sigma}_{23}$ on the edge of the tectonic plate. The elasto-plastic boundary meets $y = w$ at the point where the stress-rate reaches a minimum value.

There is very little in the literature on stress singularities in plasticity. The phenomena is mentioned in problem of two elastic regions joined by a plastic adhesive Jancar et al. [1993] and Reedy and Guess [1993] but little is done other than calculating the stress singularities to derive a criterion at which the joint fails and cracks form. The study of crack propagation is a research topic in its own right, see for example Hutchinson [1968] and Rice and Rosengren [1968], in which

an elastic strain energy density function is used to find the stress singularities. The latter reference holds most similarity with the method employed in this chapter in that they solve a set of plastic constitutive equations near the crack tip. The author, however, is unable to rigorously calculate the order of the singularity unlike the current work.

Stress singularities also occur in fluid dynamics problems and these are far more widely studied. We additionally consult this literature to apply their theory tothe current problem. Hocking [1977], for example, studies the stress singularity that occurs at the corner of a moving rigid boundary against a flate plate. The stress singularity is found to be of order $O(r^{-1})$ obtained using a similarity solution. Floryan and Czechowski [1995] study flow around an external corner and five different finite difference methods are employed to resolve the singular vorticity field at the corner. The order $O(r^{-0.4555163})$ singularity is included into a standard regular mesh finite difference scheme in all five methods and each gives a different value for the coefficient of the singular term. The same problem is considered by Hawa and Rusak [2002] but they use a mesh refinement near the corner and assume the asymptotic singular solution holds in the vicinity of the corner. The outer numerical solution is then matched to the asymptotic solution along a contour surrounding the corner and a least square method employed to calculate the unknown coefficients in the asymptotic expansion. An extension to this method to include a matching region rather than a contour is carried out by Shi et al. [2004].

To resolve the corner singularities in this work the variables are expanded asymptotically about their corner values and the governing equations are linearised. By making a change of coordinates the governing plasticity equations reduce to Laplace's equation which is solved using the method given in Li and Lu [2000]. Due to the non-constant coefficients in the full governing equation we do not assume that the resulting asymptotic expansion holds near the corner, instead the singular terms are subtracted off the full solution and the resulting regular velocity is solved for using a standard finite difference scheme.

9.2 Singularities Arising at the Point at the Base of the the Boundary of the Fault.

We seek a locally asymptotic solution near the corner at (h, w). Define the local inner coordinates (X, Y) such that $x = h + \epsilon X$ and $y = w + \epsilon Y$. Suppose the velocity and stresses take the form of the asymptotic expansions

$$\begin{aligned} V^p &= V_0 + \epsilon \nu^p(X, Y) + O(\epsilon^2), \\ V^e &= V_0 + \epsilon \nu^e(X, Y) + O(\epsilon^2), \\ \sigma_{i3} &= \bar{\sigma}_{i3} + \epsilon \sigma^*_{i3}(X, Y) + O(\epsilon^2), \end{aligned} \tag{9.1}$$

where V_0 and $\bar{\sigma}_{i3}$ are the leading order behaviours at the corner. Subsequently, it follows that $H = \bar{H} + O(\epsilon)$, $f_{i3} = \bar{f}_{i3} + O(\epsilon)$ and $\Sigma_i = \bar{\Sigma}_i + \epsilon \Sigma^*_i(X, Y) + O(\epsilon^2)$ where $\bar{H}$, $\bar{f}_{i3}$ and $\bar{\Sigma}_i$ are the values that H, f_{i3} and Σ_i take when $\epsilon = 0$ in (9.1). In the local coordinates the first derivatives transform to

$$\begin{aligned} \frac{\partial}{\partial x} &= \frac{dX}{dx}\frac{\partial}{\partial X} = \frac{1}{\epsilon}\frac{\partial}{\partial X}, \\ \frac{\partial}{\partial y} &= \frac{dY}{dy}\frac{\partial}{\partial Y} = \frac{1}{\epsilon}\frac{\partial}{\partial Y}, \end{aligned} \tag{9.2}$$

and the second derivatives become

$$\begin{aligned} \frac{\partial^2}{\partial x^2} &= \frac{1}{\epsilon^2}\frac{\partial^2}{\partial X^2}, \\ \frac{\partial^2}{\partial y^2} &= \frac{1}{\epsilon^2}\frac{\partial^2}{\partial Y^2}. \end{aligned} \tag{9.3}$$

Substituting the asymptotic expansions (9.1) and the transformed local derivatives, (9.3), into Laplace's equation results in the leading order equation

$$\frac{\partial^2 \nu^e}{\partial X^2} + \frac{\partial^2 \nu^e}{\partial Y^2} = 0. \tag{9.4}$$

Similarly, with the aid of the transformed first derivatives (9.2) the second order plasticity equation, (5.37), for the velocity becomes

$$\bar{\Sigma}_1\frac{\partial^2\nu^p}{\partial X^2}+\bar{\Sigma}_3\frac{\partial^2\nu^p}{\partial Y^2}-2\bar{\Sigma}_2\frac{\partial^2\nu^p}{\partial X\partial Y}$$
$$+\epsilon\left[\frac{\partial\Sigma_1^*}{\partial X}-\frac{\partial\Sigma_2^*}{\partial Y}\right]\frac{\partial\nu^p}{\partial X}+\epsilon\left[-\frac{\partial\Sigma_2^*}{\partial X}+\frac{\partial\Sigma_3^*}{\partial Y}\right]\frac{\partial\nu^p}{\partial Y}=0,$$

which to leading order is

$$\bar{\Sigma}_1\frac{\partial^2\nu^p}{\partial X^2}+\bar{\Sigma}_3\frac{\partial^2\nu^p}{\partial Y^2}-2\bar{\Sigma}_2\frac{\partial^2\nu^p}{\partial X\partial Y}=0. \tag{9.5}$$

The boundary condition on $X=0$ in the elastic region is expressed as

$$\mu\frac{\partial\nu^e}{\partial X}\bigg|_{X=0}=g_0+O(\epsilon),$$

which to leading order is

$$\mu\frac{\partial\nu^e}{\partial X}\bigg|_{X=0}=g_0. \tag{9.6}$$

Here g_0 is the value of the basal traction rate at $(x,y)=(h,w)$ or equivalently $(X,Y)=(0,0)$. Also the traction rate on $Y=0$ can be expressed as

$$\dot{\sigma}_{23}^e(X,0)=\mu\frac{\partial\nu^e}{\partial Y}\bigg|_{Y=0}+O(\epsilon). \tag{9.7}$$

On the base of the plastic region, the leading order behaviour of the boundary condition is

$$\mu\bar{\Sigma}_1\frac{\partial\nu^p}{\partial X}\bigg|_{X=0}-\mu\bar{\Sigma}_2\frac{\partial\nu^p}{\partial Y}\bigg|_{X=0}=g_0, \tag{9.8}$$

and the traction rate on $Y=0$ is

$$\dot{\sigma}_{23}^p(X,0)=-\mu\bar{\Sigma}_2\frac{\partial\nu^p}{\partial X}\bigg|_{Y=0}+\mu\bar{\Sigma}_3\frac{\partial\nu^p}{\partial Y}\bigg|_{Y=0}+O(\epsilon). \tag{9.9}$$

Equating the leading order terms in the traction rate on $Y = 0$ from (9.7) and (9.9) gives the condition

$$\left.\frac{\partial \nu^e}{\partial Y}\right|_{Y=0} = -\bar{\Sigma}_2 \left.\frac{\partial \nu^p}{\partial X}\right|_{Y=0} + \bar{\Sigma}_3 \left.\frac{\partial \nu^p}{\partial Y}\right|_{Y=0}. \tag{9.10}$$

Finally, continuity of velocity across $Y = 0$ simply becomes

$$\nu^e(X, 0) = \nu^p(X, 0), \tag{9.11}$$

to leading order.

The leading order plasticity equation (9.5) is now a constant coefficient partial differential equation but is still complicated by the presence of the mixed derivative. To eliminate this complexity consider the change of coordinates

$$\begin{aligned} \xi &= \alpha X, \\ \eta &= \beta X + \gamma Y. \end{aligned} \tag{9.12}$$

Relative to these new coordinates the first X and Y derivatives are

$$\begin{aligned} \frac{\partial}{\partial X} &= \alpha \frac{\partial}{\partial \xi} + \beta \frac{\partial}{\partial \eta}, \\ \frac{\partial}{\partial Y} &= \gamma \frac{\partial}{\partial \eta}, \end{aligned} \tag{9.13}$$

and the second derivatives are

$$\begin{aligned} \frac{\partial^2}{\partial X^2} &= \alpha^2 \frac{\partial^2}{\partial \xi^2} + 2\alpha\beta \frac{\partial^2}{\partial \xi \partial \eta} + \beta^2 \frac{\partial^2}{\partial \eta^2}, \\ \frac{\partial^2}{\partial Y^2} &= \gamma^2 \frac{\partial^2}{\partial \eta^2}, \\ \frac{\partial^2}{\partial X \partial Y} &= \alpha\gamma \frac{\partial^2}{\partial \xi \partial \eta} + \beta\gamma \frac{\partial^2}{\partial \eta^2}. \end{aligned} \tag{9.14}$$

The leading order plasticity equation then becomes

$$\alpha^2 \bar{\Sigma}_1 \frac{\partial^2 \nu^p}{\partial \xi^2} + (2\alpha\beta\bar{\Sigma}_1 - 2\alpha\gamma\bar{\Sigma}_2) \frac{\partial^2 \nu^p}{\partial \xi \partial \eta} + (\beta^2 \bar{\Sigma}_1 + \gamma^2 \bar{\Sigma}_3 - 2\beta\gamma\bar{\Sigma}_2) \frac{\partial^2 \nu^p}{\partial \eta^2} = 0.$$

By choosing appropriate choices for α, β and γ it is possible to reduce this to Laplace's equation in terms of ξ and η. Setting the coefficient of the mixed derivative to zero requires $\beta\bar{\Sigma}_1 = \bar{\Sigma}_2\gamma$. Substituting this into the coefficients of the two second derivatives with respect to ξ ad η and equating yields $\alpha^2\bar{\Sigma}_1^2 = \gamma^2\left(\bar{\Sigma}_1\bar{\Sigma}_3 - \bar{\Sigma}_2^2\right)$. We chose $\alpha = \sqrt{\bar{\Sigma}_1\bar{\Sigma}_3 - \bar{\Sigma}_2^2}$ and $\gamma = \bar{\Sigma}_1$ which in turn gives $\beta = \bar{\Sigma}_2$.

Hence the change of coordinates (9.12) becomes

$$\begin{aligned} \xi &= X\sqrt{\bar{\Sigma}_1\bar{\Sigma}_3 - \bar{\Sigma}_2^2}, \\ \eta &= \bar{\Sigma}_2 X + \bar{\Sigma}_1 Y, \end{aligned} \tag{9.15}$$

and in these coordinates equation (9.5) reduces to Laplace's equation

$$\frac{\partial^2 \nu^p}{\partial \xi^2} + \frac{\partial^2 \nu^p}{\partial \eta^2} = 0. \tag{9.16}$$

We now wish to perform another change of coordinates into cylindrical polar coordinates using the definitions

$$\begin{aligned} r = \sqrt{X^2 + Y^2}, \qquad & \tan\theta = \frac{Y}{X}, \\ \rho = \sqrt{\xi^2 + \eta^2}, \qquad & \tan\phi = \frac{\eta}{\xi}. \end{aligned} \tag{9.17}$$

We choose $\theta \in [0, 2\pi)$ and $\phi \in [-\pi, \pi)$ because this ensures that θ and ϕ are continuous in the elastic and plastic regions respectively. The coordinates (r, θ) are the usual polar coordinates with r the distance from the origin and θ measuring the angle from the positive X axis in the anticlockwise direction. Relative to (ξ, η), the coordinates (ρ, ϕ) have analogous definitions, but they have rather more complicated relations to (X, Y). Firstly, the angle ϕ is measured anticlockwise from the line defined by $\phi = 0$. Using the change of variables (9.15) in the definition of ϕ gives

$$\tan\phi = \frac{\bar{\Sigma}_1}{\sqrt{\bar{\Sigma}_1\bar{\Sigma}_3 - \bar{\Sigma}_2^2}}\frac{Y}{X} + \frac{\bar{\Sigma}_2}{\sqrt{\bar{\Sigma}_1\bar{\Sigma}_3 - \bar{\Sigma}_2^2}}. \tag{9.18}$$

Hence the radial line $\phi = 0$ is the line defined by

$$Y = -\frac{\bar{\Sigma}_2}{\bar{\Sigma}_1} X.$$

The X axis is given by $Y = 0$ which, using (9.18), occurs when

$$\tan\phi|_{Y=0} = \frac{\bar{\Sigma}_2}{\sqrt{\bar{\Sigma}_1\bar{\Sigma}_3 - \bar{\Sigma}_2^2}}.$$

Define Φ to be the value of ϕ along the positive X axis so that

$$\tan\Phi = \frac{\bar{\Sigma}_2}{\sqrt{\bar{\Sigma}_1\bar{\Sigma}_3 - \bar{\Sigma}_2^2}}. \tag{9.19}$$

The value of $\bar{\Sigma}_2$ is positive and so the fundamental value of Φ will lie in the region $\left[0, \frac{\pi}{2}\right)$ and so the line $\phi = 0$ lies in the third quadrant relative to X and Y. The negative X axis is given by $\phi = \Phi - \pi$. The positive Y axis is defined by $X = 0$ and this corresponds to $\phi = \frac{\pi}{2}$. Likewise, the negative Y axis is given by $\phi = -\frac{\pi}{2}$. This geometry is shown in Figure 9.4.

In the two sets of polar coordinates (9.17), Laplace's equation becomes

$$\frac{\partial^2\nu^e}{\partial r^2} + \frac{1}{r}\frac{\partial\nu^e}{\partial r} + \frac{1}{r^2}\frac{\partial^2\nu^e}{\partial\theta^2} = 0, \tag{9.20}$$

and

$$\frac{\partial^2\nu^p}{\partial\rho^2} + \frac{1}{\rho}\frac{\partial\nu^p}{\partial\rho} + \frac{1}{\rho^2}\frac{\partial^2\nu^p}{\partial\phi^2} = 0. \tag{9.21}$$

The chain rule expresses the X and Y derivatives in the elastic region as

$$\begin{aligned} \frac{\partial}{\partial X} &= \cos\theta\frac{\partial}{\partial r} - \frac{\sin\theta}{r}\frac{\partial}{\partial\theta}, \\ \frac{\partial}{\partial Y} &= \sin\theta\frac{\partial}{\partial r} + \frac{\cos\theta}{r}\frac{\partial}{\partial\theta}, \end{aligned}$$

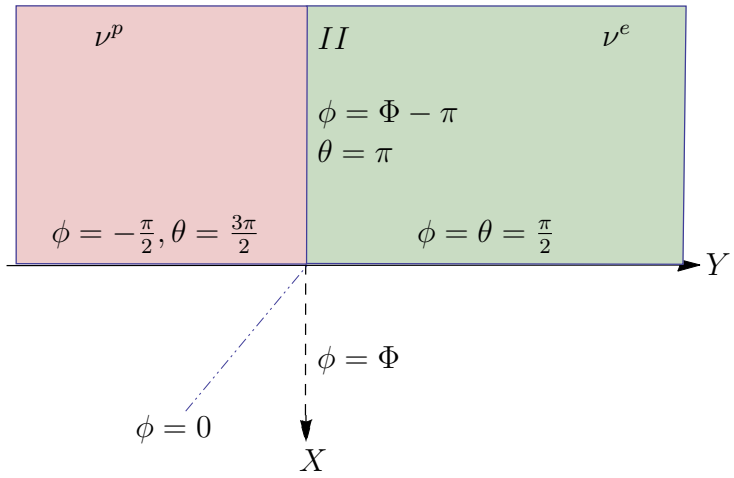

Figure 9.4: Local geometry near the corner at the base of the edge of the fault. The elastic behaving region is shaded green and the red region is the region of fault material in yield. The velocity perturbations are ν^e and ν^p in the respective regions. The coordinates X and Y radiant from the corner vertically downwards and horizontally. The boundary between the two regions is denoted II. The polar angle θ is measured anticlockwise from the positive X axis. The elliptical polar angle ϕ is measured anticlockwise and takes the value Φ on the positive X axis and $\Phi - \pi$ on II. The line $\phi = 0$ is shown by the dashed and dotted line.

which change the boundary condition (9.6) into

$$-\frac{1}{r}\frac{\partial \nu^e}{\partial \theta}\bigg|_{\theta=\frac{\pi}{2}} = \frac{g_0}{\mu}. \tag{9.22}$$

Similarly, the boundary condition on $X = 0$ in the plastic region (9.8) can be expressed in terms of the polar coordinates (9.17) with the use of (9.13) and (9.15) as

$$\begin{aligned} \frac{g_0}{\mu} &= \bar{\Sigma}_1 \frac{\partial \nu^p}{\partial X}\bigg|_{X=0} - \bar{\Sigma}_2 \frac{\partial \nu^p}{\partial Y}\bigg|_{X=0} \\ &= \bar{\Sigma}_1 \sqrt{\bar{\Sigma}_1 \bar{\Sigma}_3 - \bar{\Sigma}_2^2} \frac{\partial \nu^p}{\partial \xi}\bigg|_{\xi=0} \\ &= \frac{\bar{\Sigma}_1 \sqrt{\bar{\Sigma}_1 \bar{\Sigma}_3 - \bar{\Sigma}_2^2}}{\rho} \frac{\partial \nu^p}{\partial \phi}\bigg|_{\phi=-\frac{\pi}{2}}. \end{aligned} \tag{9.23}$$

On $Y = 0$, the value of ρ can be expressed in terms of r as

$$\rho = r\sqrt{\bar{\Sigma}_1\bar{\Sigma}_3}, \tag{9.24}$$

and the coefficient $\sqrt{\bar{\Sigma}_1\bar{\Sigma}_3}$ labelled by ρ_I so that $\rho = \rho_I r$. Continuity of velocity on $Y = 0$, (9.11), now becomes

$$\nu^e(r, \pi) = \nu^p(\rho_I r, \Phi - \pi), \tag{9.25}$$

and finally, continuity of traction rate (9.10) on $Y = 0$ becomes

$$\begin{aligned}
-\frac{1}{r}\frac{\partial \nu^e}{\partial \theta}\bigg|_{\theta=\pi} &= -\bar{\Sigma}_2\sqrt{\bar{\Sigma}_1\bar{\Sigma}_3 - \bar{\Sigma}_2^2}\frac{\partial \nu^p}{\partial \xi}\bigg|_{Y=0} + \left(\bar{\Sigma}_1\bar{\Sigma}_3 - \bar{\Sigma}_2^2\right)\frac{\partial \nu^p}{\partial \eta}\bigg|_{Y=0} \\
&= \left[-\bar{\Sigma}_2\sqrt{\bar{\Sigma}_1\bar{\Sigma}_3 - \bar{\Sigma}_2^2}\cos\phi + \left(\bar{\Sigma}_1\bar{\Sigma}_3 - \bar{\Sigma}_2^2\right)\sin\phi\right]\frac{\partial \nu^p}{\partial \rho}\bigg|_{\Phi-\pi} \\
&\quad + \frac{1}{\rho}\left[\bar{\Sigma}_2\sqrt{\bar{\Sigma}_1\bar{\Sigma}_3 - \bar{\Sigma}_2^2}\sin\phi + \left(\bar{\Sigma}_1\bar{\Sigma}_3 - \bar{\Sigma}_2^2\right)\cos\phi\right]\frac{\partial \nu^p}{\partial \phi}\bigg|_{\Phi-\pi}.
\end{aligned}$$

Using the identities

$$\begin{aligned}
\cos(\Phi - \pi) &= -\cos\Phi, \\
\sin(\Phi - \pi) &= -\sin\Phi,
\end{aligned} \tag{9.26}$$

this may be factorised to

$$\begin{aligned}
-\frac{1}{r}\frac{\partial \nu^e}{\partial \theta}\bigg|_{\theta=\pi} &= -\left(\bar{\Sigma}_1\bar{\Sigma}_3 - \bar{\Sigma}_2^2\right)\cos\Phi\left[\tan\Phi - \frac{\bar{\Sigma}_2}{\sqrt{\bar{\Sigma}_1\bar{\Sigma}_3 - \bar{\Sigma}_2^2}}\right]\frac{\partial \nu^p}{\partial \rho}\bigg|_{\Phi-\pi} \\
&\quad - \frac{1}{\rho}\left(\bar{\Sigma}_1\bar{\Sigma}_3 - \bar{\Sigma}_2^2\right)\cos\Phi\left[\frac{\bar{\Sigma}_2\tan\Phi}{\sqrt{\bar{\Sigma}_1\bar{\Sigma}_3 - \bar{\Sigma}_2^2}} + 1\right]\frac{\partial \nu^p}{\partial \phi}\bigg|_{\Phi-\pi}.
\end{aligned}$$

The definition of Φ given by (9.19) reduces this further to give

$$\frac{1}{r}\frac{\partial \nu^e}{\partial \theta}\bigg|_{\theta=\pi} = \frac{1}{\rho}\frac{\bar{\Sigma}_1\bar{\Sigma}_3 - \bar{\Sigma}_2^2}{\cos\Phi}\frac{\partial \nu^p}{\partial \phi}\bigg|_{\Phi-\pi}. \tag{9.27}$$

Laplace's equation in polar coordinates (9.20) and (9.21) can be solved using separation of variables to give the two power series expansions

$$\begin{aligned}\nu^e &= A_0 + B_0\theta + \sum_{m=1}^{\infty} r^{\gamma_m}(A_m \cos\gamma_m\theta + B_m \sin\gamma_m\theta),\\ \nu^p &= a_0 + b_0\phi + \sum_{m=1}^{\infty} \rho^{\alpha_m}(a_m \cos\alpha_m\phi + b_m \sin\alpha_m\phi).\end{aligned}$$

The eigenvalues γ_m and α_m are taken to be positive to ensure that the velocity remains finite at the origin of the polar coordinate systems and are labelled such that $\gamma_1 < \gamma_2 < \gamma_3 < ...$ and $\alpha_1 < \alpha_2 < \alpha_3 < ....$ To ensure the velocity is continuous at the corner we can set $B_0 = b_0 = 0$ and without loss of generality the constants A_0 and α_0 can be incorporated into the base state variable V_0. The perturbations to the velocity field are then expressed as

$$\nu^e = \sum_{m=1}^{\infty} r^{\gamma_m}(A_m \cos\gamma_m\theta + B_m \sin\gamma_m\theta), \tag{9.28}$$

$$\nu^p = \sum_{m=1}^{\infty} \rho^{\alpha_m}(a_m \cos\alpha_m\phi + b_m \sin\alpha_m\phi). \tag{9.29}$$

Substituting the velocity in the elastic region (9.28) into the boundary condition (9.22) yields

$$-\frac{1}{r}\frac{\partial \nu^e}{\partial\theta}\bigg|_{\theta=\frac{\pi}{2}} = \sum_{m=1}^{\infty} Y^{\gamma_m - 1}\gamma_m \left(A_m \sin\frac{\gamma_m\pi}{2} - B_m \cos\gamma_m\frac{\gamma_m\pi}{2}\right) = \frac{g_0}{\mu}.$$

The coefficients of the powers of Y must match on either side of the second equality sign. This requires $\gamma_k = 1$ for some k. After a suitable relabelling of the γ_m this expression may be written

$$A_1 + \sum_{m=2}^{\infty} Y^{\gamma_m - 1}\gamma_m \left(A_m \sin\frac{\gamma_m\pi}{2} - B_m \cos\frac{\gamma_m\pi}{2}\right) = \frac{g_0}{\mu},$$

where A_1 is the value of the term corresponding to the eigenvalue 1. Then $A_1 = \frac{g_0}{\mu}$

and all the other coefficients A_m and B_m are such that

$$A_m \sin\frac{\gamma_m\pi}{2} - B_m \cos\frac{\gamma_m\pi}{2} = 0.$$

Define

$$C_m = \frac{A_m}{\cos\frac{\gamma_m\pi}{2}},$$

so that the velocity (9.28) can be written as

$$\nu^e = r\left(\frac{g_0}{\mu}\cos\theta + B_1\sin\theta\right) + \sum_{m=2}^{\infty} r^{\gamma_m} C_m \cos\left(\gamma_m\left(\theta - \frac{\pi}{2}\right)\right). \quad (9.30)$$

Similarly, the velocity in the plastic region (9.29) can be substituted into the boundary condition (9.23)

$$\bar{\Sigma}_1\sqrt{\bar{\Sigma}_1\bar{\Sigma}_3 - \bar{\Sigma}_2^2}\sum_{m=2}^{\infty}\rho^{\alpha_m-1}\alpha_m\left(-a_m\sin\frac{3\alpha_m\pi}{2} + b_m\cos\frac{3\alpha_m\pi}{2}\right) = \frac{g_0}{\mu}.$$

One of the α_m must take the value 1 so that there is a term to balance with the $O(1)$ term on the right hand side. Following another relabelling we can write

$$a_1 + \sum_{m=2}^{\infty}\rho^{\alpha_m-1}\alpha_m\left(-a_m\sin\frac{3\alpha_m\pi}{2} + b_m\cos\frac{3\alpha_m\pi}{2}\right) = \frac{g_0}{\mu\bar{\Sigma}_1\sqrt{\bar{\Sigma}_1\bar{\Sigma}_3 - \bar{\Sigma}_2^2}}.$$

Comparing coefficients of powers of ρ yields

$$\begin{aligned} a_1 &= \frac{g_0}{\mu\bar{\Sigma}_1\sqrt{\bar{\Sigma}_1\bar{\Sigma}_3 - \bar{\Sigma}_2^2}}, \\ b_m &= a_m\tan\frac{3\alpha_m\pi}{2}. \end{aligned}$$

Define

$$c_m = \frac{a_m}{\cos\frac{3\alpha_m\pi}{2}},$$

and then the velocity (9.29) can be written

$$\begin{aligned}\nu^p &= \rho\left(\frac{g_0\cos\phi}{\mu\bar{\Sigma}_1\sqrt{\bar{\Sigma}_1\bar{\Sigma}_3-\bar{\Sigma}_2^2}}+b_1\sin\phi\right)\\ &\quad+\sum_{m=2}^{\infty}\rho^{\alpha_m}c_m\cos\left(\alpha_m\left(\phi-\frac{3\pi}{2}\right)\right).\end{aligned}\tag{9.31}$$

Using the identities (9.26), continuity of velocity (9.25) can be expressed as

$$\begin{aligned}&-\frac{g_0 r}{\mu}+\sum_{m=2}^{\infty}r^{\gamma_m}C_m\cos\frac{\gamma_m\pi}{2}\\ &=-\rho_I r\left(\frac{g_0\cos\Phi}{\mu\bar{\Sigma}_1\sqrt{\bar{\Sigma}_1\bar{\Sigma}_3-\bar{\Sigma}_2^2}}+b_1\sin\Phi\right)\\ &+\sum_{m=2}^{\infty}\rho_I^{\alpha_m}r^{\alpha_m}c_m\cos\left(\alpha_m\left(\Phi-\frac{\pi}{2}\right)\right).\end{aligned}\tag{9.32}$$

Continuity of traction rate (9.27) becomes

$$\begin{aligned}&-B_1-\sum_{m=2}^{\infty}r^{\gamma_m-1}\gamma_m C_m\sin\frac{\gamma_m\pi}{2}\\ &=\frac{\bar{\Sigma}_1\bar{\Sigma}_3-\bar{\Sigma}_2^2}{\cos\Phi}\left[\frac{g_0\sin\Phi}{\mu\bar{\Sigma}_1\sqrt{\bar{\Sigma}_1\bar{\Sigma}_3-\bar{\Sigma}_2^2}}-b_1\cos\Phi\right.\\ &\left.-\sum_{m=2}^{\infty}\rho_I^{\alpha_m-1}r^{\alpha_m-1}\alpha_m c_m\sin\left(\alpha_m\left(\Phi-\frac{\pi}{2}\right)\right)\right].\end{aligned}\tag{9.33}$$

Suppose that there exists a k such that $\gamma_k \neq \alpha_m$, $\forall m$. Then the right hand side of (9.33) does not contain an $O(r^{\gamma_k-1})$ term and so either $C_k = 0$ or $\sin\frac{\gamma_k\pi}{2} = 0$ in order to match the powers of r on either side of the equation. The same argument for (9.32) results in the conditions $C_k = 0$ or $\cos\frac{\gamma_k\pi}{2} = 0$. Since both $\sin\frac{\gamma_k\pi}{2}$ and $\cos\frac{\gamma_k\pi}{2}$ cannot be both zero for strictly positive γ_k, it is required that $C_k = 0$. Hence, the expansion of ν^e does not contain any powers of r that the expansion of ν^p does not also contain. A similar argument also eliminates the possibility of there being a power of r in ν^p that does not appear in the expansion of ν^e. Without loss of generality it can be concluded that $\gamma_m = \alpha_m$, $\forall m$.

Comparing coefficients of powers of r in (9.32) gives

$$\frac{g_0}{\mu} = \rho_I \left(\frac{g_0 \cos\Phi}{\mu\bar{\Sigma}_1\sqrt{\bar{\Sigma}_1\bar{\Sigma}_3 - \bar{\Sigma}_2^2}} + b_1 \sin\Phi \right), \tag{9.34}$$

$$C_m \cos\alpha_m \frac{\pi}{2} = \rho_I^{\alpha_m} c_m \cos\left(\alpha_m\left(\Phi - \frac{\pi}{2}\right)\right), \tag{9.35}$$

and (9.33) yields

$$B_1 = -\frac{\bar{\Sigma}_1\bar{\Sigma}_3 - \bar{\Sigma}_2^2}{\cos\Phi}\left[\frac{g_0 \sin\Phi}{\mu\bar{\Sigma}_1\sqrt{\bar{\Sigma}_1\bar{\Sigma}_3 - \bar{\Sigma}_2^2}} - b_1\cos\Phi\right], \tag{9.36}$$

$$C_m \sin\alpha_m \frac{\pi}{2} = \frac{\bar{\Sigma}_1\bar{\Sigma}_3 - \bar{\Sigma}_2^2}{\cos\Phi}\rho_I^{\alpha_m - 1} c_m \sin\left(\alpha_m\left(\Phi - \frac{\pi}{2}\right)\right). \tag{9.37}$$

Equation (9.34) can be rearranged to find b_1,

$$b_1 = \frac{g_0}{\rho_I \mu \sin\Phi} - \frac{g_0 \cot\Phi}{\mu\bar{\Sigma}_1\sqrt{\bar{\Sigma}_1\bar{\Sigma}_3 - \bar{\Sigma}_2^2}}, \tag{9.38}$$

and this can be substituted into (9.36) to find B_1,

$$\begin{aligned} B_1 &= -\frac{\bar{\Sigma}_1\bar{\Sigma}_3 - \bar{\Sigma}_2^2}{\cos\Phi}\left[\frac{g_0\sin\Phi}{\mu\bar{\Sigma}_1\sqrt{\bar{\Sigma}_1\bar{\Sigma}_3 - \bar{\Sigma}_2^2}} - \frac{g_0\cot\Phi}{\rho_I\mu} + \frac{g_0\cot\Phi\cos\Phi}{\mu\bar{\Sigma}_1\sqrt{\bar{\Sigma}_1\bar{\Sigma}_3 - \bar{\Sigma}_2^2}}\right] \\ &= -\frac{g_0}{\mu}\frac{\bar{\Sigma}_1\bar{\Sigma}_3 - \bar{\Sigma}_2^2}{\cos^3\Phi\sin^2\Phi}\left(\sin\Phi - \bar{\Sigma}_1\right). \end{aligned} \tag{9.39}$$

Define

$$D_m = C_m \cos\frac{\alpha_m\pi}{2}, \tag{9.40}$$

$$d_m = \rho_I^{\alpha_m} c_m \cos\left(\alpha_m\left(\Phi - \frac{\pi}{2}\right)\right), \tag{9.41}$$

then (9.35) states that $D_m = d_m$ and subsequently (9.37) becomes

$$d_m \tan\frac{\alpha_m\pi}{2} = d_m \frac{\bar{\Sigma}_1\bar{\Sigma}_3 - \bar{\Sigma}_2^2}{\rho_I\cos\Phi}\tan\left(\alpha_m\left(\Phi - \frac{\pi}{2}\right)\right).$$

This has the trivial solution $d_m = 0$ which will eliminate both the sums in (9.30) and (9.31) and lead to the trivial solution for the velocity perturbation or, alternatively, α_m satisfies

$$\tan\frac{\alpha_m\pi}{2} - \frac{\bar{\Sigma}_1\bar{\Sigma}_3 - \bar{\Sigma}_2^2}{\rho_I\cos\Phi}\tan\left(\alpha_m\left(\Phi - \frac{\pi}{2}\right)\right) = 0. \tag{9.42}$$

The velocity perturbations are therefore given by (9.30) and (9.31) together with the definitions of d_m and D_m given by (9.40) and (9.41).

$$\nu^e = r\left(\frac{g_0}{\mu}\cos\theta + B_1\sin\theta\right) + \sum_{m=2}^{\infty} d_m r^{\alpha_m}\frac{\cos\left(\alpha_m\left(\theta - \frac{\pi}{2}\right)\right)}{\cos\frac{\alpha_m\pi}{2}}, \tag{9.43}$$

$$\nu^p = \rho\left(\frac{g_0\cos\phi}{\mu\bar{\Sigma}_1\sqrt{\bar{\Sigma}_1\bar{\Sigma}_3 - \bar{\Sigma}_2^2}} + b_1\sin\phi\right) + \sum_{m=2}^{\infty} d_m\left(\frac{\rho}{\rho_I}\right)^{\alpha_m}\frac{\cos\left(\alpha_m\left(\phi + \frac{\pi}{2}\right)\right)}{\left(\cos\alpha_m\left(\Phi + \frac{\pi}{2}\right)\right)}. \tag{9.44}$$

The values of α_m are determined by (9.42) and the coefficients b_1 and B_1 are given by (9.38) and (9.39) respectively. Unfortunately, equation (9.42) has no non-trivial solutions and so this solution cannot be used to approximate the velocity near this corner. A probable cause of this is that the asymptotic behaviours given by (9.1) do not accurately capture the local behaviour of the solution. It is possible that the velocity, stresses and coordinates do not all vary in the same manner and perturbations of different orders of magnitude to $O(\epsilon)$ are required. Laplace's equation, however, becomes too simple in the case where the velocities and coordinates do not have the same perturbation and so the error probably lies in the stresses. This prospect is not considered further in this thesis.

9.3 Singularity at the end of the Elasto-Plastic Boundary

Figure 9.5 shows the local geometry near the point where the elasto-plastic boundary meets the line $y = w$. We introduce a local coordinate system (X, Y) near the corner which has coordinates $(x, y) = (z, w)$. The scalings $x = z + \epsilon X$ and

$y = w + \epsilon Y$ relate the inner and outer coordinates. The elasto-plastic boundary is taken to be a straight line in the vicinity of the corner and makes an angle ω with the positive X axis measured anticlockwise. The definitions of ξ, η, r, θ, ρ and ϕ are taken to be the analogous to the previous section. Since the shear modulus in the fault is the same as in the tectonic plate, the part of the domain defined by $0 \leq \theta \leq \omega$ is taken to be just one region, the velocity here is denoted V^e. In the remainder of the domain the velocity is denoted V^p. The dependent variables are rescaled using (9.1) as before to reduce the governing equations to Laplace's equation as given by (9.20) and (9.21). We denote the part of the boundary given by the positive X axis as I and the part aligned with $Y = X \tan\omega$ is denoted II. In the previous section it was shown that along I, $\phi = \Phi$ where Φ satisfies the equation

$$\tan\Phi = \frac{\bar{\Sigma}_2}{\sqrt{\bar{\Sigma}_1\bar{\Sigma}_3 - \bar{\Sigma}_2^2}}.$$

Similarly on II, ϕ takes the value Ω which satisfies

$$\tan\Omega = \frac{\bar{\Sigma}_2 + \bar{\Sigma}_1\tan\omega}{\sqrt{\bar{\Sigma}_1\bar{\Sigma}_3 - \bar{\Sigma}_2^2}}, \tag{9.45}$$

however, the definition of Ω must have a rather more complicated definition because $\omega \in [\pi, 2\pi]$ and tan is a periodic function; taking the inverse tan of (9.45) will give a value in the fundamental domain of $\left[-\frac{\pi}{2}, \frac{\pi}{2}\right]$. In order to have a continuous velocity field in the plastic region it is required that $\Omega \in [\Phi - \pi, \Phi]$. If $\omega \in \left[\pi, \frac{3\pi}{2}\right]$ then we require $\Omega \in \left[\Phi - \pi, -\frac{\pi}{2}\right]$. In this case $\tan\omega \in [0, \infty)$ and so

$$\tan\Omega = \frac{\bar{\Sigma}_2 + \bar{\Sigma}_1\tan\omega}{\sqrt{\bar{\Sigma}_1\bar{\Sigma}_3 - \bar{\Sigma}_2^2}} \in [\tan\Phi, \infty)\ .$$

The inverse tan of this will give a value of Ω in the range $\left[\Phi, \frac{\pi}{2}\right]$ in the fundamental domain. To obtain a value in the correct range that also satisfies (9.45) we use the

definition

$$\Omega = -\pi + \tan^{-1}\left(\frac{\bar{\Sigma}_2 + \bar{\Sigma}_1 \tan\omega}{\sqrt{\bar{\Sigma}_1\bar{\Sigma}_3 - \bar{\Sigma}_2^2}}\right).$$

Now if $\omega \in \left[\frac{3\pi}{2}, 2\pi - \tan^{-1}\left(\frac{\bar{\Sigma}_2}{\bar{\Sigma}_1}\right)\right]$ then we wish $\Omega \in \left[-\frac{\pi}{2}, 0\right]$. Then $\tan\omega \in \left(-\infty, -\frac{\bar{\Sigma}_2}{\bar{\Sigma}_1}\right]$ and so

$$\tan\Omega = \frac{\bar{\Sigma}_2 + \bar{\Sigma}_1 \tan\omega}{\sqrt{\bar{\Sigma}_1\bar{\Sigma}_3 - \bar{\Sigma}_2^2}} \in [-\infty, 0)\,.$$

We therefore choose the definition

$$\Omega = \tan^{-1}\left(\frac{\bar{\Sigma}_2 + \bar{\Sigma}_1 \tan\omega}{\sqrt{\bar{\Sigma}_1\bar{\Sigma}_3 - \bar{\Sigma}_2^2}}\right),$$

for this range of values of ω. Finally, for $\omega \in \left[2\pi - \tan^{-1}\left(\frac{\bar{\Sigma}_2}{\bar{\Sigma}_1}\right), 2\pi\right]$, we want $\Omega \in [0, \Phi]$. Then $\tan\omega \in \left[-\frac{\bar{\Sigma}_2}{\bar{\Sigma}_1}, 0\right]$ and

$$\frac{\bar{\Sigma}_2 + \bar{\Sigma}_1 \tan\omega}{\sqrt{\bar{\Sigma}_1\bar{\Sigma}_3 - \bar{\Sigma}_2^2}} \in [0, \tan\Phi]\,.$$

The inverse tan of this then gives values in the correct range, hence the definition

$$\Omega = \tan^{-1}\left(\frac{\bar{\Sigma}_2 + \bar{\Sigma}_1 \tan\omega}{\sqrt{\bar{\Sigma}_1\bar{\Sigma}_3 - \bar{\Sigma}_2^2}}\right),$$

is valid in this range of values of ω. We can combine these values of Ω into one split definition

$$\Omega = \begin{cases} -\pi + \tan^{-1}\left(\dfrac{\bar{\Sigma}_2 + \bar{\Sigma}_1 \tan\omega}{\sqrt{\bar{\Sigma}_1\bar{\Sigma}_3 - \bar{\Sigma}_2^2}}\right), & \omega \in \left[\pi, \frac{3\pi}{2}\right] \\ \tan^{-1}\left(\dfrac{\bar{\Sigma}_2 + \bar{\Sigma}_1 \tan\omega}{\sqrt{\bar{\Sigma}_1\bar{\Sigma}_3 - \bar{\Sigma}_2^2}}\right), & \omega \in \left[\frac{3\pi}{2}, 2\pi\right] \end{cases} \tag{9.46}$$

Having rigorously solved a similar corner problem we can start now with the following forms for the perturbation to the velocity at the corner

$$\nu^e = \sum_{m=1}^{\infty} r^{\alpha_m} \left(A_m \cos \alpha_m \theta + B_m \sin \alpha_m \theta \right), \tag{9.47}$$

$$\nu^p = \sum_{m=1}^{\infty} \rho^{\alpha_m} \left(a_m \cos \alpha_m \phi + b_m \sin \alpha_m \phi \right). \tag{9.48}$$

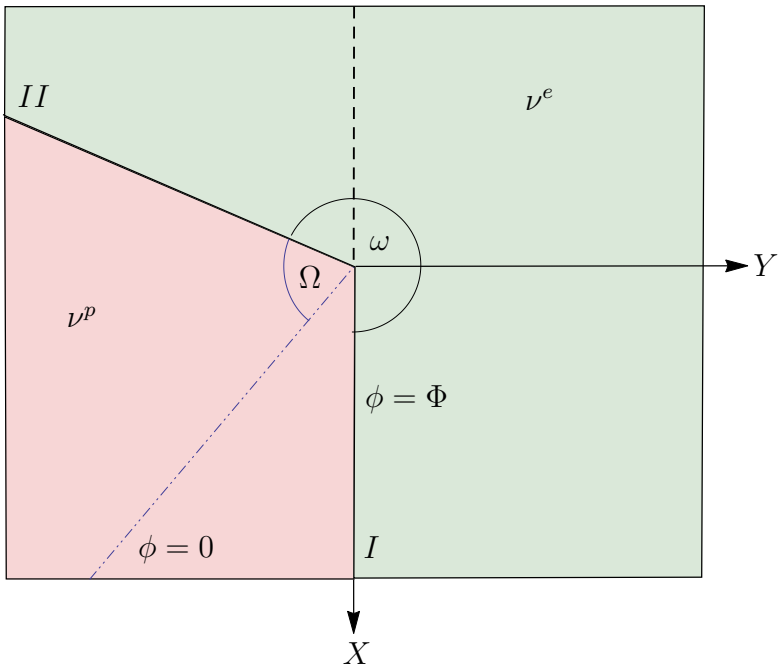

Figure 9.5: Local geometry near the corner where the elasto-plastic boundary meets the edge of the fault. The elastic behaving regions are shaded green and the red region is the region of fault material in yield. The velocity perturbations are ν^e and ν^p in the respective regions. The coordinates X and Y radiant from the corner vertically downwards and horizontally. The boundaries between the two regions are denoted I and II. The polar angle θ is measured anticlockwise from the positive X axis and takes the value ω on II. The elliptical polar angle ϕ is measured anticlockwise and takes the value Φ on I and Ω on II. The line $\phi = 0$ is shown by the dashed and dotted line.

Continuity of velocity across I requires $\nu^e(\theta = 0) = \nu^p(\phi = \Phi)$. The expansions (9.47) and (9.48) then give

$$\sum_{m=1}^{\infty} A_m r^{\alpha_m} = \sum_{m=1}^{\infty} \rho^{\alpha_m} \left(a_m \cos \alpha_m \Phi + b_m \sin \alpha_m \Phi\right). \tag{9.49}$$

Along the positive X axis $r = X$ and

$$\rho = X\sqrt{\bar{\Sigma}_1 \bar{\Sigma}_3} = \rho_I X. \tag{9.50}$$

Comparing powers of X in (9.49) yields

$$A_m = \rho_I^{\alpha_m} \left(a_m \cos \alpha_m \Phi + b_m \sin \alpha_m \Phi\right). \tag{9.51}$$

Continuity of velocity across II requires $\nu^p(\theta = \omega) = \nu^p(\phi = \Omega)$. The expansions (9.47) and (9.48) then give

$$\sum_{m=1}^{\infty} r^{\alpha_m} \left(A_m \cos \alpha_m \omega + B_m \sin \alpha_m \omega\right) = \sum_{m=1}^{\infty} \rho^{\alpha_m} \left(a_m \cos \alpha_m \Omega + b_m \sin \alpha_m \Omega\right) \tag{9.52}$$

The line II is given by $Y = X \tan \omega$ and so using the definitions of ξ and η from (9.15), the value of ρ along II is given by

$$\rho = |Y| \sqrt{\frac{\bar{\Sigma}_1 \bar{\Sigma}_3 - \bar{\Sigma}_2^2}{\tan^2 \omega} + \left(\frac{\bar{\Sigma}_2}{\tan \omega} + \bar{\Sigma}_1\right)^2}.$$

Within the fault $Y < 0$ and so along II the value of ρ is

$$\rho = -Y \sqrt{\frac{\bar{\Sigma}_1 \bar{\Sigma}_3 - \bar{\Sigma}_2^2}{\tan^2 \omega} + \left(\frac{\bar{\Sigma}_2}{\tan \omega} + \bar{\Sigma}_1\right)^2}. \tag{9.53}$$

The value of Y along II is given by $Y = r \sin \omega$. Define

$$\rho_{II} = -\sin \omega \sqrt{\frac{\bar{\Sigma}_1 \bar{\Sigma}_3 - \bar{\Sigma}_2^2}{\tan^2 \omega} + \left(\frac{\bar{\Sigma}_2}{\tan \omega} + \bar{\Sigma}_1\right)^2}.$$

so that $\rho = \rho_{II} r$ on II. This can be substituted into (9.52) and comparing coefficients of r yields

$$A_m \cos \alpha_m \omega + B_m \sin \alpha_m \omega = \rho_{II}^{\alpha_m} \left(a_m \cos \alpha_m \Omega + b_m \sin \alpha_m \Omega \right). \tag{9.54}$$

Continuity of traction rate across a radial line $Y = \tan\theta X$ is

$$\begin{aligned}
\frac{1}{r}\frac{\partial \nu^e}{\partial \theta} &= -\sin\theta \left(\bar{\Sigma}_1 \frac{\partial \nu^p}{\partial X} - \bar{\Sigma}_2 \frac{\partial \nu^p}{\partial Y} \right) + \cos\theta \left(-\bar{\Sigma}_2 \frac{\partial \nu^p}{\partial X} + \bar{\Sigma}_3 \frac{\partial \nu^p}{\partial Y} \right) \\
&= -\left(\bar{\Sigma}_1 \sin\theta + \bar{\Sigma}_2 \cos\theta \right) \frac{\partial \nu^p}{\partial X} + \left(\bar{\Sigma}_2 \sin\theta + \bar{\Sigma}_3 \cos\theta \right) \frac{\partial \nu^p}{\partial Y} \\
&= -\sqrt{\bar{\Sigma}_1 \bar{\Sigma}_3 - \bar{\Sigma}_2^2} \left(\bar{\Sigma}_1 \sin\theta + \bar{\Sigma}_2 \cos\theta \right) \frac{\partial \nu^p}{\partial \xi} + (\bar{\Sigma}_1 \bar{\Sigma}_3 - \bar{\Sigma}_2^2) \cos\theta \frac{\partial \nu^p}{\partial \eta} \\
&= (\bar{\Sigma}_1 \bar{\Sigma}_3 - \bar{\Sigma}_2^2) \cos\theta \cos\phi \left(\tan\phi - \frac{\bar{\Sigma}_2 + \bar{\Sigma}_1 \tan\theta}{\sqrt{\bar{\Sigma}_1 \bar{\Sigma}_3 - \bar{\Sigma}_2^2}} \right) \frac{\partial \nu^p}{\partial \rho} \\
&\quad + (\bar{\Sigma}_1 \bar{\Sigma}_3 - \bar{\Sigma}_2^2) \frac{\cos\theta}{\cos\phi} \frac{1}{\rho} \frac{\partial \nu^p}{\partial \phi}.
\end{aligned}$$

The terms in the large parenthesis are identically zero by definition of ϕ. Hence

$$\frac{1}{r}\frac{\partial \nu^e}{\partial \theta} = (\bar{\Sigma}_1 \bar{\Sigma}_3 - \bar{\Sigma}_2^2) \frac{\cos\theta}{\cos\phi} \frac{1}{\rho} \frac{\partial \nu^p}{\partial \phi}. \tag{9.55}$$

Therefore on I continuity of traction-rate is

$$\left. \frac{1}{r}\frac{\partial \nu^e}{\partial \theta} \right|_{\theta=0} = \frac{\bar{\Sigma}_1 \bar{\Sigma}_3 - \bar{\Sigma}_2^2}{\cos\Phi} \left. \frac{1}{\rho} \frac{\partial \nu^p}{\partial \phi} \right|_{\phi=\Phi},$$

which, when the expansions (9.47) and (9.48) are substituted in, yields

$$B_m = \frac{\bar{\Sigma}_1 \bar{\Sigma}_3 - \bar{\Sigma}_2^2}{\cos\Phi} \rho_I^{\alpha_m - 1} (-a_m \sin \alpha_m \Phi + b_m \cos \alpha_m \Phi). \tag{9.56}$$

Similarly on II the equation

$$\left. \frac{1}{r}\frac{\partial \nu^e}{\partial \theta} \right|_{\theta=\omega} = (\bar{\Sigma}_1 \bar{\Sigma}_3 - \bar{\Sigma}_2^2) \frac{\cos\omega}{\cos\Omega} \left. \frac{1}{\rho} \frac{\partial \nu^p}{\partial \phi} \right|_{\phi=\Omega},$$

holds which requires

$$\begin{aligned}&-A_m \sin\alpha_m\omega + B_m \cos\alpha_m\omega \\ &= (\bar{\Sigma}_1\bar{\Sigma}_3 - \bar{\Sigma}_2^2)\frac{\cos\omega}{\cos\Omega}\rho_{II}^{\alpha_m - 1}(-a_m \sin\alpha_m\Omega + b_m \cos\alpha_m\Omega). \end{aligned} \tag{9.57}$$

If $\omega = \frac{3\pi}{2}$ then the ratio $\frac{\cos\omega}{\cos\Omega}$ is undefined but the limit as $\omega \to \frac{3\pi}{2}$ does exist. In this limit

$$\tan\Omega \sim \frac{\bar{\Sigma}_1 \tan\omega}{\sqrt{\bar{\Sigma}_1\bar{\Sigma}_3 - \bar{\Sigma}_2}},$$

which can be rearranged to give

$$\frac{\cos\omega}{\cos\Omega} \sim \frac{\bar{\Sigma}_1}{\sqrt{\bar{\Sigma}_1\bar{\Sigma}_3 - \bar{\Sigma}_2}}\frac{\sin\omega}{\sin\Omega} \to \frac{\bar{\Sigma}_1}{\sqrt{\bar{\Sigma}_1\bar{\Sigma}_3 - \bar{\Sigma}_2}},$$

as $\omega \to \frac{3\pi}{2}$.

Equations (9.51), (9.54), (9.56) and (9.57) define a set of 4 equations in the unknowns a_m, b_m, A_m, B_m and α_m. Since the equations are all homogeneous the unique solution is the trivial solution unless the determinant of the coefficient matrix is zero. Setting the determinant to zero forms an equation which defines an infinite set of eigenvalues. An explicit expression for the determinant is not expressed here due to its complexity and, since it is non-linear, does not permit an analytical solution to be obtained.

Substituting (9.51) and (9.56) into (9.54) gives

$$\begin{aligned}&\rho_I^{\alpha_m}(a_m \cos\alpha_m\Phi + b_m \sin\alpha_m\Phi)\cos\alpha_m\omega \\ &\frac{\bar{\Sigma}_1\bar{\Sigma}_3 - \bar{\Sigma}_2}{\cos\Phi}\rho_I^{\alpha_m - 1}(-a_m \sin\alpha_m\Phi + b_m \cos\alpha_m\Phi)\sin\alpha_m\omega \\ &= \rho_{II}^{\alpha_m}(a_m \cos\alpha_m\Omega + b_m \sin\alpha_m\Omega), \end{aligned} \tag{9.58}$$

which can be factorised to

$$
\begin{aligned}
& a_m \left[\rho_I^{\alpha_m} \cos\alpha_m\Phi \cos\alpha_m\omega - \frac{\bar{\Sigma}_1\bar{\Sigma}_3 - \bar{\Sigma}_2}{\cos\Phi} \rho_I^{\alpha_m - 1} \sin\alpha_m\Phi \sin\alpha_m\omega - \rho_{II}^{\alpha_m} \cos\alpha_m\Omega \right] \\
& = b_m \left[\rho_{II}^{\alpha_m} \sin\alpha_m\Omega - \rho_I^{\alpha_m} \sin\alpha_m\Phi \cos\alpha_m\omega \right. \\
& \left. - \frac{\bar{\Sigma}_1\bar{\Sigma}_3 - \bar{\Sigma}_2^2}{\cos\Phi} \rho_I^{\alpha_m - 1} \cos\alpha_m\Phi \sin\alpha_m\omega \right] .
\end{aligned}
\tag{9.59}
$$

For simplicity we introduce the coefficients c_m such that $a_m = c_m b_m$ where the c_m are defined by the appropriate ratio of the terms in the square parenthesis above. The two equations (9.51) and (9.56) can then be utilised to obtain expressions for A_m and B_m in terms of the b_m. We further introduce the coefficients Γ_1 and Γ_2 such that

$$
\begin{aligned}
A_m &= \rho_I^{\alpha_m} b_m (c_m \cos\alpha_m\Phi + \sin\alpha_m\Phi) = \Gamma_m^1 b_m , \\
B_m &= = \frac{\bar{\Sigma}_1\bar{\Sigma}_3 - \bar{\Sigma}_2^2}{\cos\Phi} \rho_I^{\alpha_m - 1} b_m (-c_m \sin\alpha_m\Phi + \cos\alpha_m\Phi) = \Gamma_m^2 b_m .
\end{aligned}
$$

The local variation in the velocity in the two regions, as given by (9.47) and (9.48), can be expressed as

$$
\nu^e = \sum_{m=1}^{\infty} r^{\alpha_m} b_m \left(\Gamma_m^1 \cos\alpha_m\theta + \Gamma_m^2 \sin\alpha_m\theta \right) , \tag{9.60}
$$

$$
\nu^p = \sum_{m=1}^{\infty} \rho^{\alpha_m} b_m \left(c_m \cos\alpha_m\phi + \sin\alpha_m\phi \right) . \tag{9.61}
$$

9.4 Implementation

We now show how the singular perturbation terms derived in the previous section are utilised to reduce the problem to one with a regular solution which can be solved for using a numerical scheme.

Divide the domain into two regions, $\mathcal{D}_1$ and $\mathcal{D}_2$, as shown in Figure 9.6. The inner region, $\mathcal{D}_1$, lies within the closed contour $\mathcal{C}$ which surrounds the corner.

Within this region the velocity takes the form

$$V = \bar{V} + \epsilon\nu.$$

Superposed e and p are applied to all terms to correspond to the elastic and plastic regions respectively. The latter part, ν, takes the form of the expansions given by (9.60) and (9.61) and contains only the terms with $\alpha_m < 1$. Therefore, in region $\mathcal{D}_1$ the singular term is given by

$$\nu^e = r^{\alpha_1} b \left(\Gamma^1 \cos \alpha_1 \theta + \Gamma^2 \sin \alpha_1 \theta \right), \tag{9.62}$$

$$\nu^p = \rho^{\alpha_1} b \left(c \cos \alpha_1 \phi + \sin \alpha_1 \phi \right), \tag{9.63}$$

in the elastic and plastic regions respectively. The subscripts on the b, c and Γ^i are dropped for simplicity.

Region II is termed the outer region and lies on the exterior of the closed contour $\mathcal{C}$. In this region the full solution is regular and the velocity $V = \bar{V}$ can be solved for using the standard finite difference scheme outlined in Chapter 7.

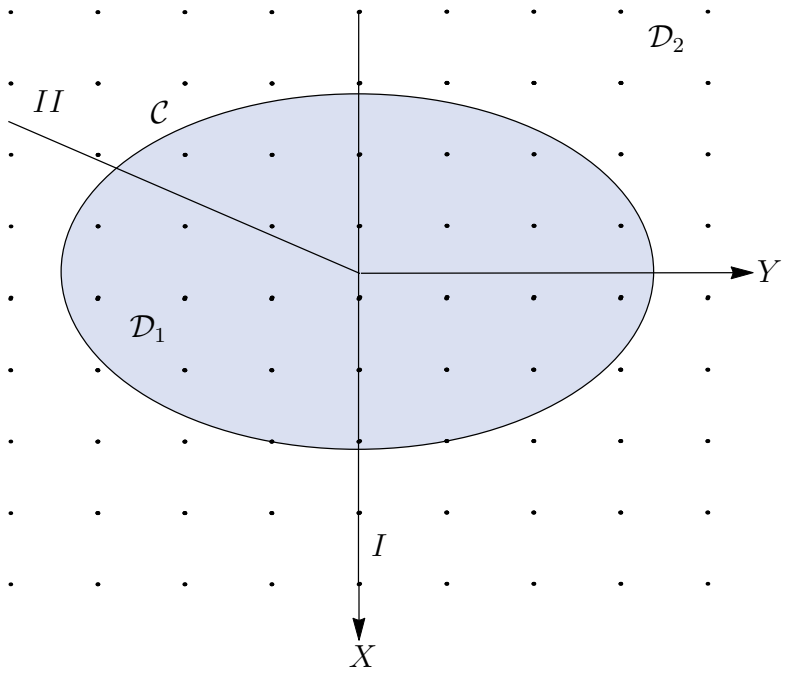

Figure 9.6: The inner region, $\mathcal{D}_1$ lies inside a closed contour $\mathcal{C}$ which surrounds the corner. This is shown in blue and within this region the singular terms in the velocity perturbation are subtracted from the full solution. Outside $\mathcal{C}$ lies the outer region in which the finite difference scheme of Chapter 7 is implemented.

There is a disparity between the definition of $\bar{V}$ either side of $\mathcal{C}$ and this must be accounted for in the numerical scheme. At points in $\mathcal{D}_1$ we finite difference as usual for $\bar{V}$ and any occurence of nodal velocities at points in $\mathcal{D}_2$ are modified by subtracting off the value of ν at that point. Conversely, at points in $\mathcal{D}_2$ we use the finite difference expressions for $\bar{V}$ and add the value of ν to the nodal velocity of any points in $\mathcal{D}_1$.

9.4.1 Governing Equations in the Inner Regions

Since ν^e satisfies Laplace's equation, substitution of $V^e = \bar{V}^e + \epsilon\nu^e$ simply yields $\nabla^2\bar{V} = 0$ as before. The function ν^p satisfies the plasticity equation when the coefficients take their values at the corner, $\bar{\Sigma}_i$ and $\bar{M}_i$. At points within $\mathcal{D}_1$ different from the corner the coefficients $\Sigma_i \neq \bar{\Sigma}_i$ and $M_i \neq \bar{M}_i$. As such, substitution of

$V = \bar{V} + \epsilon\nu$ into the plasticity equation, (7.6), yields

$$\begin{aligned}
&\Sigma_1 \frac{\partial^2 \bar{V}}{\partial x^2} + \Sigma_3 \frac{\partial^2 \bar{V}}{\partial y^2} - 2\Sigma_2 \frac{\partial^2 \bar{V}}{\partial x \partial y} + M_1 \frac{\partial \bar{V}}{\partial x} + M_2 \frac{\partial \bar{V}}{\partial y} \\
&\Sigma_1 \frac{\partial^2 \nu^p}{\partial X^2} + \Sigma_3 \frac{\partial^2 \nu^p}{\partial Y^2} - 2\Sigma_2 \frac{\partial^2 \nu^p}{\partial X \partial Y} + M_1 \frac{\partial \nu^p}{\partial X} + M_2 \frac{\partial \nu^p}{\partial Y} = 0.
\end{aligned}$$

Define $S_i = \Sigma_i - \bar{\Sigma}_i$ and $m_i = M_i - \bar{M}_i$ so that this may be written

$$\begin{aligned}
&\Sigma_1 \frac{\partial^2 \bar{V}}{\partial x^2} + \Sigma_3 \frac{\partial^2 \bar{V}}{\partial y^2} - 2\Sigma_2 \frac{\partial^2 \bar{V}}{\partial x \partial y} + M_1 \frac{\partial \bar{V}}{\partial x} + M_2 \frac{\partial \bar{V}}{\partial y} \\
&S_1 \frac{\partial^2 \nu^p}{\partial X^2} + S_3 \frac{\partial^2 \nu^p}{\partial Y^2} - 2S_2 \frac{\partial^2 \nu^p}{\partial X \partial Y} + m_1 \frac{\partial \nu^p}{\partial X} + m_2 \frac{\partial \nu^p}{\partial Y} \\
&\bar{\Sigma}_1 \frac{\partial^2 \nu^p}{\partial X^2} + \bar{\Sigma}_3 \frac{\partial^2 \nu^p}{\partial Y^2} - 2\bar{\Sigma}_2 \frac{\partial^2 \nu^p}{\partial X \partial Y} + \bar{M}_1 \frac{\partial \nu^p}{\partial X} + \bar{M}_2 \frac{\partial \nu^p}{\partial Y} = 0. \qquad (9.64)
\end{aligned}$$

By definition of ν^p the third line is identically zero. The second can be transformed into ξ and η coordinates using the definitions (9.15) to obtain

$$\begin{aligned}
&S_1 \left(\bar{\Sigma}_1 \bar{\Sigma}_3 - \bar{\Sigma}_2^2\right) \frac{\partial^2 \nu^p}{\partial \xi^2} + \left(S_1 \bar{\Sigma}_2^2 + S_3 \bar{\Sigma}_1^2 - 2S_2 \bar{\Sigma}_1 \bar{\Sigma}_2\right) \frac{\partial^2 \nu^p}{\partial \eta^2} \\
&+ \left(2S_1 \bar{\Sigma}_2 \sqrt{\bar{\Sigma}_1 \bar{\Sigma}_3 - \bar{\Sigma}_2^2} - 2S_2 \bar{\Sigma}_1 \sqrt{\bar{\Sigma}_1 \bar{\Sigma}_3 - \bar{\Sigma}_2^2}\right) \frac{\partial^2 \nu^p}{\partial \xi \partial \eta} \\
&m_1 \sqrt{\bar{\Sigma}_1 \bar{\Sigma}_3 - \bar{\Sigma}_2^2} \frac{\partial \nu^p}{\partial \xi} + \left(m_1 \bar{\Sigma}_2 + m_2 \bar{\Sigma}_1\right) \frac{\partial \nu^p}{\partial \eta} = 0.
\end{aligned}$$

The coefficients are labelled

$$\begin{aligned}
T_1 &= S_1 \left(\bar{\Sigma}_1 \bar{\Sigma}_3 - \bar{\Sigma}_2^2\right) \\
T_2 &= S_1 \bar{\Sigma}_2^2 + S_3 \bar{\Sigma}_1^2 - 2S_2 \bar{\Sigma}_1 \bar{\Sigma}_2 \\
T_3 &= 2\left(S_1 \bar{\Sigma}_2 - S_2 \bar{\Sigma}_1\right) \sqrt{\bar{\Sigma}_1 \bar{\Sigma}_3 - \bar{\Sigma}_2^2} \\
T_4 &= m_1 \sqrt{\bar{\Sigma}_1 \bar{\Sigma}_3 - \bar{\Sigma}_2^2} \\
T_5 &= m_1 \bar{\Sigma}_2 + m_2 \bar{\Sigma}_1.
\end{aligned}$$

To help with the calculations later, the first derivatives with respect to ξ and

η are stated below. The first derivatives with respect to ξ are

$$\begin{aligned}
\frac{\partial}{\partial\xi}\rho_1^\alpha\cos\alpha_1\phi &= \alpha_1\rho^{\alpha_1-1}\frac{\partial\rho}{\partial\xi}\cos\alpha_1\phi - \alpha_1\rho_1^\alpha\frac{\partial\phi}{\partial\xi}\sin\alpha_1\phi \\
&= \alpha_1\rho^{\alpha_1-1}\cos\phi\cos\alpha_1\phi + \alpha_1\rho^{\alpha_1-1}\sin\phi\sin\alpha_1\phi \\
&= \alpha_1\rho^{\alpha_1-1}\cos(1-\alpha_1)\phi, \\
\frac{\partial}{\partial\xi}\rho_1^\alpha\sin\alpha_1\phi &= \alpha_1\rho^{\alpha_1-1}\frac{\partial\rho}{\partial\xi}\sin\alpha_1\phi + \alpha_1\rho_1^\alpha\frac{\partial\phi}{\partial\xi}\cos\alpha_1\phi \\
&= \alpha_1\rho^{\alpha_1-1}\cos\phi\sin\alpha_1\phi - \alpha_1\rho^{\alpha_1-1}\sin\phi\cos\alpha_1\phi \\
&= -\alpha_1\rho^{\alpha_1-1}\sin(1-\alpha_1)\phi, \qquad (9.65)
\end{aligned}$$

and the first η derivatives are

$$\begin{aligned}
\frac{\partial}{\partial\eta}\rho_1^\alpha\cos\alpha_1\phi &= \alpha_1\rho^{\alpha_1-1}\sin(1-\alpha_1)\phi, \\
\frac{\partial}{\partial\eta}\rho_1^\alpha\sin\alpha_1\phi &= \alpha_1\rho^{\alpha_1-1}\cos(1-\alpha_1)\phi. \qquad (9.66)
\end{aligned}$$

Similarly the second derivatives with respect to ξ are

$$\begin{aligned}
\frac{\partial^2}{\partial\xi^2}\rho_1^\alpha\cos\alpha_1\phi &= \alpha_1(\alpha_1-1)\rho^{\alpha_1-2}\frac{\partial\rho}{\partial\xi}\cos(1-\alpha_1)\phi + \alpha_1(\alpha_1-1)\rho^{\alpha_1-1}\frac{\partial\phi}{\partial\xi}\sin(1-\alpha_1)\phi \\
&= \alpha_1(\alpha_1-1)\rho^{\alpha_1-2}\cos\phi\cos(1-\alpha_1)\phi \\
&\quad -\alpha_1(\alpha_1-1)\rho^{\alpha_1-2}\sin\phi\sin(1-\alpha_1)\phi \\
&= \alpha_1(\alpha_1-1)\rho^{\alpha_1-2}\cos(2-\alpha_1)\phi, \\
\frac{\partial^2}{\partial\xi^2}\rho_1^\alpha\sin\alpha_1\phi &= -\alpha_1(\alpha_1-1)\rho^{\alpha_1-2}\sin(2-\alpha_1)\phi, \qquad (9.67)
\end{aligned}$$

and those with respect to η are

$$\begin{aligned}
\frac{\partial^2}{\partial\eta^2}\rho_1^\alpha\cos\alpha_1\phi &= -\alpha_1(\alpha_1-1)\rho^{\alpha_1-2}\cos(2-\alpha_1)\phi, \\
\frac{\partial^2}{\partial\eta^2}\rho_1^\alpha\sin\alpha_1\phi &= \alpha_1(\alpha_1-1)\rho^{\alpha_1-2}\sin(2-\alpha_1)\phi. \qquad (9.68)
\end{aligned}$$

Finally, the mixed derivatives are

$$\begin{aligned}\frac{\partial^2}{\partial\xi\partial\eta}\rho_1^\alpha\cos\alpha_1\phi &= \alpha_1(\alpha_1-1)\rho^{\alpha_1-2}\sin(2-\alpha_1)\phi,\\ \frac{\partial^2}{\partial\xi\partial\eta}\rho_1^\alpha\sin\alpha_1\phi &= \alpha_1(\alpha_1-1)\rho^{\alpha_1-2}\cos(2-\alpha_1)\phi.\end{aligned}\tag{9.69}$$

Using these expressions for the derivatives, substituting the singular terms of ν^p, given by (9.63), into the equation (9.64) yields the governing equation in $\mathcal{D}_1$

$$\begin{aligned}&\Sigma_1\frac{\partial^2\bar{V}}{\partial x^2}+\Sigma_3\frac{\partial^2\bar{V}}{\partial x^2}-2\Sigma_2\frac{\partial^2\bar{V}}{\partial x\partial y}+M_1\frac{\partial\bar{V}}{\partial x}+M_2\frac{\partial\bar{V}}{\partial y}\\ &+b\alpha_1(\alpha_1-1)\rho^{\alpha_1-2}[cT_1-cT_2+T_3]\cos(2-\alpha_1)\phi\\ &+b\alpha_1(\alpha_1-1)\rho^{\alpha_1-2}[-T_1+T_2+cT_3]\sin(2-\alpha_1)\phi\\ &+b\alpha_1\rho^{\alpha_1-1}[cT_4+T_5]\cos(1-\alpha_1)\phi\\ &+b\alpha_1\rho^{\alpha_1-1}[cT_5-T_4]\sin(1-\alpha_1)\phi=0.\end{aligned}$$

9.4.2 Boundary Conditions on the Edge of the Fault

As well as affecting the governing equations in the interior of the domains, the singular terms contribute to the boundary conditions. On the edge of the fault above the elasto-plastic boundary the boundary conditions are

$$\begin{aligned}\lim_{y\to w^-}V(x,y)&=\lim_{y\to w^+}V(x,y),\\ \lim_{y\to w^-}\frac{\partial V}{\partial y}(x,y)&=\lim_{y\to w^-}\frac{\partial V}{\partial y}(x,y).\end{aligned}$$

Substituting in the expression $V=\bar{V}+\epsilon\nu^e$ yields

$$\begin{aligned}\lim_{y\to w^-}\bar{V}+\epsilon\lim_{y\to w^-}\nu^e&=\lim_{y\to w^+}\bar{V}+\epsilon\lim_{y\to w^+}\nu^e,\\ \lim_{y\to w^-}\frac{\partial\bar{V}}{\partial y}+\lim_{y\to w^-}\frac{\partial\nu^e}{\partial Y}&=\lim_{y\to w^-}\frac{\partial\bar{V}}{\partial y}+\lim_{y\to w^-}\frac{\partial\nu^e}{\partial Y}.\end{aligned}$$

Since the singular term is derived in such a manner as to be smooth, the terms involving ν^e are automatically equal on either side of these expressions. Consequently, the new boundary conditions for the regular part of the velocity are

$$\lim_{y\to w^-} \bar{V}(x,y) = \lim_{y\to w^+} \bar{V}(x,y),$$
$$\lim_{y\to w^-} \frac{\partial \bar{V}}{\partial y}(x,y) = \lim_{y\to w^-} \frac{\partial \bar{V}}{\partial y}(x,y).$$

On the lower part of the edge of the fault the boundary condition is

$$\frac{\partial V^e}{\partial y} = -\Sigma_2 \frac{\partial V^p}{\partial x} + \Sigma_3 \frac{\partial V^p}{\partial y}. \tag{9.70}$$

Substitution of the expression $V = \bar{V} + \epsilon\nu$ in to this along with the use of notation involving S_i, as previously used, gives

$$\frac{\partial \bar{V}^e}{\partial y} + \frac{\partial \nu^e}{\partial Y} = -\Sigma_2 \frac{\partial \bar{V}^p}{\partial x} + \Sigma_3 \frac{\partial \bar{V}^p}{\partial y} - S_2 \frac{\partial \nu^p}{\partial X} + S_3 \frac{\partial \nu^p}{\partial Y} - \bar{\Sigma}_2 \frac{\partial \nu^p}{\partial X} + \bar{\Sigma}_3 \frac{\partial \nu^p}{\partial Y}.$$

The singular terms already satisfy the condition

$$\frac{\partial \nu^e}{\partial Y} = -\bar{\Sigma}_2 \frac{\partial \nu^p}{\partial X} + \bar{\Sigma}_3 \frac{\partial \nu^p}{\partial Y},$$

and so the boundary condition on the lower portion of the edge of the fault is

$$\frac{\partial \bar{V}^e}{\partial y} = -\Sigma_2 \frac{\partial \bar{V}^p}{\partial x} + \Sigma_3 \frac{\partial \bar{V}^p}{\partial y} - S_2 \frac{\partial \nu^p}{\partial X} + S_3 \frac{\partial \nu^p}{\partial Y}.$$

The derivatives of ν^p can be expressed in terms of ξ and η

$$\frac{\partial \bar{V}^e}{\partial y} = -\Sigma_2 \frac{\partial \bar{V}^p}{\partial x} + \Sigma_3 \frac{\partial \bar{V}^p}{\partial y} - S_2 \sqrt{\bar{\Sigma}_1 \bar{\Sigma}_3 - \bar{\Sigma}_2^2} \frac{\partial \nu^p}{\partial \xi} + \left(S_3 \bar{\Sigma}_1 - S_2 \bar{\Sigma}_2 \right) \frac{\partial \nu^p}{\partial \eta}.$$

On $y = w$ in $\mathcal{D}_1$, the definitions of ν^p then yield

$$\begin{aligned}\frac{\partial \bar{V}^e}{\partial y} &= -\Sigma_2 \frac{\partial \bar{V}^p}{\partial x} + \Sigma_3 \frac{\partial \bar{V}^p}{\partial y} \\ &\quad + \left(-S_2 c\sqrt{\bar{\Sigma}_1\bar{\Sigma}_3 - \bar{\Sigma}_2^2} + S_3\bar{\Sigma}_1 - S_2\bar{\Sigma}_2\right) b\alpha_1 \rho^{\alpha_1 - 1}\cos(1-\alpha_1)\phi \\ &\quad + \left(S_2\sqrt{\bar{\Sigma}_1\bar{\Sigma}_3 - \bar{\Sigma}_2^2} + c\left(S_3\bar{\Sigma}_1 - S_2\bar{\Sigma}_2\right)\right) b\alpha_1 \rho^{\alpha_1 - 1}\sin(1-\alpha_1)\phi.\end{aligned}$$

9.4.3 Boundary Condition on the Elasto-plastic Boundary

The perturbation solutions (9.60) and (9.61) are derived under the assumption that the elasto-plastic boundary is locally linear and this places a restriction on the size of the elliptical contour $\mathcal{C}$. The following boundary condition is therefore derived under the same assumption. The boundary condition is

$$\begin{aligned}-\sin\omega\frac{\partial V^e}{\partial x} + \cos\omega\frac{\partial V^e}{\partial y} &= -\left(\Sigma_1\sin\omega + \Sigma_2\cos\omega\right)\frac{\partial V^p}{\partial x} \\ &\quad + \left(\Sigma_3\cos\omega + \Sigma_2\sin\omega\right)\frac{\partial V^p}{\partial y},\end{aligned}$$

where $(-\sin\omega, \cos\omega)$ is the unit normal to the elasto-plastic boundary. Substitution of $V = \bar{V} + \epsilon\nu$ and cancelling the terms that satisfy continuity of traction-rate for the perturbation given by (9.55) gives

$$\begin{aligned}-\sin\omega\frac{\partial \bar{V}^e}{\partial x} + \cos\omega\frac{\partial \bar{V}^e}{\partial y} &= -\left(\Sigma_1\sin\omega + \Sigma_2\cos\omega\right)\frac{\partial \bar{V}^p}{\partial x} \\ &\quad + \left(\Sigma_3\cos\omega + \Sigma_2\sin\omega\right)\frac{\partial \bar{V}^p}{\partial y} \\ &\quad - \left(S_1\sin\omega + S_2\cos\omega\right)\frac{\partial \nu^p}{\partial X} \\ &\quad + \left(S_3\cos\omega + S_2\sin\omega\right)\frac{\partial \nu^p}{\partial Y}.\end{aligned}$$

Transforming the X and Y derivatives into ξ and η yields

$$\begin{aligned}-\sin\omega\frac{\partial\bar{V}^e}{\partial x}+\cos\omega\frac{\partial\bar{V}^e}{\partial y}=&-\left(\Sigma_1\sin\omega+\Sigma_2\cos\omega\right)\frac{\partial\bar{V}^p}{\partial x}+\left(\Sigma_3\cos\omega+\Sigma_2\sin\omega\right)\frac{\partial\bar{V}^p}{\partial y}\\&-\left(S_1\sin\omega+S_2\cos\omega\right)\sqrt{\bar{\Sigma}_1\bar{\Sigma}_3-\bar{\Sigma}_2^2}\frac{\partial\nu^p}{\partial\xi}\\&+\left[\bar{\Sigma}_1\left(S_3\cos\omega+S_2\sin\omega\right)-\bar{\Sigma}_2\left(S_1\sin\omega+S_2\cos\omega\right)\right]\frac{\partial\nu^p}{\partial\eta}.\end{aligned}$$

Introduce the coefficients c_ξ and c_η defined such that

$$\begin{aligned}-\sin\omega\frac{\partial\bar{V}^e}{\partial x}+\cos\omega\frac{\partial\bar{V}^e}{\partial y}=&-\left(\Sigma_1\sin\omega+\Sigma_2\cos\omega\right)\frac{\partial\bar{V}^p}{\partial x}+\left(\Sigma_3\cos\omega+\Sigma_2\sin\omega\right)\frac{\partial\bar{V}^p}{\partial y}\\&+c_\xi\frac{\partial\nu^p}{\partial\xi}+c_\eta\frac{\partial\nu^p}{\partial\eta}.\end{aligned}$$

The definition of ν^p given by (9.63) and the derivatives (9.65) and (9.66) reduce this to

$$\begin{aligned}-\sin\omega\frac{\partial\bar{V}^e}{\partial x}+\cos\omega\frac{\partial\bar{V}^e}{\partial y}=&-\left(\Sigma_1\sin\omega+\Sigma_2\cos\omega\right)\frac{\partial\bar{V}^p}{\partial x}+\left(\Sigma_3\cos\omega+\Sigma_2\sin\omega\right)\frac{\partial\bar{V}^p}{\partial y}\\&+b(c_\xi c+c_\eta)\alpha_1\rho^{\alpha_1-1}\cos(1-\alpha_1)\phi+b(c_\eta c-c_\xi)\alpha_1\rho^{\alpha_1-1}\sin(1-\alpha_1)\phi,\end{aligned}$$

which holds on $x=z(y)$.

9.5 Finite Difference Equation at the Corner

It is advisable to avoid using the finite difference equation that is explained at the end of Chapter 8 which is analogous to equation (8.11) to prevent the singular nature of the stress-rate being reintroduced in to the numerical solution. We therefore must derive an alternative equation to be satisfied by $\bar{V}$. Furthermore, the singular terms (9.62) and (9.63) introduce a new unknown, the coefficicient b, and an additional equation is required in order to maintain consistency of the system. The local behaviour of the stress-rate is accounted for by the singular terms and as such it can be assumed that the stress-rate of the numerical part of the solution is zero at the corner. By taking the grid point at the corner to be

part of the tectonic plate its stress-rate $\dot{\sigma}_{13}$ is proportional to the x derivative of V. The derivative can be approximated by a forwards and backwards difference and equated to zero to provide the necessary additional two equations. The finite difference expressions for a second order accurate one sided difference are given by

$$\begin{aligned} \frac{-\delta\left(2\eta_n+\delta_x\right)f(x)-\eta_n^2 f(x-(\eta_n+\delta_x))+(\eta_n+\delta_x)^2 f\left(x-\eta_n\right)}{\eta_n(\eta_n+\delta_x)\delta_x} &= 0, \\ \frac{\delta_x\left(3\delta_x-4\eta_n\right)f(x)+\delta_2^2 f\left(x+2\delta_x-\eta_n\right)-(2\delta_x-\eta_n)^2 f(x+\delta_x-\eta_n)}{\delta_x(\delta_x-\eta_n)(2\delta_x-\eta_n)} &= 0. \end{aligned}$$

Chapter 10

The Matlab Programme

The finite difference scheme deveoped in Chapters 7 and 8 is implemented by a purpose built Matlab code. Discussed in this chapter are some of the additional details that are required for the implementation.

10.1 Time Stepping the Stress

The stress-rates calculated have a peak and a discontinuity across the elasto-plastic boundary, see for example Figure 10.1 which shows the stress-rates at some time early in the deformation. In the continuous problem the position of the elasto-plastic boundary moves continuously. In the discretised analogue implemented in the Matlab code the position of the elasto-plastic boundary and consequently the discontinuity jumps by a finite amount in space between neighbouring time steps. Therefore, the intermediate points through which the elasto-plastic boundary would sweep during the timestep need to be given information about the discontinuity. In additions, standard linear interpolation of the stress-rate would lead to these discontinuities appearing in the stresses. Qualitatively the stress-rates look similar at neighbouring timesteps with the discontinuity simply translated to the new position. Presented in this section is a method of integrating the stress-rates through the time step which utilises this property to provide information to all points about the discontinuity. The method then uses this to estimate the stress at the next time step and, as a result, the coefficients in the elasto-plastic

equation, (5.37) can be treated as known quantities.

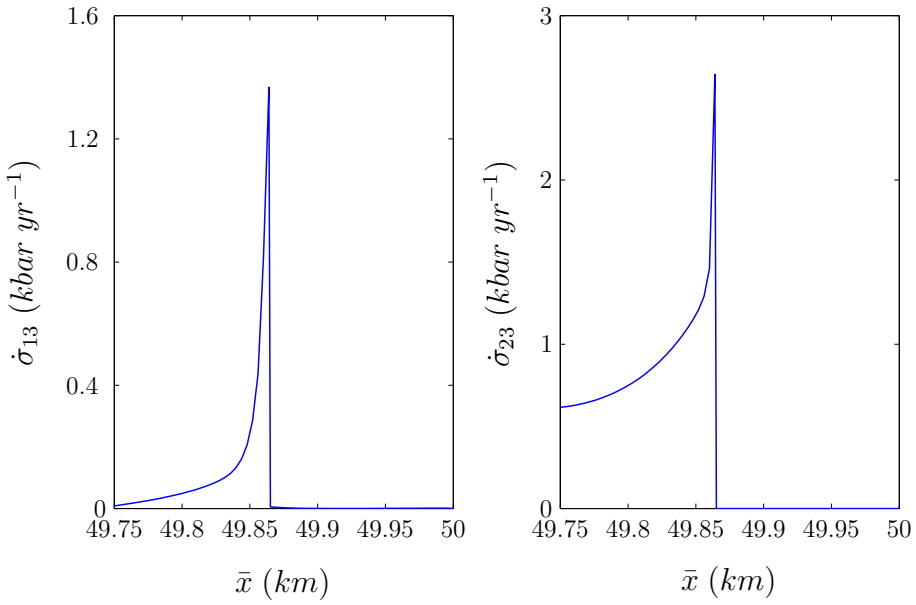

Figure 10.1: The discontinuous stress-rates at a representative time early in the deformation.

The increment of stress at time t, denoted by $\delta\sigma(t)$, is the increase in stress from time t to time $t + \delta t$ and is

$$\delta\sigma(t) = \int_t^{t+\delta t} \dot{\sigma}(\tau)d\tau, \tag{10.1}$$

so that the stress at time $t + \delta t$ is given by

$$\sigma(t + \delta t) = \sigma(t) + \delta\sigma(t).$$

The speed of propagation of the elasto-plastic boundary is denoted c and the stress rate in the intermediate time $\tau \in [t, t + \delta t]$ is given a translation in the negative x direction of the stress-rate at time t. Thus

$$\dot{\sigma}(x, \tau) = \dot{\sigma}(x + c(\tau - t), t). \tag{10.2}$$

The stress increment is therefore given by substituting (10.2) into (10.1),

$$\delta\sigma = \int_t^{t+\delta t} \dot{\sigma}(x + c(\tau - t), t)d\tau. \tag{10.3}$$

The speed, c, is assumed constant through the time step given by $[t, t + \delta t]$ and as such is expressed as the distance travelled by the elasto-plastic boundary divided by δt. Assuming the shape of the elasto-plastic boundary does not change through the time step and using the notation of $z(y, t)$ for the position of the boundary introduced at the start of Chapter 8 the speed is given by

$$c = \frac{z(0, t) - z(0, t + \delta t)}{\delta t}.$$

The value of $z(0, t + \delta t)$, however, is dependent on the stress at time $t + \delta t$ and is not known at time t. To overcome this an iterative scheme is implemented. In order to control the number of time steps required to solve the problem we define a maximum distance Δ_x by which the elasto-plastic boundary moves between time steps. A speed c_0 is assumed initially so that the length of the time step is given by $\delta t = \frac{\Delta_x}{c_0}$. The stress increment is calculated according to (10.3), added to the stresses at time t and the yield function evaluated. The new position of the elasto-plastic boundary can then be calculated and the value of c_0 updated. This iterative procedure is repeated until the c_n has converged to a value that leads to $z(0, t) - z(0, t + \delta t) = \Delta_x$. The algorithm used is Matlab's inbuilt `fzero` root finder function which uses Brent's method, a combined secant, bisection and inverse quadratic interpolation method, to converge with a relative error of 2^{-52} between consecutive iterations.

10.2 The Asthenosphere interaction

The evolution of the basal stress-rate $\mu\mathcal{G}$ controls the time evolution of the velocity field. In this section we first solve the boundary value problem given in Section 5.5.2 for the initial velocity and stress-rate in the lithosphere before discussing how $\mathcal{G}$ evolves with time by assuming it is a function of the velocity at previous time steps.

The initial velocity field in the lithosphere is given by the solution to Laplace's equation in the rectangular domain $(x, y) = [0, h] \times [0, L]$. The boundary condition on $y = 0$ is $V = 0$. On the boundaries defined by $x = 0$ and $y = L$ the normal derivatives are 0 and γ respectively. The velocity on $x = h$ is chosen to match the velocity at the top of the asthenosphere given by (5.32) which is restated below

$$V(h, y) = V_b(y) = \frac{\sigma_b}{2\eta_a d} y(2L - y) + \gamma y.$$

This boundary value problem can be solved by separation of variables to give the velocity

$$V(x, y, 0) = \gamma y + \sum_{m=1}^{\infty} B_m \frac{\sinh \Lambda_m x}{\sinh \Lambda_m h} \sin \Lambda_m y,$$

where the eigenvalues are

$$\Lambda_m = \frac{(2m - 1)\pi}{2(L + w)},$$

and the values of the coefficients are

$$\begin{aligned} B_m &= \frac{2\sigma_b}{\eta_a d} \left[\frac{\sin \Lambda_m L - \Lambda_m L \cos \Lambda_m L}{\Lambda_m^2} \right] \\ &\quad - \frac{\sigma_b}{L\eta_a d} \left[\frac{(2 - \Lambda_m^2 L^2) \cos \Lambda_m L + 2\Lambda_m L \sin \Lambda_m L}{\Lambda_m^3} - \frac{2}{\Lambda_m^3} \right]. \end{aligned}$$

The derivative of the velocity with respect to x is used to write the initial stress-rate on the base of the lithosphere as

$$\dot{\sigma}_{13} = \mu \left. \frac{\partial V}{\partial x} \right|_{x=h} = \mu \sum_{m=1}^{\infty} B_m \Lambda_m \coth \Lambda_m h \sin \Lambda_m y,$$

and consequently the initial value of $\mathcal{G}$ is

$$\mathcal{G}(y, 0) = \frac{1}{\mu} \sum_{m=1}^{\infty} B_m \Lambda_m \coth \Lambda_m h \sin \Lambda_m y.$$

At subsequent times the effect of the coupling with the asthenosphere is to increase

the basal velocity up to the far field velocity, $\frac{v_0}{2}$, measured on the Earth's surface and when such a velocity is obtained $\mathcal{G}$ should have decreased to zero. This is obtained in Rowshandel and Nemat-Nasser [1986] and is equivalent to the tectonic plate approaching a steady state rigid body motion. Due to the zero velocity at the center of the fault this rigid body motion is expected to occur at the far field first and as more of the tectonic plate reaches the steady state the strains at the fault increase. It is these strains that build up near the fault that are released during the dynamic earthquake event. To capture this effect we define the function $\mathcal{G}(y,t)$ to be

$$\mathcal{G}(y,t) = \mathcal{G}(y,t-\delta t)\left(1+\alpha\left(\frac{\frac{v_0}{2}-V(h,y,t-\delta t)}{\frac{v_0}{2}}\right)\right), \tag{10.4}$$

where α depends on the viscosity of the asthenosphere. In the current work a value of 0.1 is chosen.

10.3 Adaptive Mesh

The geometry of the fault is such that $\frac{w}{h} \ll 1$ and this creates a boundary layer of thickness $\approx 100m$ at the base of the fault in which the velocity and the stresses vary rapidly. To cope with this we use a refined grid along the base of the domain. Additionally, the solution in the tectonic plate varies more significantly in the vicinity of the fault with less variation nearer L. To reduce the computational cost we apply two mesh refinements in vertical regions adjacent to the fault. The first has the same dimensions as the fault and the second has a width of the order of $1km$ in order to bridge the gap between the refined mesh and the coarser grid spacing at larger distances. This mesh is time independent and is used for all time steps.

In order to resolve the curvature of the elasto-plastic boundary we apply an additional variable mesh refinement around this region. The refinement is set to extend a distance equal to the thickness of the boundary layer above and below the elasto-plastic boundary and uses the same refined grid spacing within this region. A representative mesh is shown in Figure 10.2 which is not drawn to scale. The width of the fault and tectonic plates are stretched to be of equal width. The mesh

refinements are also expanded in order to make the diagram clearer.

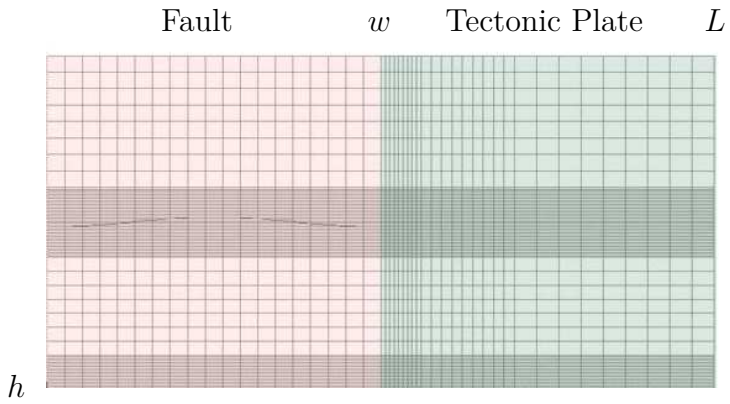

Figure 10.2: A representative mesh used for the discretisation of the domain. The fault region is shown in red and the tectonic plate is coloured green.

Chapter 11

Numerical Results

We present now the results obtained from the Matlab code discussed in the previous chapters. Section 11.1 discusses the velocity solutions and Section 11.2 presents the results for the stress field. The accumulated strains are demonstrated in Section 11.3.

11.1 The Velocity Field

The velocity field within the tectonic plate is shown in Figures 11.1 and 11.2 at every tenth time step. The times corresponding to each timestep are given in Table 11.1 and the plots are arranged chronologically from left to right on each row and from top to bottom. The first plot in Figure 11.1 suggests that the initial basal velocity is much too large and subside until about $t = 30$years. The first two plots in Figure 11.1 have approximately zero velocity on the left hand side, which is at $y = w$, as shown by the dark blue colour. These coincide with a fault being entirely within its elastic phase. Figures 11.3 and 11.4 shows the corresponding velocity in the fault and as can be seen the zero velocity boundary condition imposed on $y = 0$ is dominating the behaviour at early times. Between 25 and 30 years the base of the fault reaches yield, the material begins to flow more readily and this leads to a substantial increase in the velocity at the lower right corner of the fault; shown in the third plot of Figure 11.3. This consequently allows a dramatic increase in the velocity at the lower left corner of the tectonic plate.

As time progresses the region of the fault that is in yield expands and allows more of the fault material to move at larger velocities. By the second plot in Figure 11.2, corresponding to $t = 109.8$years, the base of the tectonic plate has reached the desired far field velocity of $\frac{v_0}{2}$ and the non-dimensional velocity plotted in the Figures 11.1 and 11.2 is approximately equal to 1.

By about 150 years the velocity at the lower right hand corner of the tectonic plate is beginning to exceed 1 rather than plateaux at this value. The probably cause is the far field strain-rate γ which is chosen to be a constant with depth. The value of γ is taken from surface measurements and is only required near the surface. Choosing a constant value with depth was merely the simplest choice in the absence of real data. A more suitable boundary condition for the model might come in the form of a Robin condition in which the strain-rate decreases as the velocity approaches $\frac{v_0}{2}$.

Table 11.1: The time in years corresponding to each tenth time step at which the variables are plotted in this chapter.

time step	10	20	30	40	50	60	70
t	23.4	24.7	31.0	41.5	56.0	73.3	91.5
time step	80	90	100	110	120	130	140
t	109.8	126.4	141.1	153.6	163.8	170.5	175.5

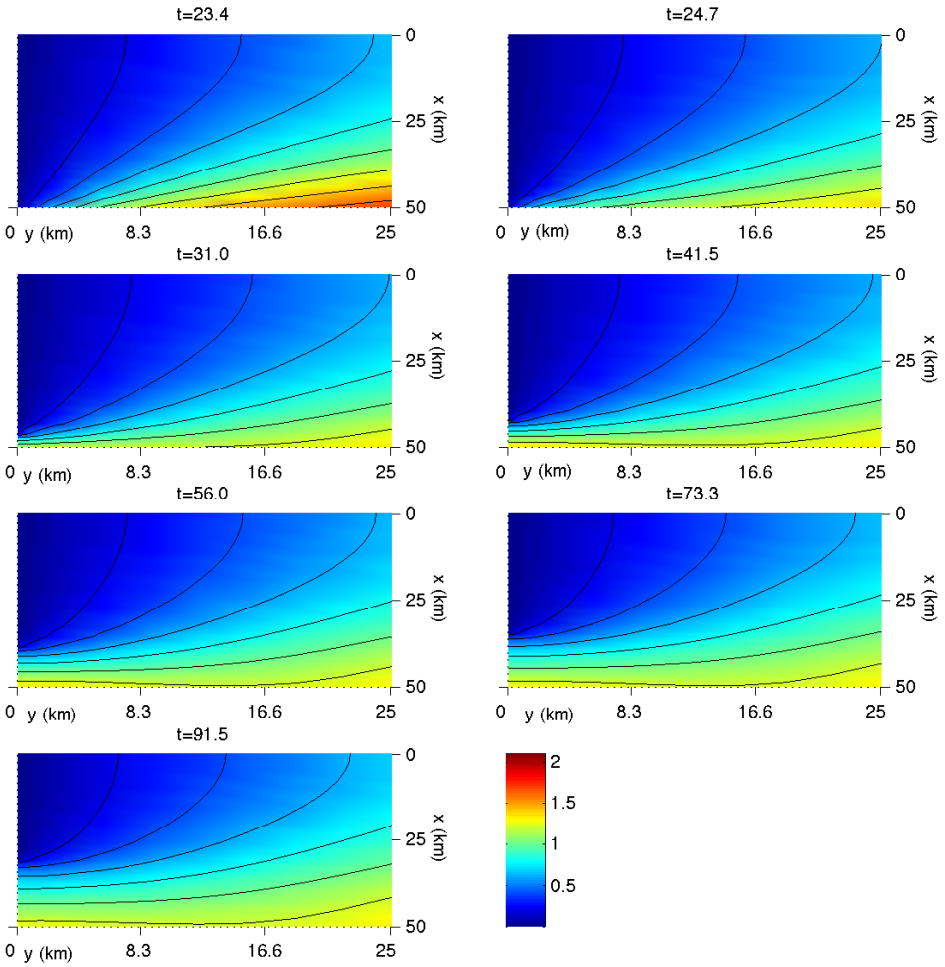

Figure 11.1: The velocity field, non-dimensionalised by the far field velocity $\frac{v_0}{2}$, within the tectonic plate at times $t = 23.4, 24.7, 31.0, 41.5, 56.0, 73.3, 91.5$ corresponding to the first line of Table 11.1.

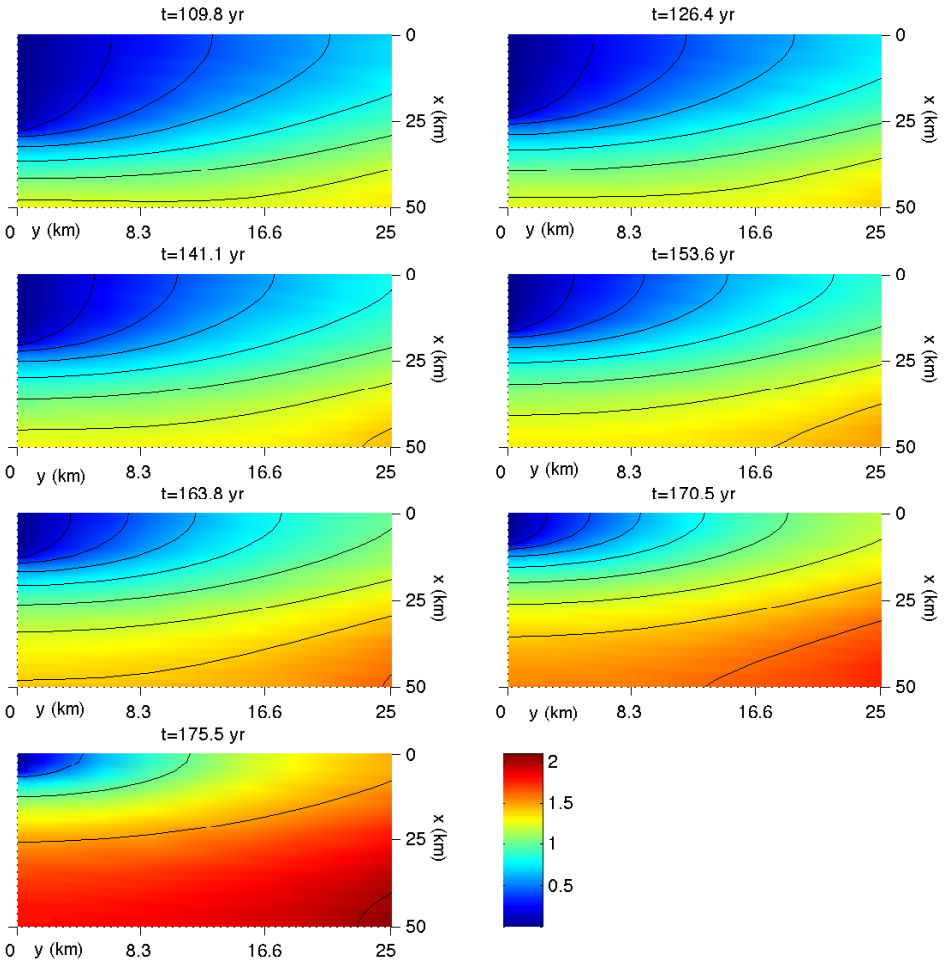

Figure 11.2: The velocity field, non-dimensionalised by the far field velocity $\frac{v_0}{2}$, within the tectonic plate at times $t = 109.8, 126.4, 141.1, 153.6, 163.8, 170.5, 175.5$ corresponding to the second line of Table 11.1.

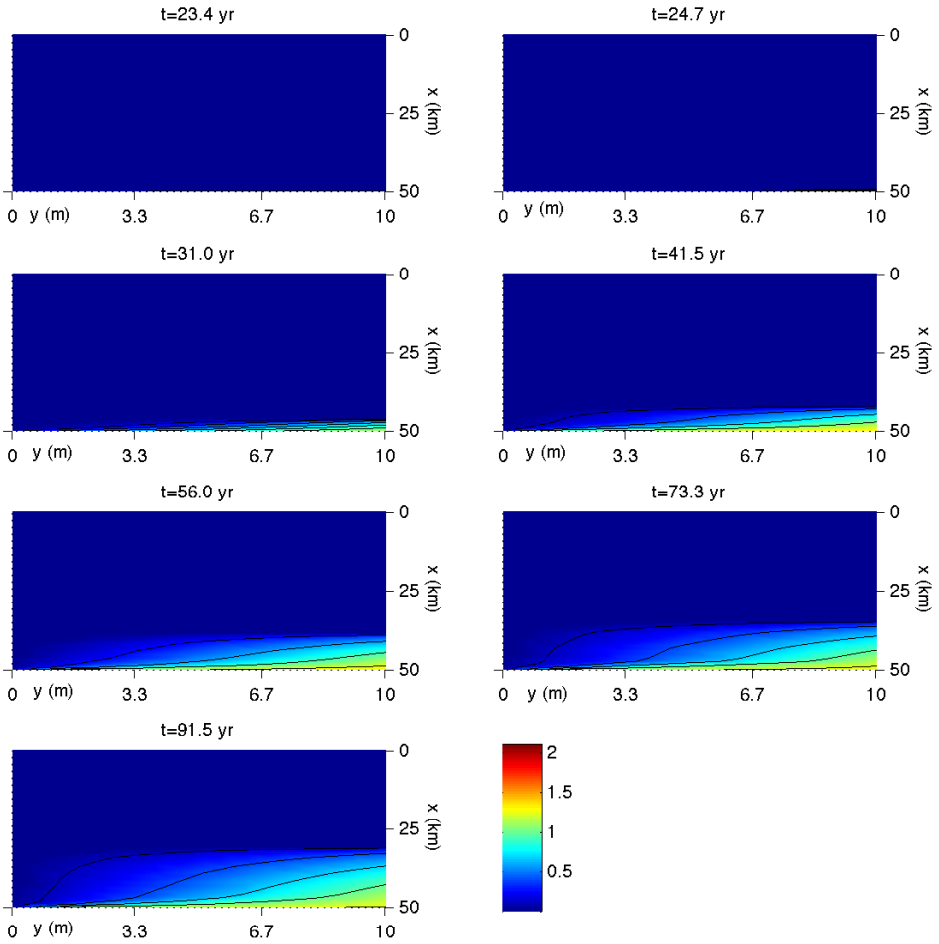

Figure 11.3: The velocity field, non-dimensionalised by the far field velocity $\frac{v_0}{2}$, within the fault at times $t = 23.4$, 24.7, 31.0, 41.5, 56.0, 73.3, 91.5 corresponding to the first line of Table 11.1.

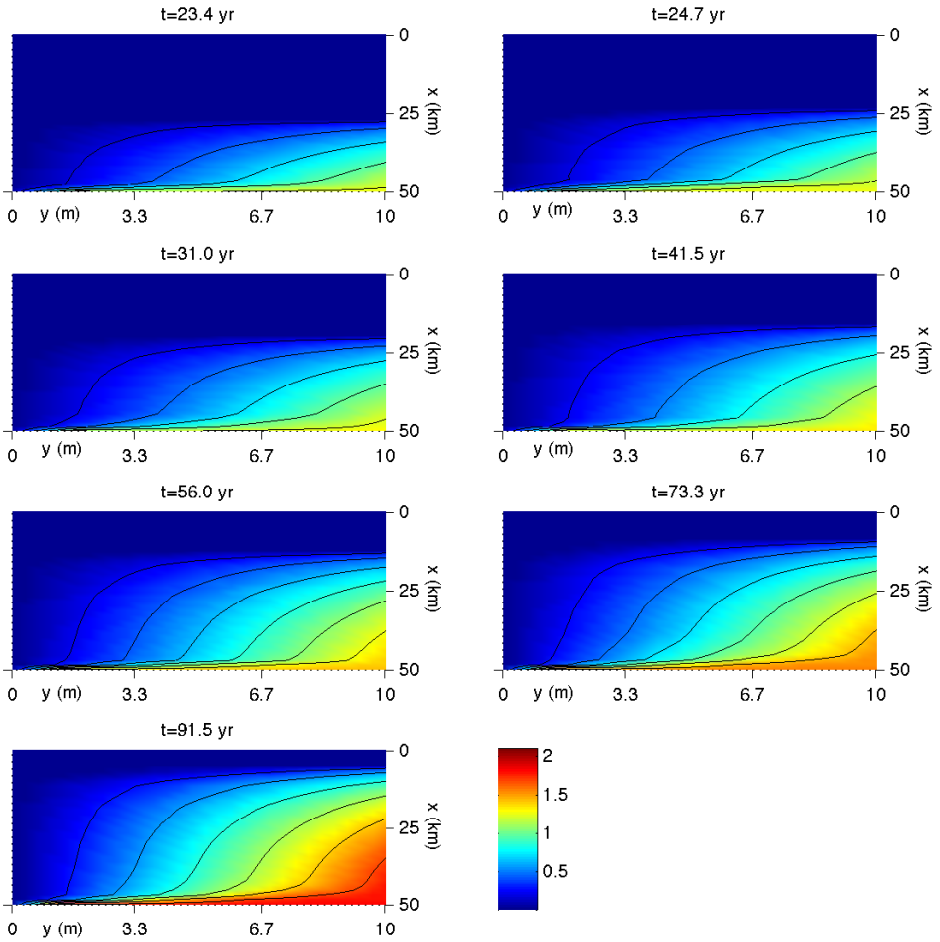

Figure 11.4: The velocity field, non-dimensionalised by the far field velocity $\frac{v_0}{2}$, within the fault at times $t = 109.8$, 126.4, 141.1, 153.6, 163.8, 170.5, 175.5 corresponding to the second line of Table 11.1.

The intention behind the definition of the $\mathcal{G}$ given by (10.4) is to decrease to zero once the basal velocity reaches a steady value of $\frac{v_0}{2}$. Figure 11.6 shows the variation in $\mathcal{G}$ at the same times as the basal velocities in Figure 11.5. It can be seen that at the value of $\mathcal{G}$ decreases with increasing time, as the velocity approaches $\frac{v_0}{2}$ at about 100 years, shown by the dashed lines. At subsequent time steps the non-dimensional velocity increases towards the value 2, as previously

discussed, rather than the desired value of 1. The effect of the fault reaching yield, however, does lead to the basal velocity reaching a value which is approximately independent of y. This can be seen by the almost horizontal nature of the plots in Figure 11.5 for $t > 30$. This means at depth that the velocity of the tectonic plate is less affected by the zero velocity in the fault

The cause of the peak in $\mathcal{G}$ at each time step at distances close to w is caused by the asthenosphere tring to force the base of the fault to move. As $\mathcal{G}$ increases here, it forces the velocity to increase locally and this subsequently increases the velocity at further distances. This consequently decreases $\mathcal{G}$ accordingly.

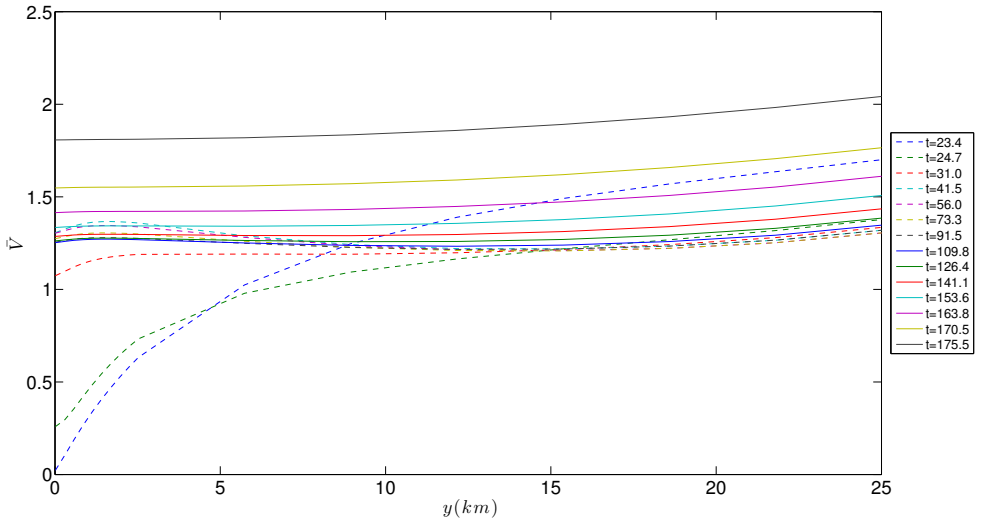

Figure 11.5: The non-dimensional basal velocity plotted against y. Several plots are presented for a variety of times after the base of the fault reaches yield.

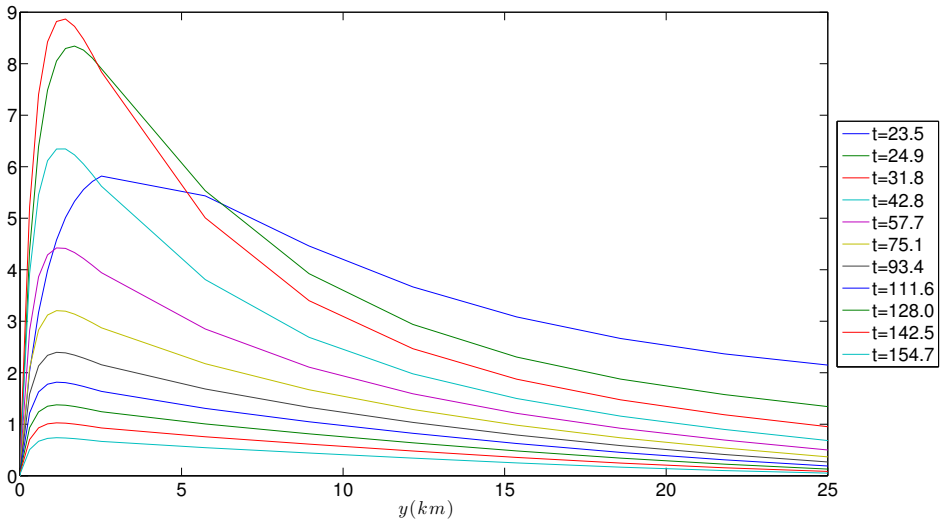

Figure 11.6: The evolution of $\mathcal{G}$ with time after the onset of plastic deformation in the fault.

11.2 The Stress Field

Figure 11.7 shows the speed of progression of the elasto-plastic boundary. For approximately 23 years the entire fault remains elastic as the stresses accumulate towards satisfying equality in the yield criterion. Immediately after the onset of plastic deformation the elasto-plastic boundary increases rapidly up to a speed of $1kmyr^{-1}$ at about 25 years. After this time the speed decays. The effect of this decreasing speed is an increase in the stress increment as the peak in $\dot{\sigma}_{13}$ and $\dot{\sigma}_{23}$ has a more profound effect on each point through which the boundary sweeps during a time step. This is demonstrated the darker red colour in Figure 11.13 which corresponds to the minimum in the speed of the elasto-plastic boundary between 40 and 130 years.

From about 150 years the elasto-plastic boundary begins to speed up, reaching nearly $1.4kmyr^{-1}$. A possible explanation for this is that the cohesion in the yield criterion decays too rapidly with depth so that the value of k in (5.34) is too low around $5-10km$. A more gradual decay of the cohesion with depth would increase the value of k and therefore slow the progression of the elasto-plastic boundary

and lead to an increase in the stress increment. An alternative explanation is that this progression is indicative of an earthquake instigation. Figure 11.4 shows that the velocity increases rapidly with depth below the elasto-plastic boundary and reaches an approximate constant value. The rate at which the velocity in the fault increases from its low elastic value to the $O\left(\frac{v_0}{2}\right)$ value during the plastic phase is determined by the speed of progression of the elasto-plastic boundary. Consequently, the acceleration increases as the elasto-plastic boundary increases its speed of progression and this could lead to an invalidation of the quasi-static approximation and produce a dynamic earthquake event.

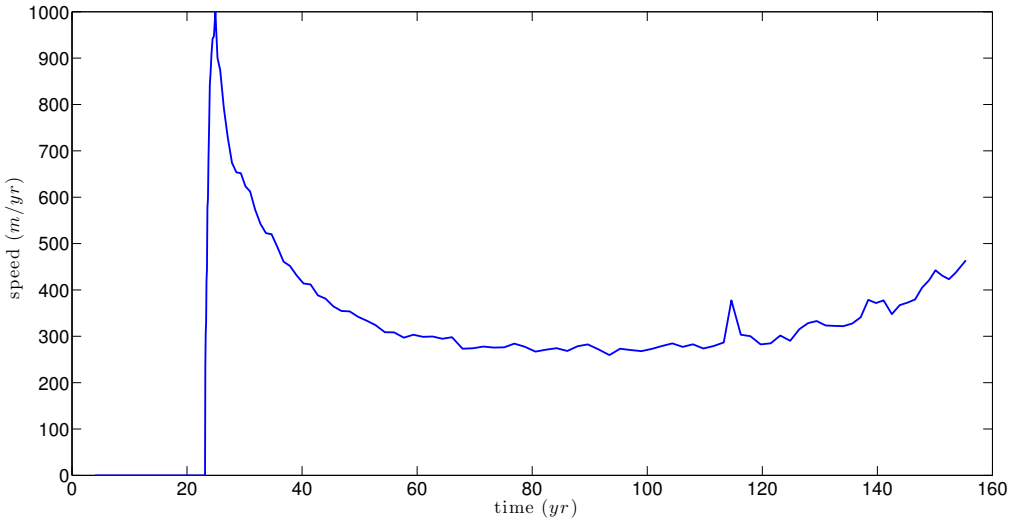

Figure 11.7: The speed of propagation of the elasto-plastic boundary with time.

Figures 11.8 through to 11.11 show the stresses accumulating in the tectonic plate. The increase in σ_{13} is mainly focused at $y = w$ at the base of the tectonic plate and is a result of the peaks in $\mathcal{G}$ shown in Figure 11.6. At further distances the stress reaches a value which is approximately independent of the position in the y direction as shown by the green colour. This is consistent with the tectonic plate approaching a steady state in the far field.

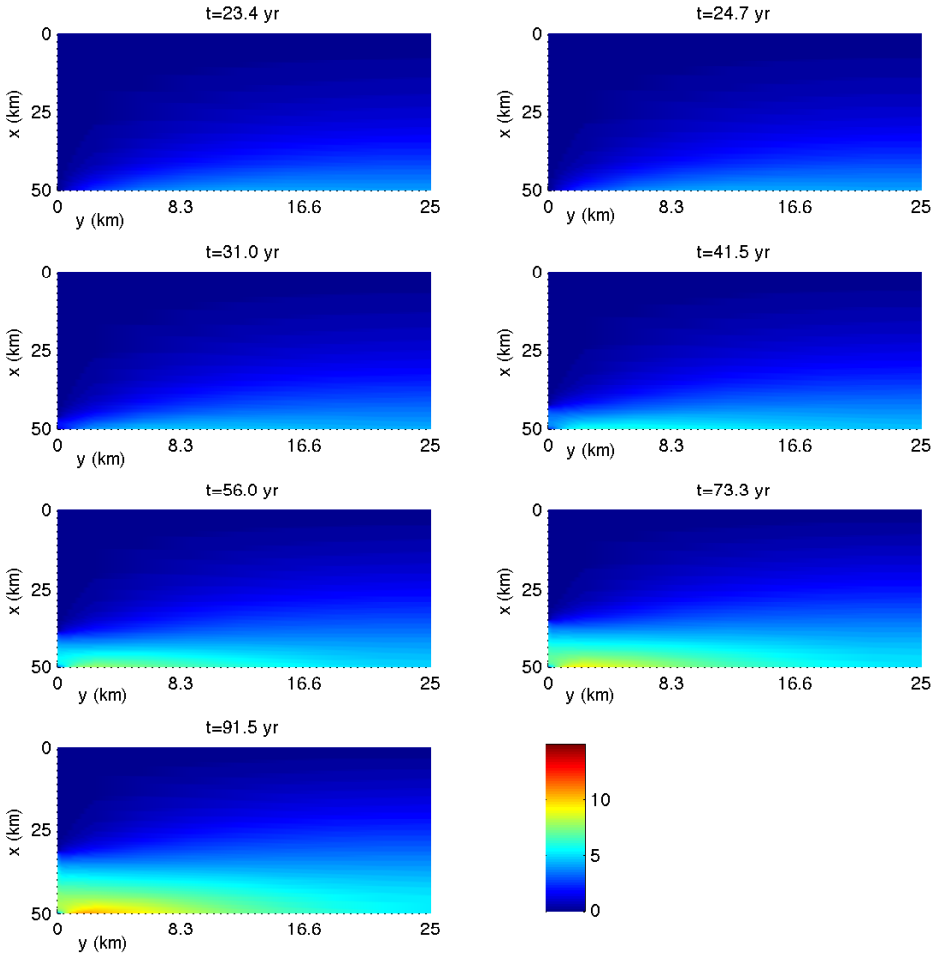

Figure 11.8: The accumulation of σ_{13} in *kbar* within the tectonic plate at times $t = 23.4, 24.7, 31.0, 41.5, 56.0, 73.3, 91.5$ corresponding to the first line of Table 11.1.

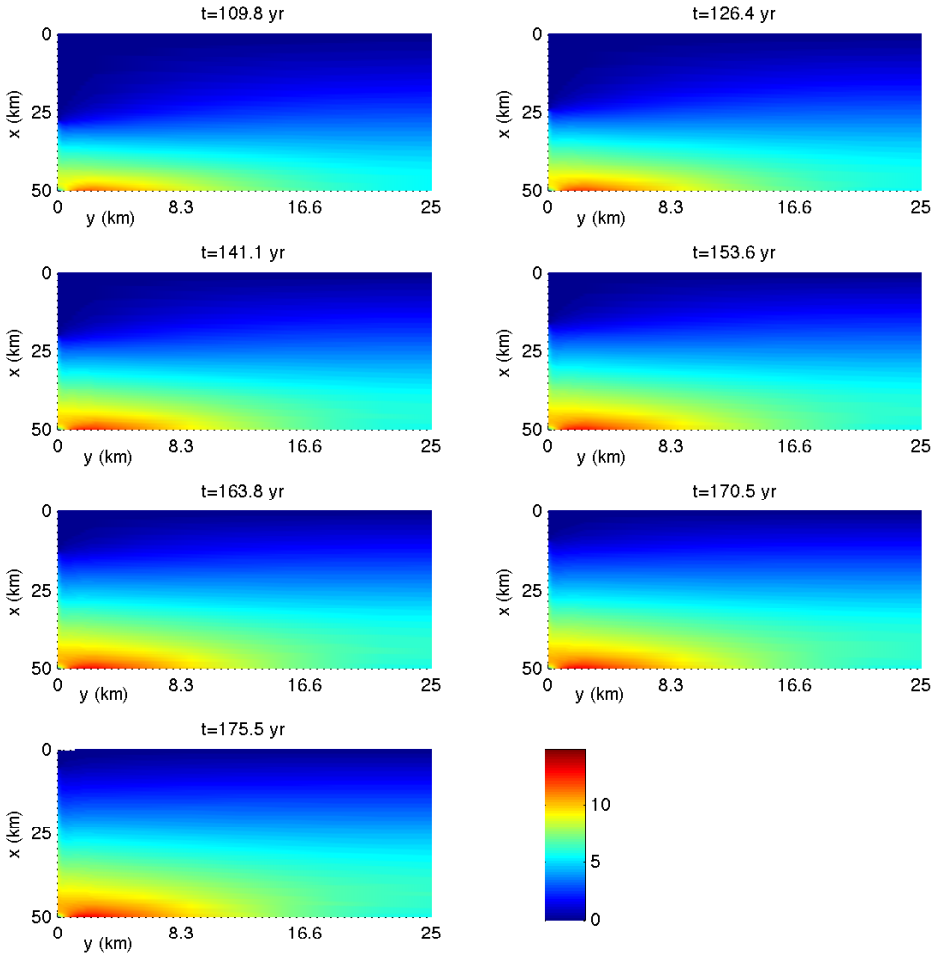

Figure 11.9: The accumulation of σ_{13} in *kbar* within the techtonic plate at times $t = 109.8, 126.4, 141.1, 153.6, 163.8, 170.5, 175.5$ corresponding to the second line of Table 11.1.

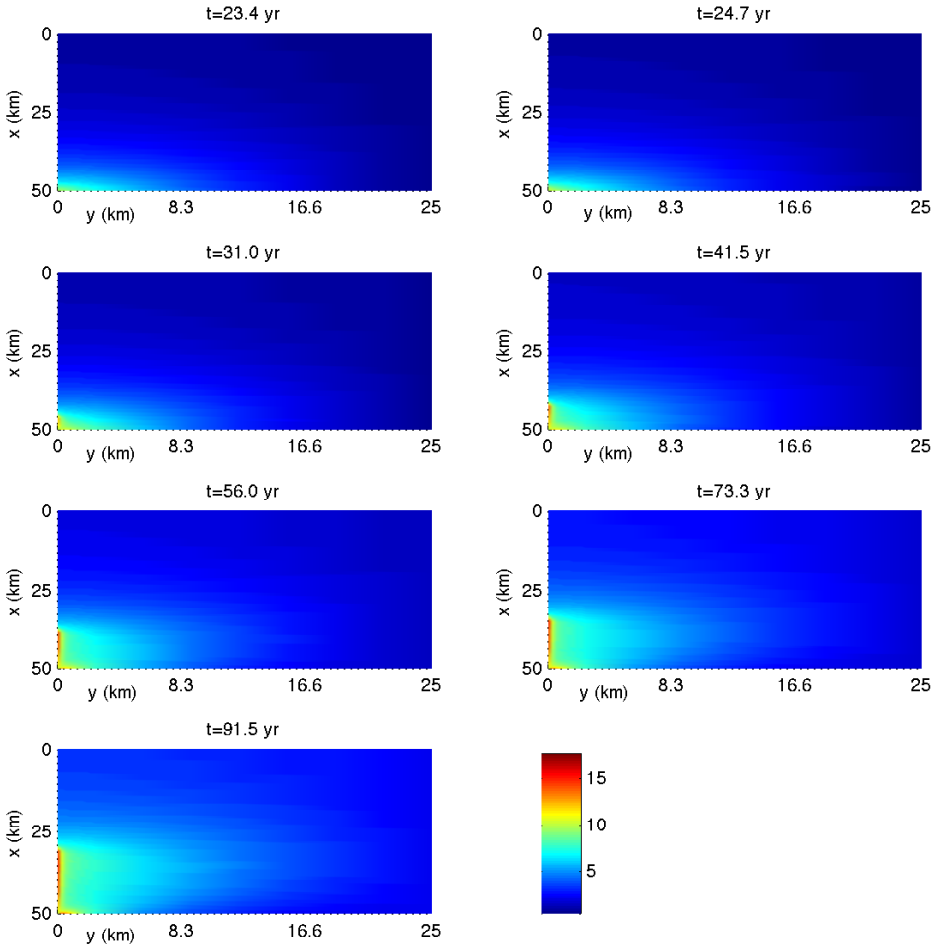

Figure 11.10: The accumulation of σ_{23} in *kbar* within the tectonic plate at times $t = 23.4, 24.7, 31.0, 41.5, 56.0, 73.3, 91.5$ corresponding to the first line of Table 11.1.

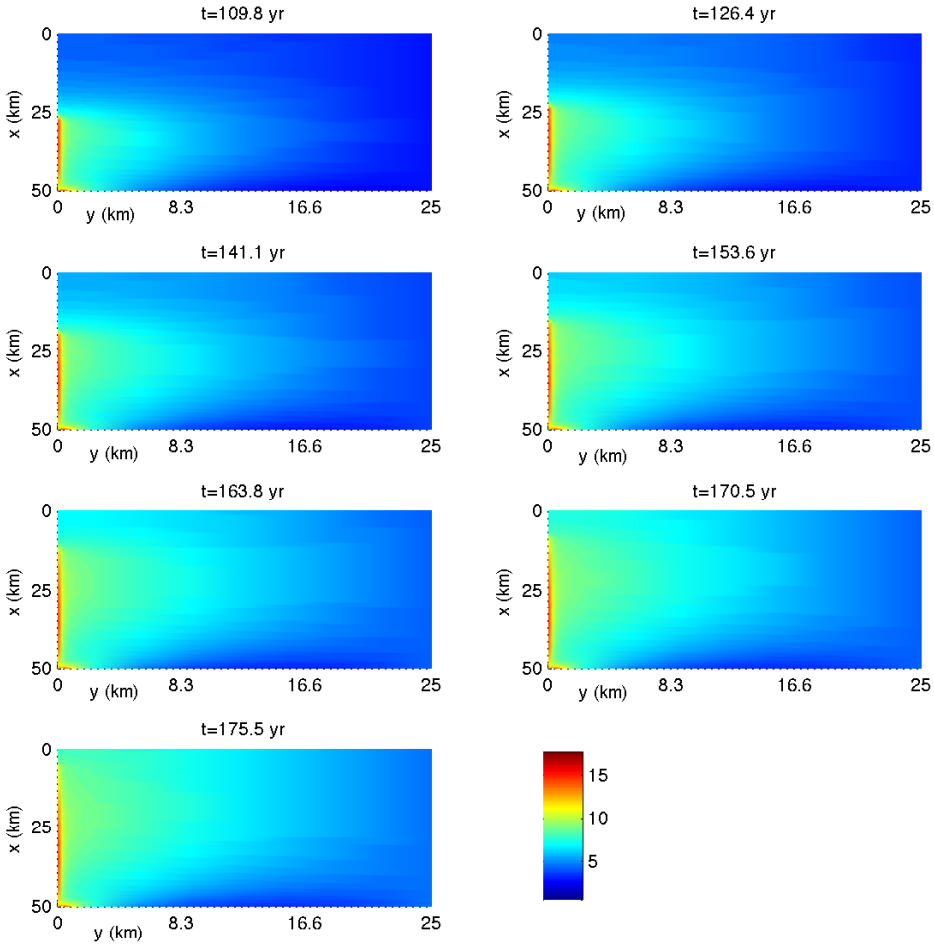

Figure 11.11: The accumulation of σ_{23} in *kbar* within the techtonic plate at times $t = 109.8, 126.4, 141.1, 153.6, 163.8, 170.5, 175.5$ corresponding to the second line of Table 11.1.

The increase in σ_{23} is similarly focused on $y = w$ with the stresses at the base of the plate increasing 5-fold over the initial 30 years. Figures 11.12 and 11.13 show that the stress in the fault, and subsequently the left edge of the tectonic plate, reaches a fairly constant value. This is seen by the red area in the later plots. These red areas correspond to the plastically behaving material in the fault and implies that the stress increases rapidly in the initial stages of plastic flow but then the stress-rates drop subsequently to leave an approximately constant value of σ_{23}. In the tectonic plate the value of σ_{23} demonstrates this phenomenon further by the growing red region at the lower region of the edge of the fault, the shade of which is approximately even.

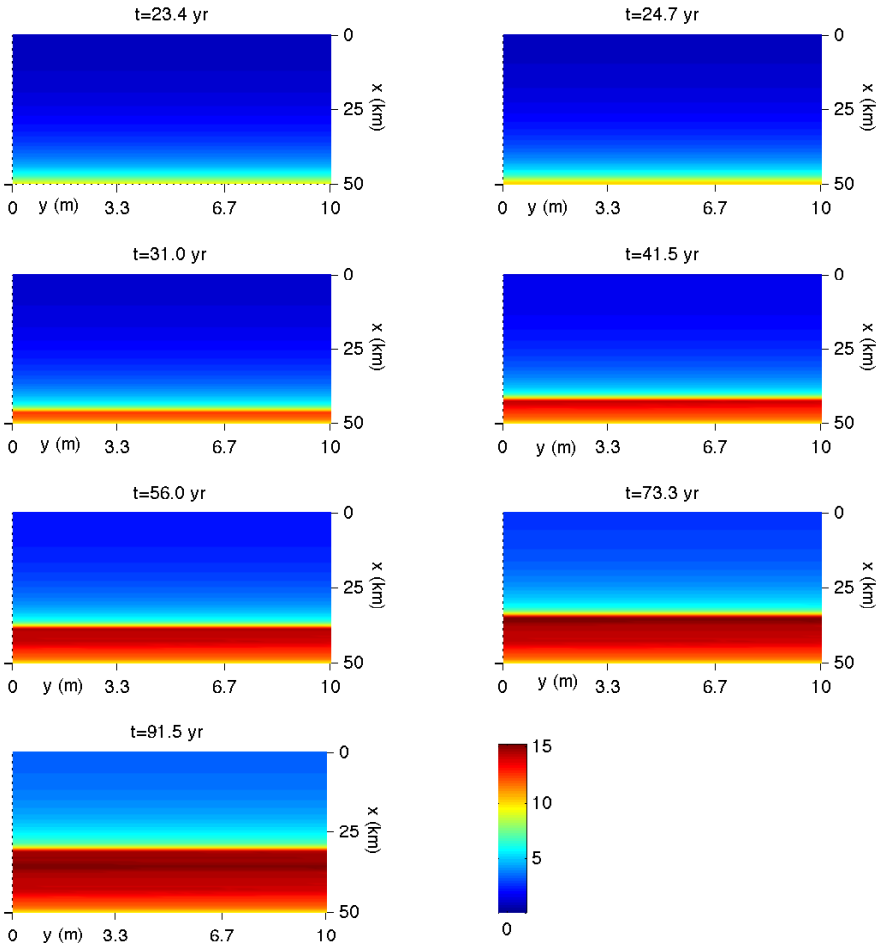

Figure 11.12: The accumulation of σ_{23} in *kbar* within the fault at times $t = 23.4$, 24.7, 31.0, 41.5, 56.0, 73.3, 91.5 corresponding to the first line of Table 11.1.

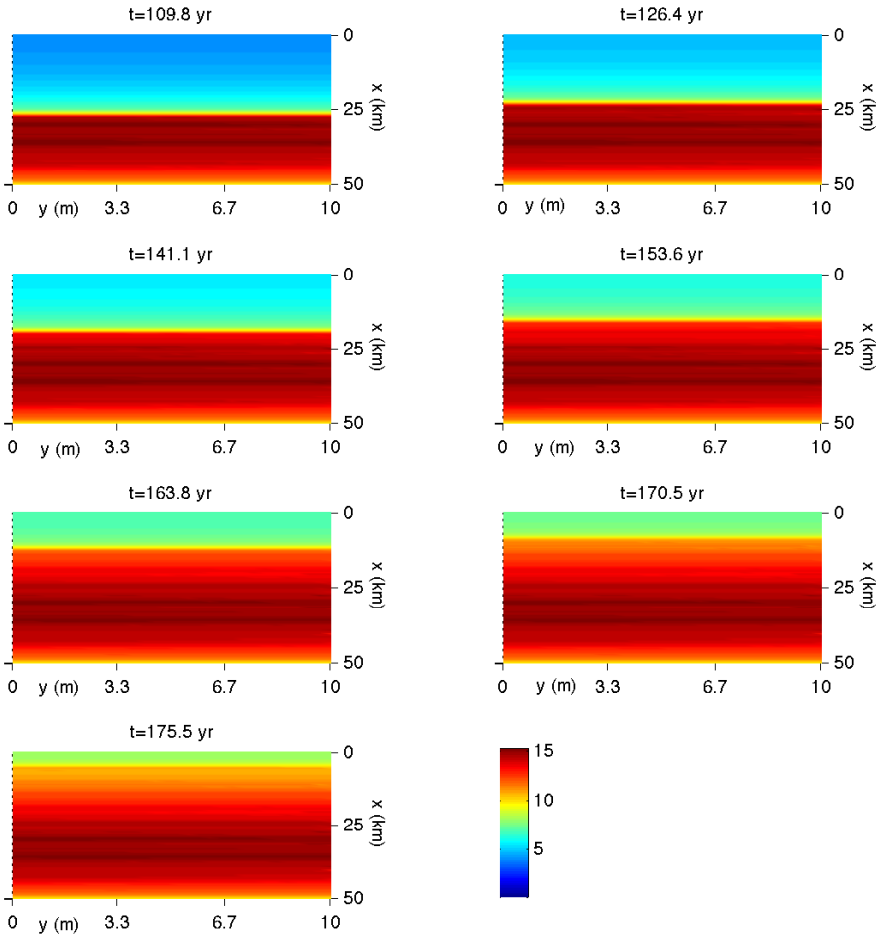

Figure 11.13: The accumulation of σ_{23} in $kbar$ within the fault at times $t = 109.8$, 126.4, 141.1, 153.6, 163.8, 170.5, 175.5 corresponding to the second line of Table 11.1.

The stress component σ_{13} in the fault is shown in Figures 11.14 and 11.15. It accumulates at the edge of the fault with zero values at the center of the fault. A maximum value of $0.2kbar$ is achieved which is an order of magnitude less than the stress component σ_{23} shown in Figures 11.12 and 11.13.

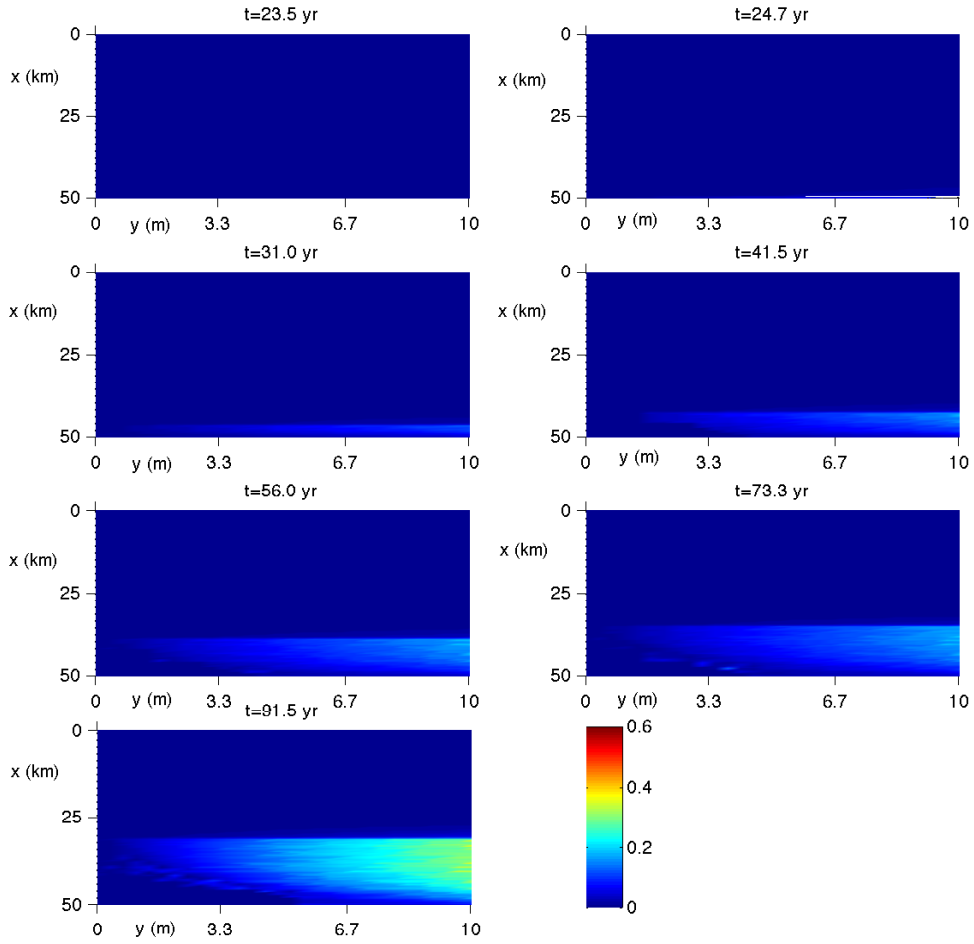

Figure 11.14: The accumulation of σ_{13} in *kbar* within the fault at times $t = 23.4$, 24.7, 31.0, 41.5, 56.0, 73.3, 91.5 corresponding to the first line of Table 11.1.

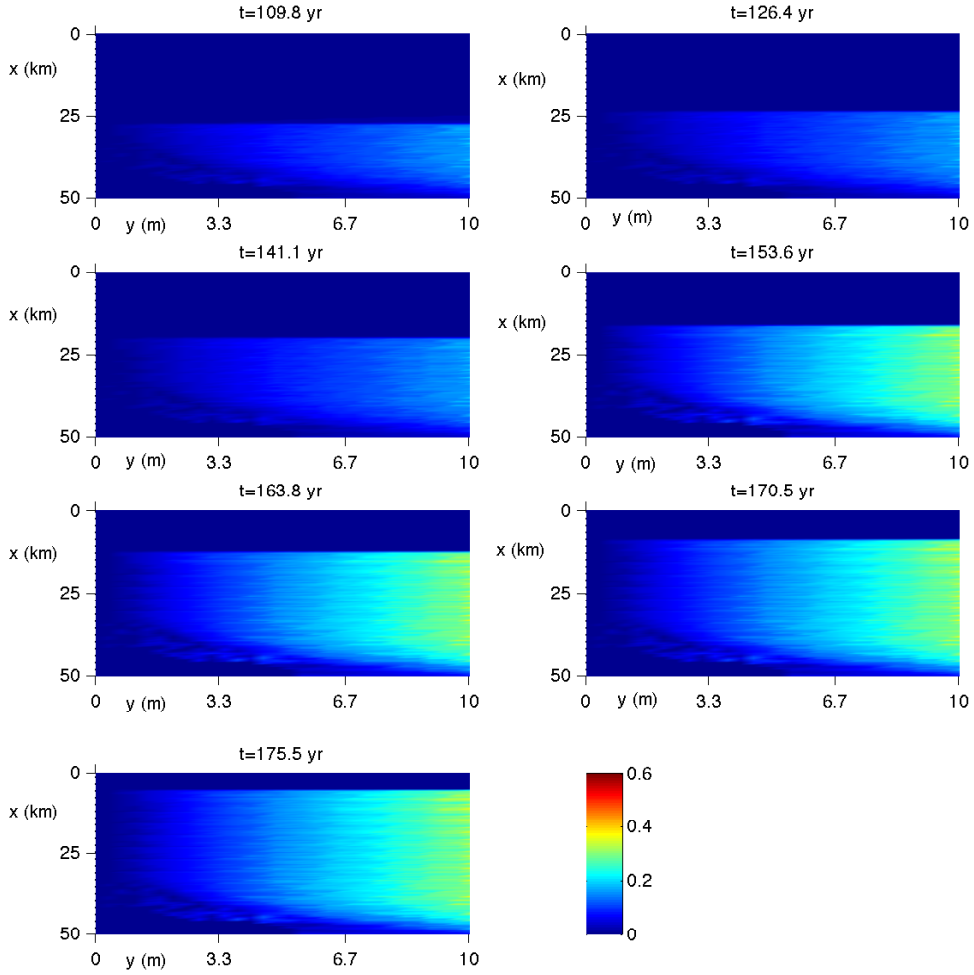

Figure 11.15: The accumulation of σ_{13} in *kbar* within the fault at times $t = 109.8$, 126.4, 141.1, 153.6, 163.8, 170.5, 175.5 corresponding to the second line of Table 11.1.

11.3 The Strains

Since the elastic strains are proportional to the stresses, plots for the strains are not presented but are qualitatively demonstrated by Figures 11.8 through to 11.11 and are rescaled by dividing by the value of the shear modulus in kbar, namely 500, to give a colour bar ranging from 0 to $0.03kbar$. The strain, ϵ_{13}, therefore accumulates significantly at the lower left corner of the tectonic plate, reaching an approximately constant value of $0.03kbar$ as shown by Figure 11.11. During an earthquake the elastic strains are released and should have ideally accumulated prodominantly at a depth of $10km$ where the hypocenter lies. The strain component, e_{23}, does accumulate a little near the surface of the tectonic plate near the fault as shown by the turquoise colour which represents a value of 3×10^{-5}. It mostly builds up, however, immediately next to the fault at lower depths.

The plastic strains are shown in Figures 11.16 through to 11.19. All figures show an accumulation at the base of the fault where the temperatures are larger and the rock becomes more ductile which facilitates the plastic deformation. The strains, ϵ^p_{13}, in Figures 11.16 and 11.17 are three orders of magnitude less than ϵ^p_{23} in Figures 11.18 and 11.19. The strain, ϵ^p_{23}, builds up at the base of the center of the fault where the velocity is fixed at zero, as shown on the left edge of plots 4 to 6 of Figure 11.18. This causes large velocity gradients as the velocity increases rapidly up to the $O\left(\frac{v_0}{2}\right)$ at the edge of the fault. The strains at this corner become dominated by the overall strain lower in the fault at later times as the strains approach a constant value below $30km$.

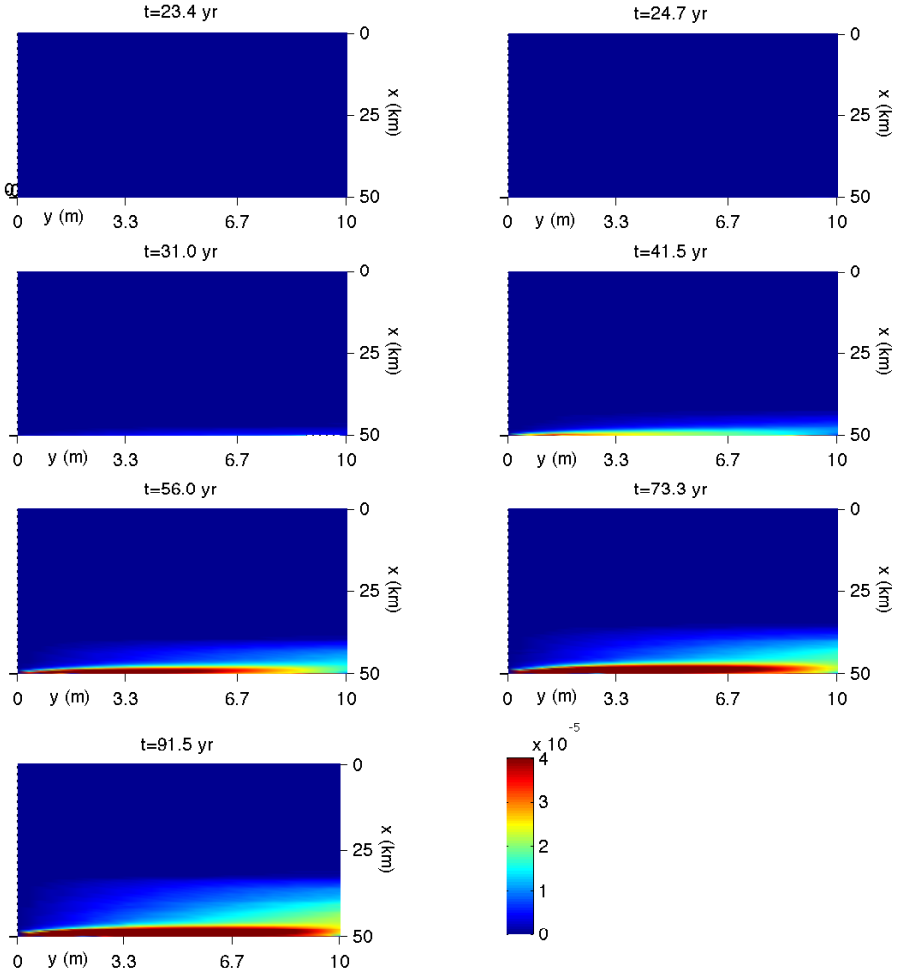

Figure 11.16: The accumulation of the plastic strain ϵ^p_{13} in the fault at times $t = 23.4$, 24.7, 31.0, 41.5, 56.0, 73.3, 91.5 corresponding to the first line of Table 11.1.

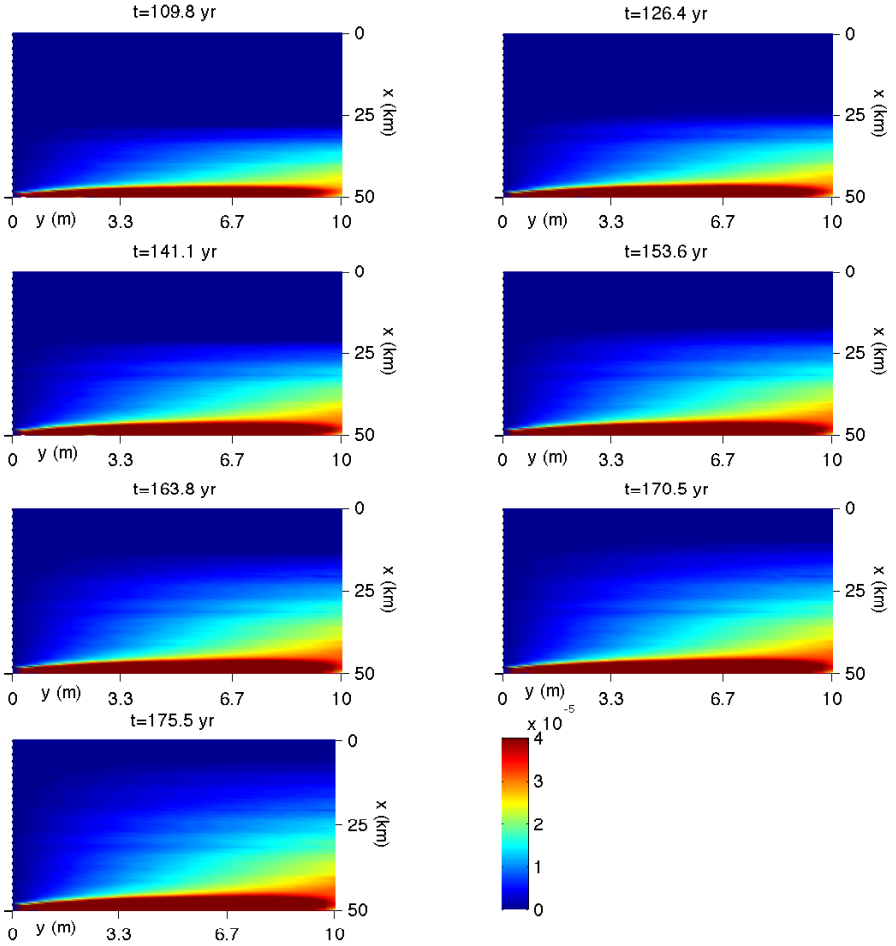

Figure 11.17: The accumulation of ϵ^p_{13} in the fault at times $t = 109.8$, 126.4, 141.1, 153.6, 163.8, 170.5, 175.5 corresponding to the second line of Table 11.1.

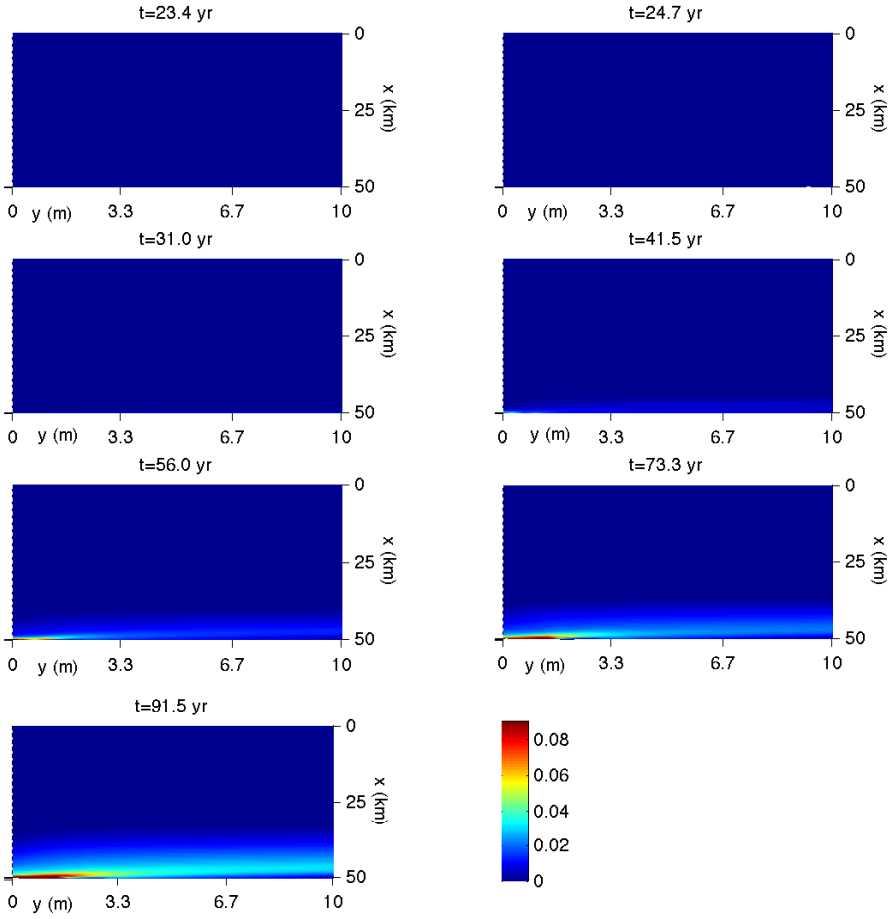

Figure 11.18: The accumulation of the plastic strain ϵ^p_{23} in the fault at times $t = 23.4, 24.7, 31.0, 41.5, 56.0, 73.3, 91.5$ corresponding to the first line of Table 11.1.

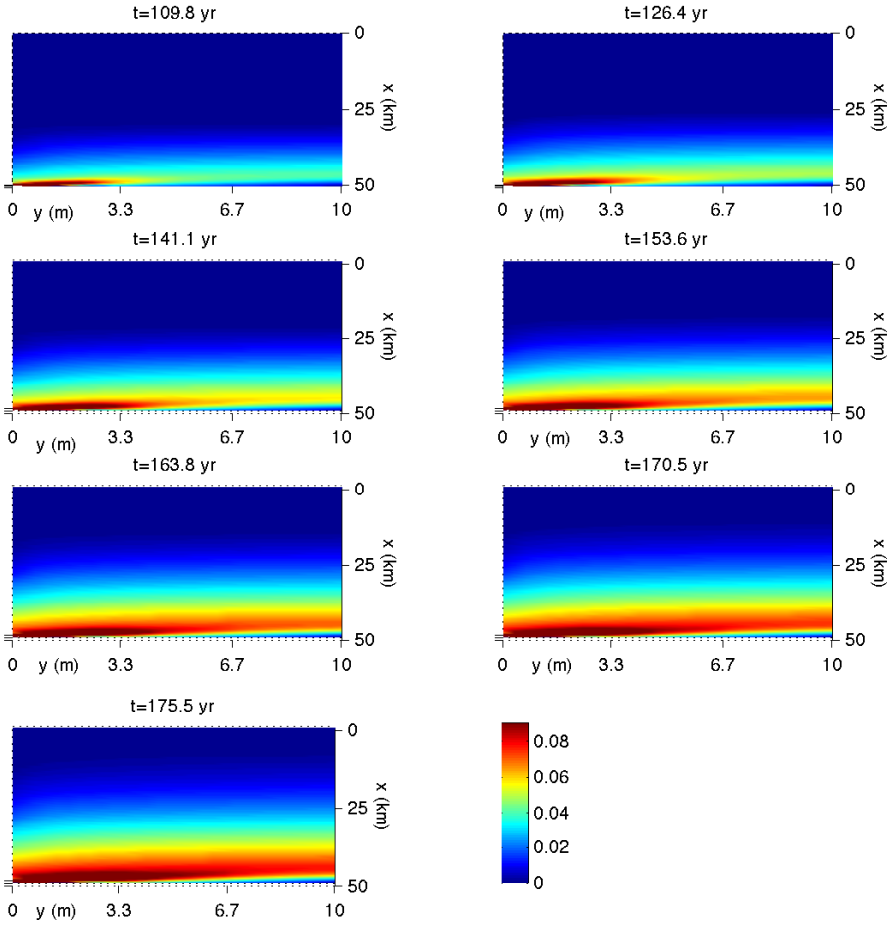

Figure 11.19: The accumulation of ϵ^p_{23} in the fault at times $t = 109.8$, 126.4, 141.1, 153.6, 163.8, 170.5, 175.5 corresponding to the second line of Table 11.1.

Chapter 12

Conclusions

A model for stress and strain accumulation in strike-slip earthquake fauls has been presented. It develops the work by Rowshandel and Nemat-Nasser [1986] to include a finite width fault. The finite width of the fault allows $O\left(\frac{v_0}{2}\right)$ velocities on its edge while remaining stationary at its center.

The velocity field discussed in Chapter 11 shows some similarities with reality. The velocity at the base of the tectonic plate reaches a state which is independent of the distance from the fault. This implies that the motion at depth is less dependent on the zero velocity at the center of the fault. At shallower depths where the fault is still deforming elastically the velocity at the edge of the fault is much less than the far field velocity and as a result the velocity in the tectonic plate is highly dependent on y.

At the lower right corner of the tectonic plate the velocities exceed the desired value of $\frac{v_0}{2}$ despite the value of $\mathcal{G}$ simultaneously decaying to zero. The cause is most likely due to the far field strain-rate which was assumed to be constant with depth. This has the effect of continuing to force the tectonic plate even once it reaches $\frac{v_0}{2}$. A more suitable boundary condition may come in the form of a Robin condition which, like $\mathcal{G}$, decays to zero as the velocity approaches $\frac{v_0}{2}$. This is left for future work.

The stresses and strains accumulate predominantly below the position of the elasto-plastic boundary. It is therefore unlikely that an earthquake would occur in the elastic region of the fault and an earthquake should be instigated by a feature

of the plastic behaviour. An analogous trigger to the friction models of Rice and Simons [1976] and Scholtz [1990] is that the pressure dependent term in the work hardening parameter k, (5.34), suddenly drops in value to immitate a change from static to dynamic friction. The work hardening depends on the plastic strains, however, which accumulate at the base of the fault and therefore are unlikely to lead to an earthquake hypocenter at the correct depth.

One alternate possibility is that the increase in speed of progression of the elasto-plastic boundary at shallower depths creates significant acceleration of the fault material and tectonic plate. If these accelerations become large enough that a quasistatic approximation is not valid then the inertia terms would need to be reintroduced into the governing equations and this in turn could lead to a velocity that increases more rapidly than the current model can predict. This could be described as an earthquake.

Another possibility is that the cohesion decays too rapidly wih depth. A steep increase in the value of k at deeper depths could prevent the elasto-plastic boundary from accelerating towards the surface. A slower progression of this boundary would lead to an accumulation of the stresses locally and if this occurred at about $10km$ below the surface could give a more realistic stress and strain field. An investigation into the effects of the cohesion is left for future work.

Chapter 8 presented a novel method for applying the finite difference method to domains with curved boundaries. This utilises an interpolation-extrapolation method applied to points outside the domain in order to maintain the standard finite difference templates. The advantages are that it does not affect the simplicity of the finite difference scheme templates and the same code can be applied to all points in the vicinity of the boundary regardless of the gradient and position of the boundary. The convergence plots presented show that the method is robust for a range of curved boundaries which range from approximately horizontal to those which span a third of the height of the domain. In all cases the convergence of the second order accurate finite difference scheme in which the method is embedded is unaffected and the numerical solution converges quadratically to the analytical solution derived in Chapter 6.

Chapter 9 resolves the singular stress-rate field encountered at the end of the elasto-plastic boundary. At this point the solution varies too rapidly to be resolved

by a reasonably dense mesh and asymptotic expansions are derived for the solution which capture this singular nature. A new method of incorporating this asymptotic solution into a finite difference scheme is presented which removes the singularity from the finite difference scheme in an elliptical region surrounding the corner. The method does not involve intensive mesh refinements of other methods applied to similar problems in fluid mechanics.

The method does not, however, seem to be applicable at the base of the edge of the fault where similar singularities occur. The problem arises that the equation that determines the eigenvalues, (9.42), does not have any solutions less than one which are required for singular stresses. This is most likely due to the form of the asymptotic approximations used to simplify the governing equations. It is assumed that all variables vary in the order of $O(\epsilon)$ near the corner which was chosen as the simplest possibility. Perturbations to the stresses of the form $O(\epsilon^n)$ for $n \neq 1$ may resolve the problem and is left for future work.

Bibliography

R. P. Agarwal and D. O'Regan. *Ordinary and Partial Differential Equations*. Springer, 2009.

Y. Caristan. The transition from high temperature creep to fracture in maryland diabase. *Journal of Geophysical Research*, 87(B8):6781–6790, August 1982.

W. M. Coombs and R. S. Crouch. Non-associated reuleaux plasticity: Analytical stress integration and consistent tangent for finite deformation mechanics. *Computer Methods in Applied Mechanics and Engineering*, 200(9-12):1021–1037, February 2010.

R. Courant and D. Hilbert. *Methods of Mathematical Physics*, volume II. Interscience Publishers, 1962.

B. Doran, H. O. KöKsal, Z. Polat, and C. Karakoc. The use of "Drucker-Prager criterion" in the analaysis of reinforced concrete members by finite elements. *Technical Journal of Turkish Chamber of Civil Engineers*, 98:489–493, December 1998.

A. Drescher and G. de Josselin de Jong. Photoelastic verification of a mechanical model for the flow of a granular material. *Journal of the Mechanics and Physics of Solids*, 20:337–351, 1972.

D. C. Drucker and W. Prager. *Quart. Appl. Math*, 10:157, 1952.

W. M. Elsasser. Convection and stress propagation in the upper mantle. In Runcorn, editor, *The Application of Modern Physics to The Earth and Planetary Interiors*, pages 223–246, 1969.

J. M. Floryan and L. Czechowski. On the numerical treatment of corner singularity in the vorticity field. *Journal of Computational Physics*, 118:222–228, 1995.

P. L. Gould. *Introduction to Linear Elasticity*. Springer, 2nd edition edition, 1994.

K. F. Graff. *Wave Motion in Elastic Solids*. Dover Publications, 1991.

J. M. N. T. Gray, M. Wieland, and K. Hutter. Gravity-driven free surface flow of granular avalanches over complex basal topography. *Proc. R. Soc.*, 455(1985): 1841–1874, May 1999.

D. Harris. Plasticity models for soil, granular and jointed rock materials. *Journal of the Mechanics and Physics of Solids*, 40(2):273–290, 1992.

D. Harris. Constitutive equations for planar deformations of rigid-plastic materials. *Journal of the Mechanics and Physics of Solids*, 41:1515–1531, September 1993.

D. Harris. A unified formulation for plasticity models of granular and other materials. *Proceedings of the Royal Society*, 450(1938):37–49, 1995.

K. Hashiguchi and Y. Yamakawa. *Introduction to Finite Strain Theory for Continuum Elasto-Plasticity*. Wiley, 1st edition, 2012.

T. Hawa and Z. Rusak. Numerical-asymptotic expansion matching for computing a viscous flow around a sharp expansion corner. *Theoretical Computational Fluid Dynamics*, 15:265–281, 2002.

N. S. Heaps. Three-dimensional numerical model of the Irish sea. *Geophys. J. R. Astr. Soc*, 35:99–120, 1973.

H. C. Heard. Comparison of the flow properties of rocks at crustal conditions. *Philosophical Transactions of the Royal Society of London. Series A*, (283):173–186, 1976.

E. H. Hearn and R. Bürgmann. The effect of elastic layering on inversions of gps data for coseismic slip and resulting stress changes: Strike-slip earthquakes. *Bulletin of the Seismological Society of America*, pages 1637–1653, November 2005.

H. Hencky. *Zeits. ang. Math. Mech.*, 4:323, 1924.

H. J. Hermann, J. P. Hovi, and S. Luding, editors. *Non-Associated Plasticity for Soils, Concrete and Rock*, September 1997. NATO Advanced Study Institute, Kluwer Academic Publishers.

R. Hill. *The Mathematical Theory of Plasticity.* Clarendon Press, 1950.

L. M. Hocking. A moving fluid interface. part 2. the removal of the force singularity by a slip flow. *Journal of Fluid Mechanics*, 79:209–229, 1977.

G. W. Housner. A dislocation theory of earthquakes. Technical report, California Institute of Technology, 1953.

J. W. Hutchinson. Plastic stress and strain fields at a crack tip. *Journal of the Mechanics and Physics of Solids*, 16(5):337–342, September 1968.

S. Ivorra, R. Irles, L. Estevan, J. M. Adam, F. J. Pallarés, and B. Ferrer. Drucker-Prager yield criterion application to study the behaviour of cfrp confined concrete under compression. *In Proceedings of IAHS World Congress on Housing Science*, October 2010.

J. Jancar, A. T. Dibenedetto, and A. Dianselmo. Effect of adhesion on the fracture toughness of calcium carbonate-filled polypropylene. *Polymer Engineering and Science*, 33(9):559–563, May 1993.

L. Jing and J.A. Hudson. Numerical methods in rock mechanics. *International Journal of Rock Mechanics and Mining Sciences*, 39:409–427, 2002.

G. de Josselin de Jong. Statics and kinematics in the failure zone of a granular material. *Uitgeverij*, 1959.

J. F. Kennedy. The mechanics of dunes and anti-dunes in erodible-bed channels. *Journal of Fluid Mechanics*, 16(4):521–544, 1963.

W. T. Koiter. An infinite row of collinear cracks in an infinite elastic sheet. *Archive of Applied Mechanics*, 28:168–172, 1959.

P. V. Lade. Elasto-plastic stress-strain theory for cohesionless soil with curved yield surfaces. *International Journal of Solids and Structures*, 13(11):1019–1035, 1977.

F. K. Lehner, V. C. Li, and James R. Rice. Stress diffusion along rupturing plate boundaries. *Journal of Geophysical Research*, 86:6155–6169, July 1981.

V. C. Li and J. R. Rice. Crustal deformation in great California earthquake cycles. *Journal of Geophysical Research*, 92:11533–11551, October 1987.

Z. C. Li and T. T. Lu. Singularities and treatments of elliptic boundary value problems. *Mathematical Computer Modelling*, 31(8-9):97–145, April-May 2000.

M. Lisowski, J. C. Savage, and W. H. Prescott. The velocity field along the San Andreas fault in central and southern California. *Journal of Geophysical Research*, 96(B5):8369–8389, May 1991.

T. Liszka and J. Orkisz. The finite difference method at arbitrary irregular grids and its application in applied mechanics. *Computers and Structures*, 11:83–95, 1980.

M. M. Mehrabadi and S. C. Cowin. Initial planar deformation of dilatant granular materials. *Journal of the Mechanics and Physics of Solids*, 26(4):269–284, August 1978.

J. Melosh. Shear stress on the base of a lithosphereic plate. *Pure and Applied Geophysics*, 115(1-2):429–439, 1977.

N. I. Muskhelishvili. *Some Basic Problems of the Mathematical Theory of Elasticity*. P. Noordhoff Ltd, 1953.

S. Nemat-Nasser and A. Shokooh. On finite plastic flows of compressible materials with internal friction. *International Journal of Solids and Structures*, 16:495–514, 1980.

M. Nicolas, P. Duru, and O. Pouliquen. Compaction of a granular material under cyclic shear. *European Physical Journal*, 3(4):309–314, December 2000.

E. R. Nowak, J. B. Knight, M. L. Povinelli, H. M. Jaeger, and S. R. Nagel. Reversibility and irreversibility in the packing of vibrated granular material. *Powder Technology*, 94(1):79–83, Novermber 1997.

B. J. Noye and R. J. Arnold. Accurate finite difference approximations for the neumann condition on a curved boundary. *Applied Mathematical Modelling*, 14 (1):2–13, 1990.

A. Nur and G. Mavko. Postseismic viscoelastic rebound. *Science*, 183:204–206, July 1974.

M. N. Ozisik. *Finite Difference Methods in Heat Transfer*. CRC Press. Inc., 1994.

M. S. Paterson and T. Wong. *Experimental Rock Deformation-The Brittle Field*. Springer, 2nd edition edition, 1977.

X. Le Pichon, C. Kreemer, and N. Chamot-Rooke. Asymmetry in elastic properties and the evolution of large continental strike-slip faults. *Journal of Geophysical Research*, 110, March 2005.

Y. Pinchova and J. Rubinstein. *An Introduction to Partial Differential Equations*. Cambridge University Press, 2005.

W. H. Prescott and A. Nur. The accommodation of relative motion at depth on the san andreas fault system in california. *Journal of Geophysical Research*, 86: 999–1004, 1981.

E. D. Reedy and T. R. Guess. Comparison of butt tensile strength data with interface corner stress intensity factor prediction. *International Journal of Solids and Structures*, 30(21):2929–2936, 1993.

H. F. Reid. *Report of the State Earthquake Investigation Commission in Two Volumes and Atlas*, volume II. The Carnegie Institution of Washington, 1910.

M. Renardy and R. C. Roberts. *An Introduction to Partial Differential Equations*. Springer, 2005.

J. R. Rice. Thermo-hydro-mechanics of shear rupture in fault zones, October 2007.

J. R. Rice and G. F. Rosengren. Plane strain deformation near a crack tip in a power-law hardening material. *Journal of the Mechanics and Physics of Solids*, 16(1):1–12, January 1968.

J. R. Rice and D. A. Simons. The stabilization of spreading shear faults by coupled deformation-diffusion effects in fluid-infiltrated porous materials. *Journal of Geophysical Research*, 81:5322–5334, October 1976.

J. R. Rice and S. T. Tse. Dynamic motion of a single degree of freedom system following a rate and state dependent friction law. *Journal of Geophysical Research*, 91:521–530, January 1986.

K. H. Roscoe. The influence of strains in soil mechanics. *Geotechnique*, 20:129–170, 1970.

K. H. Roscoe, R. H. Basset, and E. R. Cole. Principal axes observed during simple shear of a sand. *Proc. Geotech. Conf.*, 1:231–237, 1967.

B. Rowshandel and S. Nemat-Nasser. A mechanical model for deformation and earthquakes on strike-slip faults. *Pure and Applied Geophysics*, 124:531–565, 1986.

B. Rowshandel and S. Nemat-Nasser. Finite strain rock plasticity: stress triaxiality, pressure, and temperature effects. *Soil Dynamics and Earthquake Engineering*, 6(4):203–219, 1987.

F. Rummel, H. J. Alheid, and C. Frohn. Dilatancy and fracture induced velocity changes in rock and their relation to frictional sliding. *Pure and Applied Geophysics*, 116(4-5):743–764, 1978.

G. Ryskin and L. G. Leal. Numerical solution of free-boundary problems in fluid mechanics. part 1. the finite-difference technique. *Journal of Fluid Mechanics*, 148:1–17, November 1984.

J. C. Savage. Dislocation pile up as a repreentation of strain accumulation on a strike-slip fault. *Journal of Geophysical Research*, 111, 2006.

J. C. Savage and W. H. Prescott. Asthenosphere readjustment and the earthquake cycle. *Journal of Geophysical Research*, 83:3369–3376, July 1978.

C. H. Scholtz. *The Mechanics of Earthquakes and Faulting*. Cambridge University Press, 1990.

C. H. Scholtz. Earthquakes and friction laws. *Nature*, 391:37–42, January 1998.

J. M. Shi, M Breuer, and F. Durst. A combined analaytical-numerical method for treating corner singularities in viscous flow predictions. *International Journal for Numerical Methods in Fluids*, 45:659–688, 2004.

G. D. Smith. *Numerical Solution of Partial Differential Equations: Finite Difference Methods*. Clarendon Press, 1985.

A. J. M. Spencer. A theory of the kinematics of ideal soils under plane strain conditions. *Journal of the Mechanics and Physics of Solids*, 12:337–351, 1964.

A. J. M. Spencer. *Continuum Mechanics*. Longman, 1980.

A. J. M. Spencer and M. R. Kingston. Plane mechanics and kinematics of compressible ideal granular materials. *Rheol. Acta*, 12:194–199, 1973.

G. C. Spencer. *An Introduction to Plasticity*. Chapman and Hall Ltd, 1968.

W. Thatcher. Nonlinear strain buildup and the earthquake cycle on the san andreas fault. *Journal of Geophysical Research*, 88:5893–5902, July 1983.

J. F. Thompson, F. C. Thames, and C. W. Mastin. Automatic numerical generation of body-fitted curvilinear coordinate system for field containing any number of arbitrary two-dimensional bodies. *Journal of Computational Physics*, 15:299–319, 1974.

H. Tresca. Memoire sur l'ecoulement des corps solides soumis a de fortes pressions. *Comptes Rendus Acad. Sci. Paris*, 59:754, 1864.

D. L. Turcotte and D. A. Spence. An analysis of strain accumulation on a strike slip fault. *Journal of Geophysical Research*, 79:4407–4412, July 1974.

M. R. Visbal and D. V. Gaitonde. On the use of higher-order finite-difference schemes on curvilinear and deforming meshes. *Journal of Computational Physics*, 181:155–185, September 2002.

R. von Mises. Mechanik der festen korper im plastisch deformablen zustand. *Math. Phys. Klass*, 1:582–592, 1913.

R. Wang, F. L. Martin, and F. Roth. Computation of deformation induced by earthquakes in a multilayered elastic crust. *Computers and Geophysics*, 29:195–207, March 2003.